

THE UNIVERSITY OF CHICAGO

DISCOVERY OF VISUAL SEMANTICS BY UNSUPERVISED AND  
SELF-SUPERVISED REPRESENTATION LEARNING

A DISSERTATION SUBMITTED TO  
THE FACULTY OF THE DIVISION OF THE PHYSICAL SCIENCES  
IN CANDIDACY FOR THE DEGREE OF  
DOCTOR OF PHILOSOPHY

DEPARTMENT OF COMPUTER SCIENCE

BY  
GUSTAV MARTIN LARSSON

CHICAGO, ILLINOIS

AUGUST 2017

Copyright © 2022 by Gustav Martin Larsson  
All Rights Reserved

# TABLE OF CONTENTS

LIST OF FIGURES . . . . .	vi
LIST OF TABLES . . . . .	vii
ACKNOWLEDGMENTS . . . . .	viii
ABSTRACT . . . . .	ix
INTRODUCTION . . . . .	1
1 UNSUPERVISED REPRESENTATION LEARNING . . . . .	4
1.1 Introduction . . . . .	4
1.2 Stacked Mixture Models . . . . .	5
1.2.1 Related Work . . . . .	5
1.2.2 Parts Model . . . . .	8
1.2.3 Latent Transformation . . . . .	11
1.2.4 Permutation EM . . . . .	12
1.2.5 Implementing Transformation . . . . .	13
1.2.6 Classification . . . . .	15
1.2.7 Independence Assumption . . . . .	15
1.2.8 Layer Types . . . . .	16
1.2.9 Experiments . . . . .	17
1.3 Autoencoder . . . . .	20
1.3.1 Related Work . . . . .	21
1.3.2 Shortcut Autoencoder . . . . .	23
1.3.3 Baseline Results . . . . .	25
2 AUTOMATIC COLORIZATION . . . . .	27
2.1 Introduction . . . . .	27
2.2 Related work . . . . .	30
2.3 Method . . . . .	31
2.3.1 Color Spaces . . . . .	32
2.3.2 Loss . . . . .	33
2.3.3 Inference . . . . .	34
2.3.4 Ground-Truth Histogram Transfer . . . . .	36
2.3.5 Neural Network Architecture . . . . .	37
2.3.6 Network Re-Balancing . . . . .	38
2.3.7 Dense vs. Sparse Sampling . . . . .	39
2.4 Experiments . . . . .	41
2.5 Conclusion . . . . .	47

3	SELF-SUPERVISED REPRESENTATION LEARNING . . . . .	49
3.1	Introduction . . . . .	49
3.2	Related Work . . . . .	51
3.3	Method . . . . .	53
3.3.1	Colorization as the Target Task . . . . .	53
3.3.2	Colorization as a Proxy Task . . . . .	55
3.4	Results . . . . .	58
3.4.1	PASCAL . . . . .	58
3.5	Experiments . . . . .	59
3.5.1	Loss . . . . .	59
3.5.2	Network Architecture . . . . .	60
3.5.3	ImageNet Pretraining . . . . .	62
3.5.4	Training Time and Learning Rate . . . . .	63
3.5.5	Latent Representation . . . . .	64
3.5.6	Color . . . . .	66
3.6	Conclusion . . . . .	66
4	MULTI-PROXY REPRESENTATION LEARNING . . . . .	69
4.1	Introduction . . . . .	69
4.2	Related Work . . . . .	71
4.3	Model Distillation . . . . .	72
4.3.1	Task-Agnostic Distillation . . . . .	73
4.3.2	New Distillation Loss . . . . .	74
4.3.3	AB Divergence . . . . .	76
4.3.4	Feature Compatibility . . . . .	79
4.3.5	Data Augmentation, Dropout, and Warm Start . . . . .	80
4.4	Disjoint Weights Training . . . . .	81
4.4.1	Split-Activations . . . . .	81
4.4.2	Split-Weights . . . . .	82
4.5	Shared Weights Training . . . . .	82
4.5.1	Uneven Gradients Problem . . . . .	83
4.5.2	Separate Adaptive Optimizers . . . . .	84
4.5.3	Globally Normalized SGD (NormSGD) . . . . .	85
4.5.4	Round-Robin Scheduling . . . . .	88
4.6	Evaluation . . . . .	88
4.6.1	Distillation . . . . .	89
4.6.2	Multi-Task Representation Learning . . . . .	92
4.7	Multi-Proxy Self-Supervision . . . . .	97
4.7.1	Proxy Tasks . . . . .	97
4.7.2	Method . . . . .	99
4.7.3	Results . . . . .	99
4.8	Conclusion . . . . .	101
	CONCLUSION . . . . .	104



A	PERMUTATION EM . . . . .	105
A.1	Introduction . . . . .	105
A.1.1	Cyclic Groups . . . . .	105
A.1.2	Permutations . . . . .	105
A.1.3	Notation . . . . .	106
A.2	Model . . . . .	107
A.3	Expectation Maximization . . . . .	107
A.4	Coding Features . . . . .	109
	REFERENCES . . . . .	111

## LIST OF FIGURES

1.1	Variations of MNIST examples . . . . .	7
1.2	Rotatable parts on MNIST . . . . .	9
1.3	Feature transformation . . . . .	13
1.4	Class-level mixture model on MNIST . . . . .	20
1.5	Autoencoder schematics . . . . .	22
2.1	System overview . . . . .	28
2.2	Artifacts without chromatic fading . . . . .	35
2.3	Fully automatic colorization results on ImageNet/ctest10k . . . . .	38
2.4	Dense vs. sparse hypercolumns . . . . .	39
2.5	Additional colorization results . . . . .	42
2.6	Examples on SUN-6 . . . . .	43
2.7	Cumulative histogram of per-pixel error on SUN-6 . . . . .	45
2.8	Histogram of per-image PSNR on SUN-A . . . . .	45
2.9	Failure modes . . . . .	47
2.10	Sampling multiple colorizations . . . . .	47
3.1	Self-supervision overview . . . . .	50
3.2	Feature re-use/re-purpose . . . . .	53
3.3	Feature shift . . . . .	54
3.4	Learning rate . . . . .	64
3.5	Feature visualization . . . . .	68
4.1	AB divergence . . . . .	77
4.2	Shape of AB divergence . . . . .	78
4.3	Schematic of disjoint weights training . . . . .	81
4.4	Gradient norm . . . . .	86
4.5	AB divergence as a distillation loss . . . . .	93
4.6	First convolutional filters . . . . .	100
4.7	Inter-proxy training loss . . . . .	103
A.1	Latent permutations . . . . .	110

## LIST OF TABLES

1.1	Results on variations of MNIST . . . . .	17
1.2	Small sample size . . . . .	18
1.3	Autoencoders for pretraining . . . . .	25
2.1	Hypercolumn sparsity . . . . .	40
2.2	Validation on ImageNet/cval1k . . . . .	41
2.3	Ablation study of hypercolumn components . . . . .	41
2.4	Results on SUN-6 . . . . .	45
2.5	Results on SUN-6 (with ground truth histograms) . . . . .	45
3.1	Comparison on VOC of self-supervised pretraining methods . . . . .	57
3.2	Self-supervision loss . . . . .	59
3.3	Color vs. grayscale input . . . . .	59
3.4	Network architecture validation . . . . .	60
3.5	ImageNet pretraining variations . . . . .	61
3.6	End-to-end fine-tuning . . . . .	65
4.1	Test architectures . . . . .	89
4.2	Distillation problems . . . . .	90
4.3	Distillation loss . . . . .	91
4.4	Distillation methods . . . . .	92
4.5	Multi-task learning . . . . .	96
4.6	Round-robin task scheduling . . . . .	97
4.7	Multi-proxy self-supervision . . . . .	102

## ACKNOWLEDGMENTS

I want to start by thanking my primary advisor, Gregory Shakhnarovich. You have been a great mentor and teacher, attentive to both personal needs and professional development. Above all else, you gave me what I sought the most from an advisor: an environment where hard work is rewarded with success and fulfillment.

I also want to thank my co-advisor and advisor for my Master's degree, Yali Amit. You and I have spent countless of hours discussing research and machine learning, which has helped me gain invaluable experience, intuition, and perspective. In this dissertation, Yali was my primary advisor for the work in section 1.2.

I also owe a great deal to my close collaborator Michael Maire, who has been involved in almost every aspect of this dissertation and has in many ways been a deputy advisor to Greg. I appreciate everything that you have done for me.

Furthermore, I want to thank my entire committee, Gregory Shakhnarovich, Yali Amit, Michael Maire, and Risi Kondor. Anne Rogers, thank you for making the job of a teaching assistant fun and fulfilling. I also appreciate that I could always turn to you with problems, big and small. A final thanks to all the students, faculty, administrative and technical staff at both University of Chicago and TTI-Chicago.

Chenan, the support that you have given me is hard to put into words and more than I ever intended to put on your shoulders. You have accepted my problems as ours, and given me a strength that I do not have alone. When things get tough and I despair and retreat, you are reasoned, levelheaded, and get straight to finding a solution.

Ett stort tack till mina föräldrar Mats och Gunnel, syskon Loe och Erik, släkt och vänner hemma i Sverige. Loe, du och David var ett ovärderligt stöd i Chicago. Farfar, du var den förste som upptäckte och uppmuntrade mitt intresse för matematik. Tack.

# ABSTRACT

The success of deep learning in computer vision is rooted in the ability of deep networks to scale up model complexity as demanded by challenging visual tasks. As complexity is increased, so is the demand for large amounts of labeled data to train the model. This is associated with a costly human annotation effort. Modern vision networks often rely on a two-stage training process to satisfy this thirst for training data: the first stage, *pretraining*, is done on a general vision task where a large collection of annotated data is available. This primes the network with semantic knowledge that is general to a wide variety of vision tasks. The second stage, *fine-tuning*, continues the training of the network, this time for the target task where annotations are often scarce. The reliance on supervised pretraining anchors future progress to a constant human annotation effort, especially for new or ever-changing domains. To address this concern, with the long-term goal of leveraging the abundance of cheap unlabeled data, we explore methods of unsupervised pretraining. In particular, we propose to use self-supervised automatic image colorization.

We begin by evaluating two baselines for leveraging unlabeled data for representation learning. One is based on training a mixture model for each layer in a greedy manner. We show that this method excels on relatively simple tasks in the small sample regime. It can also be used to produce a well-organized feature space that is equivariant to cyclic transformations, such as rotation. Second, we consider autoencoders, which are trained end-to-end and thus avoid the main concerns of greedy training. However, its per-pixel loss is not a good analog to perceptual similarity and the representation suffers as a consequence. Both of these methods leave a wide gap between unsupervised and supervised pretraining.

As a precursor to our improvements in unsupervised representation learning, we develop a novel method for automatic colorization of grayscale images and focus initially on its use as a graphics application. We set a new state-of-the-art that handles a wide variety of scenes and contexts. Our method makes it possible to revitalize old black-and-white photography,

without requiring human effort or expertise. In order for the model to appropriately recolor a grayscale object, it must first be able to identify it. Since such high-level semantic knowledge benefits colorization, we found success employing the two-stage training process with supervised pretraining. This raises the question: If colorization and classification both benefit from the same visual semantics, can we reverse the relationship and use colorization to benefit classification?

Using colorization as a pretraining method does not require data annotations, since labeled training pairs are automatically constructed by separating intensity and color. The task is what is called *self-supervised*. Colorization joins a growing family of self-supervision methods as a front-runner with state-of-the-art results. We show that up to a certain sample size, labeled data can be entirely replaced by a large collection of unlabeled data. If these techniques continue to improve, they may one day supplant supervised pretraining altogether. We provide a significant step toward this goal.

As a future direction for self-supervision, we investigate if multiple proxy tasks can be combined to improve generalization in the representation. A wide range of combination methods is explored, both offline methods that fuse or distill already trained networks, or online methods that actively train multiple tasks together. On controlled experiments, we demonstrate significant gains using both offline and online methods. However, the benefits do not translate to self-supervision pretraining, leaving the question of multi-proxy self-supervision an open and interesting problem.

# INTRODUCTION

Supervised versus unsupervised learning is a central debate in machine learning. Supervision in computer vision typically refers to training images that are annotated with additional information, such as class label (*e.g.*, “dog”). To solve a prediction task, some annotated samples are required to define the task. *Representation learning* is the act of learning useful features from input samples and can be helpful prior to prediction training, especially if labeled samples are scarce. This *pretraining* procedure can be either supervised or unsupervised. The choice between the two is in our experience straightforward: Supervise *if* you have the means to supervise. That is, if you have data annotations, using them typically offers substantial improvements over using the data as raw unlabeled data. The “if” is important, since it may be costly or impractical. Having humans annotate a large set of data is error-prone, expensive, and could lead to over-specialization to the pretraining task. Constantly annotating new data for an autonomous robot, as the environment changes, can be impractical and limit its autonomy. The prospect of an unsupervised method that is able to leverage the abundance of raw sensory data would allow vision systems to seamlessly adapt to new situations and promote progress in new domains. We argue that this is a worthwhile pursuit. In this dissertation, we investigate options for unsupervised representation learning and present promising progress toward the goal of reducing the reliance on labeled data.

Taking a step back, two of the primary sub-areas of machine learning are supervised and unsupervised learning. The former, *supervised learning*, takes training data of inputs and outputs, with the goal of learning a model that can correctly predict outputs given inputs. The loss driving the learning is its ability to correctly predict outputs, or perform a closely related surrogate task. The latter, *unsupervised learning*, has a less clearly defined goal and can be used for several reasons. Given input samples, it may be used to find interesting structure in the data, to generate synthetic samples, or to learn a function that maps the data into a useful feature space that hopefully benefits downstream supervised learning. The

last goal can also be achieved through supervised learning itself, by training on a supervised task similar to the downstream task (*transfer learning*). The performance gap between unsupervised and supervised representation learning has in computer vision tilted in favor of supervised methods, and the gap has become increasingly wide as networks and sample sizes have grown.

However, a new family of methods, *self-supervision*, is reversing this trend of a widening gap by greatly improving representation learning on unlabeled data. The technique involves manufacturing a supervised prediction task on raw data, similar to playing a game with yourself. For instance, an agent (*e.g.*, child) picks up a ball and places it on a slanted surface, guessing its rolling trajectory. The correct outcome is subsequently observed and if the prediction was wrong the agent can learn from its mistake.

Chapter 1 discusses two distinct methods of traditional unsupervised learning. Both methods build multi-layer feed-forward convolutional networks, which has become standard practice in computer vision. The main difference between the two methods lies in the way they are trained: one layer at a time (greedy) or all layers together (end-to-end). The former method, which is the primary contribution of the chapter, works well on small-scale problems and can cleverly deal with latent transformations, such as rotations. However, neither of the two methods succeed in providing significant benefits in the increasingly complex challenges in computer vision.

In chapter 2, we take a break from representation learning and focus on automatic colorization: a technique to bring color to old black-and-white photographs. With the assumption that colorization requires semantic knowledge, we build a new algorithm inspired by work in semantic segmentation. We accommodate the multimodal nature of color by predicting distributions over a color space. This rich prediction representation captures the notion that a grayscale image can be associated with several plausible colorizations and can be used in post-processing. We also present a novel memory-efficient training method using



sparsely sampled color targets, with applications beyond colorization to any image-to-image prediction task. Finally, we establish new quantitative colorization benchmarks to promote further progress.

The broader implications of automatic colorization become clear in chapter 3, where we show it to be a strong self-supervised proxy task for representation learning. The difficulty and importance of high-level semantics in colorization drives a general-purpose representation that can be used for other visual tasks, such as classification and semantic segmentation. We demonstrate state-of-the-art results on both when supervised pretraining is forgone. A series of stress tests on supervised pretraining (smaller sample size, reduced label space, label noise, etc.) sheds further light on the similarities between supervised and self-supervised learning.

In chapter 4, we explore the possibility of using multiple proxy tasks as a future direction. We evaluate both *offline* and *online* methods. Offline is what we call methods that combine already trained networks without being aware of how the networks were originally trained. We evaluate network concatenation and a novel method of task-agnostic model distillation. Online is a method that actively trains multiple proxy tasks jointly. We identify key issues that may occur during joint training, such as unbalanced gradients, and propose effective solutions. Through a variety of controlled experiments based on supervised pretraining, we show success for both offline and online methods. Despite promising results, our techniques interestingly do not move the needle in the context of self-supervision. However, we hope that our investigation lays the groundwork for future work in making self-supervision compete with supervised pretraining.

# CHAPTER 1

## UNSUPERVISED REPRESENTATION LEARNING

We evaluate two traditional methods for unsupervised representation learning, establishing baselines for future chapters and showing how difficult it is to leverage unlabeled data.

### 1.1 Introduction

The main contribution of this chapter is a greedy method of training a multi-layer network presented in section 1.2. The method is based on representing the data distribution of image patches or intermediate feature patches as mixture models. Training is driven by trying to maximize the likelihood of unlabeled training data under this model. Once a network has been trained, a modest amount of labeled data can be used at the top layer to solve visual tasks. We show competitive results on simple tasks, such as variations on MNIST. The feature space can also be organized to be equivariant to cyclic transformations, which we demonstrate by successfully training a model on MNIST with random rotations. However, due to its greedy training, it fails to scale up to the size required by modern computer vision architectures.

To address the concerns of greedy training, we evaluate in section 1.3 autoencoders, an unsupervised model trained end-to-end. This allows top layers to signal corrections they would like to see in lower layers, using back-propagation of errors. The model is phrased as a compression problem with an encoder and a decoder, where the encoder can subsequently be used as a feature extractor. A good representation intended to solve high-level tasks should be invariant to low-level semantics and help organize high-level semantics into features. The reconstruction loss, operating on a per-pixel level, encourages the opposite by putting a large price on perceptually insignificant differences.

The purpose of this chapter is primarily to establish a baseline and give context to

self-supervised learning by describing two predecessors. Additionally, we offer the following contributions:

- A method to build multi-layer feature extractors using mixture models. It is trained greedily and can be made equivariant to cyclic transformations. It works particularly well in the small-sample regime.
- Shortcut Autoencoder, a novel technique for efficient training of deep autoencoders.

## 1.2 Stacked Mixture Models

We present a framework for building multi-layer networks, with the option of an organized feature space equivariant to rotation or other cyclic transformations. The work is an extension of the parts-based model developed by Bernstein & Amit [9]. On the surface, it resembles a convolutional neural network (CNN), with several layers and weight sharing across spatial translations. However, training is layer-wise and unsupervised. This means, it uses no back-propagation and class-annotated data is only needed at the final classification layer. Each layer is based on a mixture model trained on unlabeled data. We demonstrate that this model works well on simple tasks, such as variations on MNIST, and is particularly competitive when annotated data is scarce.

### 1.2.1 Related Work

Our starting point is the *parts model* by Bernstein & Amit [9], using mixture models to learn unsupervised visual representations. Coates *et al.* [21] similarly use  $k$ -means clustering to learn dictionaries of parts. At test time, both of these models are analogous to the convolutional filters in a CNN. However, training is both greedy and unsupervised, making it fast and cheap to estimate parameters. In this section, we outline similar unsupervised

representation learning methods, with a particular focus on its contemporary methods from 2014, when our work was developed.

The Restricted Boltzmann Machine (RBM) [107] is an undirected graphical model forming a bipartite graph between visible and hidden binary units. The bipartite structure, which makes it a *restricted* version of a Boltzmann machine [47], ensures that visible units are conditionally independent of hidden units and can be sampled directly; the same is true reversing the roles of hidden and visible units. Inference of the joint probability between hidden and visible units is slightly harder, but can be done using repeated Gibbs sampling. The process involves alternating between sampling visible units conditioned on hidden, and hidden units conditioned on visible, until convergence. The models are trained using gradient methods on the log-likelihood. To do this properly, for each iteration of parameter updates, an inner loop of Gibbs sampling is required. However, it has been shown that training can be successfully performed even when the Gibbs sampling has not converged. This technique is called Contrastive Divergence [44].

There are two primary multi-layer extensions of the RBM. The first one is called Deep Belief Networks (DBN) [46]. After training an initial RBM, a second one is trained with the hidden layers of the first one now as visible units of the next. This creates a series of RBMs trained sequentially in a greedy fashion. The only layers in the finished model that form an RBM are the two top layers, since after those two layers units are sampled conditioned on the hidden units using directed graphical models. The finished model can be fine-tuned end-to-end, by effectively turning it into an autoencoder with tied weights [46]. The DBN can also be made into a convolutional DBN [70]. The second multi-layer extension is the Deep Boltzmann Machine (DBM) [102], which preserves the undirectedness in each layer, making inference more complicated and computationally more intensive. This is often alleviated by using similar methods of training a DBN as initial pretraining, followed by sampling strategies.

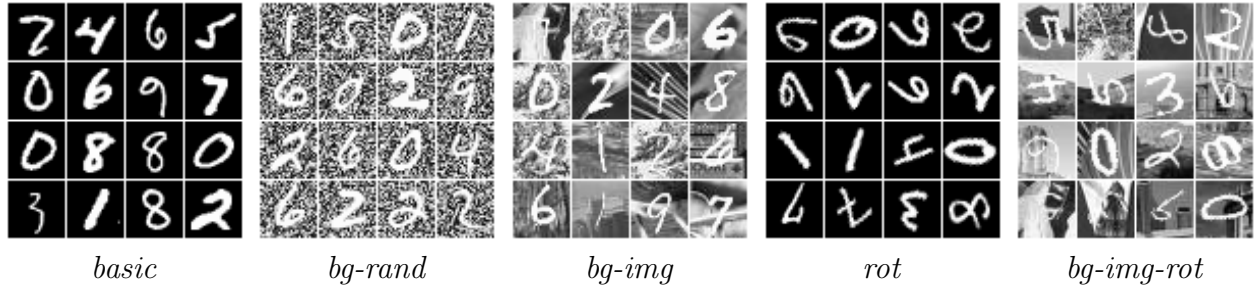


Figure 1.1: **Variations of MNIST examples.** The variations include added background images or noise and random rotations. All variants are divided into 10,000 training, 2,000 validation, and 60,000 testing samples.

The standard way of using an RBM (or DBN/DBM) for classification is to use the top-layer’s hidden units as features fed to a linear classifier. There are also ways to make the discriminative training part of the RBM training [65]. Fine-tuning discriminatively is also an option, effectively turning the RBM into a feed-forward network. The point of the RBM training is in such case to pretrain the network.

There are many more flavors of RBMs. We discuss briefly a few that relate specifically to our test benchmarks. Nair & Hinton proposed something reminiscent of mixture models for RBMs [85], with separate sets of parameters for each mixture component. This work was extended by Sohn *et al.* [110] in Point-wise Gated Boltzmann Machines (PGBM), by allowing the mixture components to be specified per pixel. This is realized by having a binary gate for each pixel that determines which component is active. This framework can be used to learn task-relevant and task-irrelevant features, which is particularly suited for MNIST with cluttered background (see fig. 1.1). The task-irrelevant features can subsequently be discarded by only feeding the task-relevant activations into a classifier, making the model more robust to noise.

The Transformation-Invariant RBM (TIRBM) [109] can learn invariance to transformations such as rotation, scale, and translation. It does this by introducing a vector of hidden units indicating transformation and regularized to be one-hot. Each element is associated

with a pre-defined linear transformation matrix that operates on the input samples before fed into the regular RBM weights. The model is a single-layer RBM with no generalization to multiple layers.

We also compare results to the Stacked Denoising Autoencoder (SDAE) [123]. It is also a greedy and unsupervised model, that for each layer trains a single-layer autoencoder. It fixes the encoder as the first layer and continues to train on the subsequent layer. It injects noise into the input, while keeping the clean sample as the reconstruction target. Today, it would be more common to train the autoencoder end-to-end and use dropout [111] as a regularizing noise injection. We evaluate this approach in section 1.3.

Since our work in 2014, there have been several attempts at building features equivariant to rotations using CNNs trained end-to-end [17, 22, 24, 126, 140]. Although not presented in our tables, this has further improved state-of-the-art on benchmarks with randomly rotated samples. However, these methods are fully supervised and are not relevant to unsupervised representation learning, unlike the RBM-based methods.

### 1.2.2 *Parts Model*

We begin by reviewing the *parts model* by Bernstein & Amit [9], presenting it in slightly more general terms. The final model is a feed-forward network composed of several layers:

$$f = f_L \circ \cdots \circ f_1$$

The model is trained in a greedy manner, which means  $f_1$  is trained first without regard for any other layer, then  $f_2$  without changing  $f_1$ , and so forth. To formulate  $f_l$ , we associate each layer with a stationary (translation-invariant) distribution over a small spatial window. If, for instance,  $\text{dom}(f_l) \subset \mathbb{R}^{H \times W \times F}$  (height, width, feature channels), then the distribution describes how to draw samples from  $\mathbb{R}^{S \times S \times F}$  representing any spatial region of the incoming

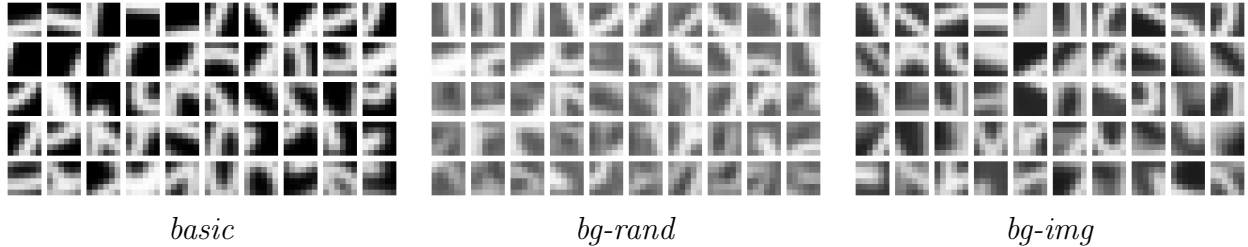


Figure 1.2: **Rotatable parts on MNIST.** Examples of 6-by-6 convolutional parts learned using a mixture models with latent rotation on variations of MNIST (see fig. 1.1). Only the canonical rotation (that happens to have the leading index) is displayed for each part.

representation. We model the distribution over each patch as a mixture model. The latent mixture component can be thought of as defining what type the patch represents from a dictionary of parts. At low levels, a part can represent a specific type of edge (see fig. 1.2) and at higher levels it could be part of a semantic object. This is different from the distributed representation of an RBM, where each hidden unit represents only one of several active aspects of the visible units. Each mixture component can be modeled with a variety of distributions. Although the framework is general, we focus primarily on products of Bernoulli distributions.

The distribution allows us to sample patches of intermediate representations. However, our model is only generative in this local sense, since we do not describe how to sample an entire image with overlapping patches (unlike for instance the POP model [2]). Luckily, sampling is not our primary interest and instead we focus on the representation that we can learn through this process. The goal of the layer is to transform the incoming signal in a way that will eventually benefit discriminative tasks. This typically means summarizing the co-occurrence patterns of low-level features into a single high-level feature (*e.g.*, this group of pixels describes a line). The hope is that the estimated distribution has captured this underlying structure in a succinct and meaningful representation. Hinton describes this method of representation learning as “procrastination” [45], since a supervised task is not involved until the very last layer and there is an element of hope that it will eventually be

useful.

The statistical model so far given input gives back a likelihood, not a set of features. We need an activation function,  $g$ , that takes the likelihood  $p_i = p(X \mid Z = i)$  for each component  $i$  and converts it to a feature ready to be passed to the next layer. To discuss concrete suggestions for  $g$ , we must be specific about the type of distribution.

**Bernoulli.** Our main focus is when the distribution is a product of Bernoulli distributions

$$p(X \mid Z = z) = \prod_d p(x_d; \theta_{z,d}) = \prod_d \theta_{z,d}^{x_d} (1 - \theta_{z,d})^{(1-x_d)}, \quad (1.1)$$

where  $d$  indexes spatial and feature dimensions together. The activation function then forms a one-hot vector of the maximum likelihood component:

$$[g(p)]_i = \begin{cases} 1 & \text{if } p_i = \max_j p_j \\ 0 & \text{otherwise} \end{cases} \quad (1.2)$$

This creates a sparse binary feature representation. In order to make it more robust to local spatial translations, we spread the 1's to nearby locations using morphological dilation.

**Gaussian.** It can also be based on Gaussian mixture models (GMM), with a range of options for parameterization of the covariance matrix. Coates *et al.* [21] lend inspiration for  $g$ , who similarly built an unsupervised feature extractor using  $k$ -means clustering. The activation function they call *hard* is the same as (1.2), with  $p_i$  defined as the negative distances to centroid  $i$ . A second one is called *triangle*, which assigns soft scores to each component and then passes it through a rectifier. The soft score is designed so that roughly half of the features are rectified. An analogous activation for GMM would be:

$$[g(x)]_i = \max\{0, \log p_i - \frac{1}{F} \sum_j \log p_j\} \quad (1.3)$$



### 1.2.3 Latent Transformation

The mixture model's latent space can be extended to be a product of latent component *and* latent transformation. The latent space thus holds information not just about which part from a dictionary, but also which instantiation of the part (*e.g.*, orientation, polarity, etc.). We focus on transformations that can be expressed as products of cyclic groups. For instance, we could have a group with  $R$  rotations around the part's center. Let  $\Phi : \mathcal{X} \mapsto \mathcal{X}$  be a  $\frac{360}{R}$ -degree rotation around the center. The transformation  $\Phi$  then generates the cyclic rotational group. If  $x \in \mathcal{X}$  denotes a single sample, let  $\mathbf{x} \in \mathcal{X}^R$  denote a *complete* sample that contains the complete group's transformations of  $x$ :

$$\mathbf{x} = [x, \Phi x, \Phi^2 x, \dots, \Phi^{R-1} x] \quad (1.4)$$

We associate  $\mathbf{x}$  with a permutation,  $\sigma = (0 \ 1 \ \dots \ R-1)$ . For a direct product of two cyclic groups, the permutation  $\sigma$  will be the product of the two permutations. Let  $A$  denote the permutation matrix corresponding to  $\sigma$  and let  $A(i, j)$  denote indexing the matrix.

We refer to the latent joint variable as  $(Z, W)$ , where  $Z$  represents component and  $W$  permutation. The model for a Bernoulli mixture model with latent transformation becomes

$$(Z, W) \sim \text{Cat}(\pi), \quad (1.5)$$

$$X_{w',d} \mid Z = z, W = w \sim \text{Bern}(\mu_{z,A(w,w'),d}), \quad \forall w', d \quad (1.6)$$

where  $w'$  indexes which transformation of the complete sample and  $d$  the sample feature (over channels and both spatial dimensions). Note that the random variable  $X$  models the complete sample. We now see the purpose of  $A$ : permuting the parameter space of the complete sample depending on the latent transformation. Next, we describe how to estimate the parameters  $\pi$  and  $\mu$ .

### 1.2.4 Permutation EM

Expectation Maximization (EM) is used to train the original parts model. The latent permutation mixture model can be trained with an adaptation that we call Permutation EM. We describe how this is done specifically for the Bernoulli mixture model, although a Gaussian mixture model is closely analogous. We present the modifications briefly and assume that the reader is familiar with EM. For more details and derivations, see appendix A.

**E-Step.** The responsibilities  $\gamma^{(n)}$  for sample  $n$ , are computed over the joint latent variable  $(Z, W)$  as

$$\gamma_{z,w}^{(n)} = \frac{\tilde{\gamma}_{z,w}^{(n)}}{\sum_{z',w'} \tilde{\gamma}_{z',w'}^{(n)}}, \quad \tilde{\gamma}_{z,w}^{(n)} = \pi_{z,w} \prod_{w',d} p(x_{A(w,w'),d}^{(n)}; \mu_{z,w',d}), \quad (1.7)$$

where,  $p$  is defined in (1.1). To avoid numerical underflow, it is better to compute and store logarithms of the unnormalized responsibilities  $\tilde{\gamma}$  and use the log-sum-exp trick.

**M-Step.** The parameters are updated as follows:

$$\pi_{z,w} \leftarrow \frac{1}{N} \sum_n \gamma_{z,w}^{(n)} \quad \mu_{z,w,d} \leftarrow \frac{\sum_{n,w'} \gamma_{z,w'}^{(n)} x_{A(w,w'),d}}{\sum_{n,w'} \gamma_{z,w'}^{(n)}} \quad (1.8)$$

In words, the E-step computes responsibilities over best matched component *and* transformation. The complete sample is permuted according to a latent transformation, which synchronizes the samples of various shape *and* pose into sharp models in the M-step. In the case of latent rotation, the responsibilities learn the rotation of each sample relative to an arbitrary canonical rotation.

Since the latent model is a distribution over *complete* samples, extracting features strictly requires building the complete sample and evaluating the likelihood of each component and

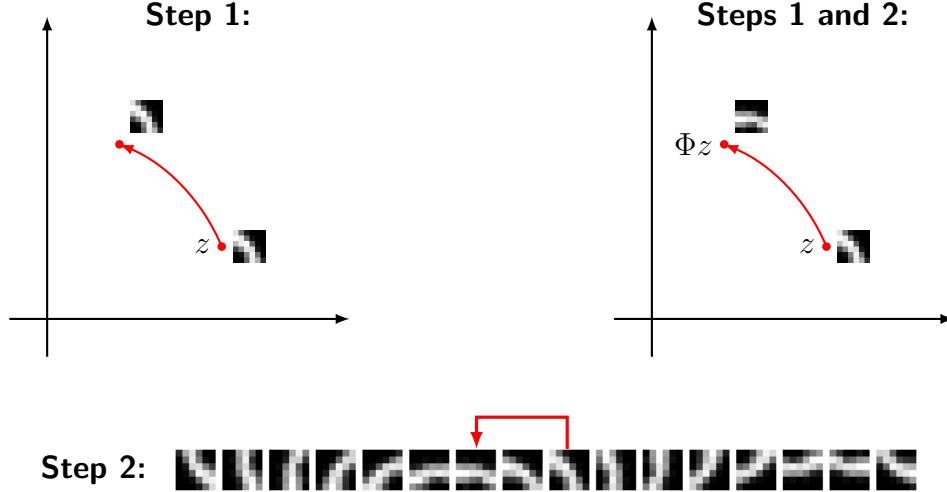


Figure 1.3: **Feature transformation.** Transformation ( $\Phi$ ) of a feature space is a two-step process: (1) spatial transformation, and (2) permutation of the feature space. The figure depicts a 45-degree counter-clockwise rotation around the origin of a feature space with latent rotation ( $R = 16$ ).

permutation. However, this is costly and tedious as a feature extractor. Instead, we ignore that we trained the parts using complete samples, and instead consider each part and transformation as a separate feature. We then use (1.2) as we normally would to code features. The feature space can of course still be interpreted with an association between parts and its transformed siblings.

### 1.2.5 Implementing Transformation

A few notes on how to implement the transformation  $\Phi$ , specifically for latent rotation. At the first layer,  $\Phi$  simply becomes an image rotation operation on the patches (transformation and resampling, typically with bilinear interpolation). However, if the patch is used in an intermediate layer and each feature represents an oriented structure, this is not enough to correctly transform the feature space. We present two options.

First, the transformation is performed as a two-step process: transforming and permuting. The first step is to transform the spatial dimensions, using the same technique as in the first

layer. The difference is that instead of 1 or 3 color channels, we now typically have a lot more feature channels. However, more profoundly, unlike color pixels, the features represent local structure beyond their center pixel. This structure is typically not rotation invariant, so if we rotate a feature 45 degrees, we also need to rotate what the feature represents by 45 degrees. To make this correction we permute the feature space, assuming that the incoming feature space is equivariant to rotation. These two steps are illustrated in fig. 1.3.

An alternative to this method is to rotate the original input and separately pass them through all previous layers. This has the advantage that we do not need to do further transforming or permuting. We can even use this layer on top of features that are not organized to be equivariant to rotation. The model will discover on its own how to rotate features to correspond best to the transformed inputs. This method is convenient even if the incoming feature space can be rotated. For instance, in the first layer we may use edges with 8 orientations, while in the second layer we may use parts with 32 orientations. We could write the correct permutation to synchronize the 8 and 32 orientations. However, the analytically transformed feature space may not perfectly correspond to transformation in the input space, due to the lower fidelity of 8 orientations. It is possible to choose different methods for different layers. If two subsequent layers have the same number of latent orientations, then the analytical approach becomes appropriate and efficient. Regardless of the method used during training, the finished feature space can always be analytically transformed.

A final note on resampling. When we rotate a point around the patch center, it may not end up exactly on the feature grid. We need to resample after transformation, which can be done with techniques like nearest neighbor or bilinear interpolation. However, even simpler, if your extraction layer is followed by a pooling layer you can simply check if the new point is within the pooling region (equivalent to nearest neighbor in the post-pooling feature space). We use this technique at layers that use pooling and nearest neighbor at layers that do not use pooling.

### 1.2.6 Classification

So far, we have only discussed unsupervised representation learning. Classification is done by training a global (patch covering the entire input) mixture model for each class  $y$  separately, storing the parameters in  $\theta_y$ . The same unlabeled training procedure is performed as before, except each model is trained only on samples from a specific class. With  $C$  separately trained top layers, a final class prediction is done exactly like feature extraction, where the maximum likelihood part is identified:

$$\hat{y} = \arg \max_y \log p(X | Y = y; \theta_y) \quad (1.9)$$

One of the benefits of this model is that new classes can be added without having to re-train existing classes. Each separately trained model for each class can itself be a mixture model of several components. In our main experiments, we use  $M = 1$ . This does not require EM and parameters are estimated by simple averaging. Even with such simple supervised training step, we do well thanks to the unsupervised representation from the previous layers.

### 1.2.7 Independence Assumption

The beauty of the mixture model is that the assumption of conditional independence does not imply the assumption of independence. This allows more complex dependence structure, while still being cheap to train and evaluate. However, having said that, the conditional independence assumption will still be violated by natural image data. There is always strong correlation between proximal features, even conditioned on the component. There may also be to a lesser extent long-range correlation in certain situations.<sup>1</sup> The reason for the independence assumption is that it makes training and inference straightforward.

One of the main concerns of breaking this assumption is that likelihood estimates will

---

1. In MNIST, where digits are centered, if the top of a 1 is located in the top-right corner, chances are it is a tilted 1 and the bottom will be located in the bottom-left corner. This creates a long-range correlation.

be wrong. This is true and likelihoods will in fact be grossly under-estimated. However, what we are interested in is only if the likelihoods compare well between components, as required by (1.9). It turns out that the under-estimations is fairly even across classes, or results would suffer. If a situation appears where class likelihoods are not balanced, it may help to standardize the log-likelihoods with statistics estimated from your training data.

With latent transformation, the violation becomes even clearer. The model assumes according to (1.5) that two transformations are conditionally independent given the joint latent variable. The likelihood of each individual segment of the complete sample will be nearly perfectly correlated with all the other transformations. This will under-estimate the likelihoods further, although again without disruption to our end goal.

### 1.2.8 *Layer Types*

Before describing the models that we evaluate, we outline the layers that we use as building blocks:

**Edges** Parameterless oriented binary edges defined in [9]. The output contains 8 features (cardinal and diagonal directions) per color channel based on intensity differences. Since a Bernoulli mixture layer requires binary input, this provides a bridge between the real-valued input and the rest of the binary network.

**Mixture** Bernoulli mixture model layer. At the final task layer, the patch size is set to be equal to the input size, making it effectively non-convolutional. Otherwise, the patch size is 6-by-6. The value  $M$  (mixture components) is left as an option. When used as an intermediate layer, we reduce spatial resolution by pooling features in 4-by-4 disjoint regions using element-wise OR (max) operations.

**RotMix** Bernoulli mixture model with latent orientation. Analogous to *Mixture*, with built-in pooling and the same patch size. Can also be used as a final task layer.

Model	<i>basic</i>	<i>bg-rand</i>	<i>bg-img</i>	<i>rot</i>	<i>bg-img-rot</i>
RBM [109]	-	-	-	15.6	54.0
RBM [110]	-	11.4	15.4	-	49.9
DBM-3 [66]	$3.1 \pm 0.2$	$6.7 \pm 0.2$	$16.3 \pm 0.3$	$10.3 \pm 0.3$	$47.4 \pm 0.4$
SDAE-3 [123]	$2.6 \pm 0.1$	$8.5 \pm 0.2$	$16.7 \pm 0.3$	$8.8 \pm 0.3$	$43.8 \pm 0.4$
SDAE-3 (Linear SVM) [123]	$2.6 \pm 0.1$	$11.3 \pm 0.3$	$14.6 \pm 0.3$	$10.0 \pm 0.3$	$42.1 \pm 0.4$
SDAE-3 (Kernel SVM) [123]	$2.6 \pm 0.1$	$10.2 \pm 0.3$	$14.1 \pm 0.3$	$8.6 \pm 0.3$	$39.1 \pm 0.4$
PGBM [110]	-	7.3	13.3	-	45.5
Supervised PGBM [110]	-	6.9	12.9	-	44.7
PGBM + DN-1 [110]	-	6.1	12.3	-	36.8
TIRBM [109]	-	-	-	<b>4.2</b>	35.5
Plain	$1.9 \pm 0.0$	$7.9 \pm 0.0$	$10.0 \pm 0.1$	$11.8 \pm 0.1$	$36.2 \pm 0.1$
Plain-SVM	<b><math>1.3 \pm 0.0</math></b>	<b><math>6.0 \pm 0.1</math></b>	<b><math>8.0 \pm 0.1</math></b>	$9.1 \pm 0.0$	$33.4 \pm 0.2$
Oriented	-	-	-	$5.5 \pm 0.1$	<b><math>25.0 \pm 0.8</math></b>

Table 1.1: **Variations of MNIST.** (Error rate, %) Evaluation on variations of MNIST (see fig. 1.1). 10,000 samples are used for training and 60,000 for testing. As a result, the first column *basic* should not be compared with regular MNIST results that train on 60,000 and test on 10,000. Our models in the bottom three rows are described in section 1.2.9.

Options include  $R$  (rotations) and  $M$  (mixture components). The number of parts at test time is  $R \cdot M$ .

**SVM** Multi-class linear SVM. This is evaluated as a discriminative alternative to log-likelihood comparisons.

### 1.2.9 Experiments

We consider three models, each with three layers:

**Plain** 1. Edges, 2. Mixture ( $S = 6, M = 1280$ ), 3. Mixture ( $M = 1$ )

**Plain-SVM** 1. Edges, 2. Mixture ( $S = 6, M = 1280$ ), 3. SVM

**Oriented** 1. Edges, 2. RotMix ( $S = 6, M = 40, R = 32$ ), 3. RotMix ( $M = 1, R = 16$ )

Model		<i>basic</i>	<i>bg-rand</i>	<i>bg-img</i>	<i>rot</i>	<i>bg-img-rot</i>
1000 samples/class (full)						
CNN		<b>1.8</b> $\pm$ 0.1	<b>4.3</b> $\pm$ 0.2	<b>8.0</b> $\pm$ 0.4	10.4 $\pm$ 0.3	31.9 $\pm$ 0.1
CNN (+rot. aug.)		-	-	-	<b>4.0</b> $\pm$ 0.1	<b>19.2</b> $\pm$ 0.3
Our model		1.9 $\pm$ 0.0	7.9 $\pm$ 0.0	10.0 $\pm$ 0.1	5.5 $\pm$ 0.1	25.0 $\pm$ 0.8
100 samples/class						
Semi-sup. PGBM [110]	✓	-	12.0 $\pm$ 0.8	20.3 $\pm$ 0.2	-	59.2 $\pm$ 0.7
CDBN [70]	✓	<sup>†</sup> <b>2.6</b> $\pm$ 0.1	-	-	-	-
CNN		4.7 $\pm$ 0.1	<b>10.2</b> $\pm$ 0.3	17.1 $\pm$ 0.4	25.0 $\pm$ 0.4	53.0 $\pm$ 0.9
CNN (+rot. aug.)		-	-	-	11.5 $\pm$ 0.2	<b>31.3</b> $\pm$ 0.8
Our model	✓	<b>2.6</b> $\pm$ 0.1	<b>10.2</b> $\pm$ 0.1	<b>14.7</b> $\pm$ 0.4	<b>7.8</b> $\pm$ 0.8	35.3 $\pm$ 2.1
10 samples/class						
CNN		15.6 $\pm$ 0.4	24.4 $\pm$ 0.9	34.2 $\pm$ 2.8	58.9 $\pm$ 0.7	75.5 $\pm$ 0.4
CNN (+rot. aug.)		-	-	-	26.2 $\pm$ 0.4	54.7 $\pm$ 1.0
Our model	✓	<b>8.8</b> $\pm$ 0.7	<b>21.1</b> $\pm$ 1.1	<b>29.7</b> $\pm$ 1.6	<b>16.4</b> $\pm$ 0.9	<b>48.4</b> $\pm$ 2.4
Check mark (✓) means all 10,000 training samples are used as additional unlabeled data						

Table 1.2: **Small sample size.** (Error rate, %) The sample size is varied from full (1,000 samples/class) to 10 samples/class. However, in the non-full cases, our models are allowed to observe the rest of the 10,000 samples as unlabeled data. This can be leveraged using pretraining (*e.g.*, our model) or semi-supervision (*e.g.*, PGBM [110]). Our model refers to *Plain* (see section 1.2.9) for the three columns on the left with no rotation and *Oriented* for the two columns on the right with rotation. The baseline CNN models do not use additional unlabeled samples. Since our rotational model is designed to work well for randomly rotated classes, we also augment the CNN training data with random rotations (“+rot. aug.”). The CNN is designed to be as similar as possible to our model. The biggest differences are in training and that our model has binary and not floating point activations. Our model performs well in all settings and particularly well when labeled sample size is small. (<sup>†</sup>evaluated on the original MNIST with 10,000 samples and not *basic* on 60,000 samples)



The models are evaluated on variations on MNIST [66], a set of derivatives that introduce various forms of background clutter and/or random rotations. It designates 10,000 samples for training, 2,000 for validation, and 60,000 for testing. This differs from the original MNIST, which has 60,000 samples for training and 10,000 for testing. Examples can be seen in fig. 1.1.

Results and comparisons to contemporary work are summarized in table 1.1. *Plain* provides strong results across all benchmarks. Switching the last layer to a discriminatively trained linear SVM consistently improves results. However, remember that this is less flexible in terms of adding new classes and does not work well for randomly rotated samples.

By using mixtures with latent orientation (*Oriented*), the results on MNIST with random rotations can be improved even further. TIRBM, which is the only other model that explicitly deals with random rotations, does slightly better for rotated MNIST with clean backgrounds. However, in the case of cluttered background images, we offer a 10-point improvement over their results. Our strong results on background clutter are also shown by beating all versions of PGBM, which has per-pixel gates specifically designed to deal with noise and clutter. It is worth noting however that RBMs typically do not use convolutional weight sharing, which puts them at a disadvantage. The Convolutional DBN (CDBN) performs on par with our results as seen in table 1.2. However, our model offers more straightforward training and inference.

We also compare against a 3-layer CNN, designed to be closely analogous to our network in table 1.2. We see that it performs better than our mixture model classifiers, but fairly close to our SVM-based results in table 1.1. If we reduce sample size from 1,000 per class to 100 and 10 per class, our model becomes increasingly competitive and outperforms the CNN. In order to give the CNN a more fair comparison on rotated MNIST, we also try augmenting data using random rotations. This greatly improves CNN results and it excels with enough samples. However, in the small-sample regime at only 10 samples per class, we

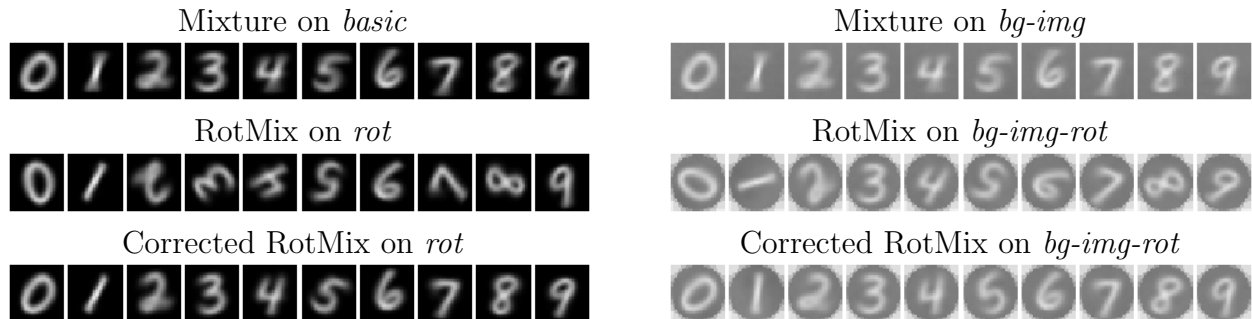


Figure 1.4: **Class-level mixture model on MNIST.** Top row is a Mixture layer (see section 1.2.8) with a single component trained on correctly rotated samples. The middle row is a RotMix layer with a single component and 16 latent rotations trained on randomly rotated data. The bottom row is the same as the middle row, except 5 correctly rotated samples have been used to designate the canonical rotation.

still do better.

Examples of trained parts (layer 2) can be seen in fig. 1.2 and trained classes (layer 3) can be seen in fig. 1.4. We note that a task-level mixture with latent orientations is able to train even cleaner versions of the digits on rotated samples than a plain mixture is on regular samples. This is because the *RotMix* layers can account for natural rotational variation, such as the tilt of the digit 1 (see fig. 1.4). Source code for all experiments is publicly available.<sup>2</sup>

### 1.3 Autoencoder

We have seen that stacked mixture models can be effective on simple benchmarks, such as variations on MNIST. However, the network contains only two parameterized layers and is difficult to grow deeper due to the greedy training. We shift our attention to another unsupervised model that can be trained end-to-end and thus allows deeper models to be trained to convergence.

The autoencoder is a feed-forward network with an encoder ( $f$ ) and a decoder ( $g$ ). The encoder can for instance be inspired by a regular convolutional feed-forward network used

---

2. <https://github.com/gustavla/parts-net>

for a visual classification task. The value returned by the encoder is then fed through a decoder to produce a reconstruction  $\hat{x} = g(f(x))$ . This is trained end-to-end using gradient descent on a per-pixel reconstruction loss:

$$\ell(x) = \|x - \hat{x}\|^2 \tag{1.10}$$

The autoencoder should contain an information bottleneck (most obviously controlled by the size of the encoded vector) or the task becomes trivial. The network must economize and learn how to represent high-level input with as few bits as possible. In the ideal case, the encoding represents local coordinates on a low-dimensional manifold that perfectly captures the data distribution. This does not happen and the main problem stems from the reconstruction loss, which operates on a per-pixel level with no regard to high-level semantics. Two samples that are perceptually similar to humans may have a large  $L_2$  difference. This uncompromising nature of the squared  $L_2$  loss forces the encoding to devote much informational real estate to low-level information.

The primary purpose of this section is to evaluate autoencoders for pretraining, in order to establish a baseline for subsequent chapters. Their poor ability to capture high-level semantics results in modest improvements over using no pretraining at all. In order to improve training of our baseline, we propose the Shortcut Autoencoder that converges well and improves pretraining results.

### 1.3.1 *Related Work*

Using autoencoders to facilitate the training of neural networks has been around since 1987 [5]. 20 years later, a similar idea in a more familiar form was developed by Bengio *et al.* [7]: Greedy layer-wise training of a DBN by fitting shallow autoencoders (single-layer encoder, single-layer decoder). The idea was inspired by Hinton & Salakhutdinov [46], who

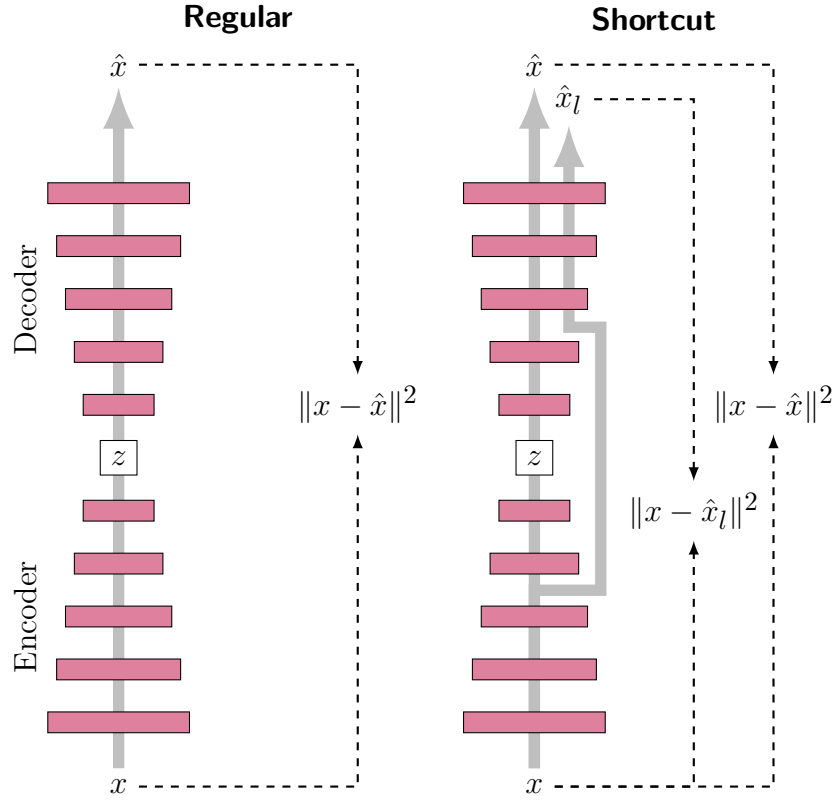


Figure 1.5: **Autoencoder schematics.** Schematics of the two autoencoders we consider for pretraining. Regular autoencoders pass samples through an encoder and then a decoder, attaching a reconstruction loss. The depth is double that of the encoder, which can make it difficult to train properly. We propose *shortcut autoencoders*, that separately passes samples through shortcuts, adding additional auxiliary reconstruction losses that converge faster.

used RBMs for layer-wise pretraining. Incidentally, the network that they trained this way was a multi-layer autoencoder for the purpose of dimensionality reduction. With improved techniques of training deep neural networks from scratch, layer-wise pretraining fell out of favor. None of the major milestone networks (AlexNet [62], VGG-16 [106], ResNet [41]) have since used such network priming. Attempts at making use of autoencoders in semi-supervised settings has continued [97, 108, 120, 137], but has largely alluded widespread success.

There are many variations on the regular autoencoder. Weights between the encoder and the decoder can be either separate or tied [122]. The Denoising Autoencoder [122, 123], a precursor to dropout [111], improves generalization by randomly zeroing out input features. One of the benefits of autoencoders (as opposed to for instance Principal Component Analysis) is the ease of experimenting with new losses and regularizations, such as adding sparsity regularization of the latent space [87]. In Transforming Autoencoders [42], the input image and the target image are different according to a transformation whose parameters are fed to the network. This promotes a more organized feature space. Regular autoencoders are not suited for generating samples, since we would need to know how to meaningfully sample the latent distribution. This is addressed in Variational Autoencoders [59], where the encoder instead of a latent vector produces sufficient statistics of a distribution that are then used to sample the latent vector. The statistics are regularized toward preset values (*e.g.*, unit normal), so that latent vectors can be sampled directly from this distribution. Another attempt at improving autoencoders for generative purposes trains the autoencoder to be one link in a Markov chain [8].

### 1.3.2 *Shortcut Autoencoder*

We have seen the loss of a regular autoencoder in (1.10). This can be non-trivial to train due to the total depth of combining both encoder and decoder. Let  $\ell_k$  denote the recon-

struction error when passing a sample through only the  $k$  first encoding layers and then the corresponding decoding layers:

$$\ell_k(x) = \|x - \hat{x}_k\|, \quad \hat{x}_k = (g_1 \circ \cdots \circ g_k \circ f_k \circ \cdots \circ f_1)(x), \quad (1.11)$$

where  $f_k$  is the  $k$ :th layer of the encoder and  $g_k$  the corresponding decoder layer. A regular autoencoder is thus  $\ell = \ell_L$ , where  $L$  is the number of layers. The Shortcut Autoencoder adds one or several auxiliary  $\ell_l$  to the objective:

$$\ell(x) = \ell_L(x) + \lambda \sum_{k \in \mathcal{L}} \ell_k(x) \quad (1.12)$$

The  $\mathcal{L}$  defines which layers get shortcut losses (does not need to be exhaustive) and  $\lambda$  regulates their importance (we use  $\lambda = 1$ ). The auxiliary losses can be implemented by building separate truncated networks that share weights with the full loss ( $\ell_L$ ) and the other shortcut losses. The shallow losses train faster and make it easier for the deeper paths to converge.

There are a few approaches that resemble this technique. Bengio *et al.* [7] used shallow autoencoders to train a deep network in a greedy manner. This starts by training for  $\ell_1$  and freezing the parameters of  $f_1$ . Next, a shallow encoder is trained on top of the second layer, with  $f_1(x)$  as the input. This is different, although reminiscent, to training for  $\ell_2$  without updating the parameters of layer 1. If this had been done, it would have been a close sequential analog of our proposed method. Shortcut connections in autoencoders are not new [77, 120]. However, the paths in those works are part of the network architecture with aggregation of the main path and the shortcut paths, for instance using element-wise means [77]. An alternative to shortcuts is to try to make activations synchronized between the encoder and the decoder through  $L_2$  losses. This idea of synchronizing activations is similarly used in FitNets [99], where the activations of a deep model tries to mimic that of

Method	Classification (%mAP)	Segmentation (%mIU)
No pretraining	46.2	23.5
Autoencoder	50.8	26.0
Shortcut Autoencoder	53.3	28.7
Layer-wise $k$ -means [27, 61]	56.6	32.6

Table 1.3: **Autoencoders for pretraining.** Autoencoders may slightly help, but the benefits are modest. Adding shortcuts makes convergence faster and offers slightly improved results. However, the improvements are so modest that it is hard to know if meaningful semantic knowledge was internalized during the pretraining phase, or if the parameter statistics simply offered a better and more even initialization. We also include results from a method of using  $k$ -means to initialize the network. This is similar to the idea of using stacked mixture models (section 1.2) as a starting point for end-to-end fine-tuning.

a shallow. We did not find success with such regularization and results were consistently worse. Our approach of not promoting synchronization explicitly, but instead implicitly by requiring subsequent layers to deal with both paths, was inspired by our work on fractal networks [69].

### 1.3.3 Baseline Results

We evaluate autoencoders as a method of pretraining by taking the encoder and using it as a starting point for a downstream task. For this, we use two standard benchmarks: VOC 2007 Classification and VOC 2012 Semantic Segmentation. We revisit these benchmarks in chapters 3 and 4, providing more training and network details. For now, it is worth knowing that we allow end-to-end fine-tuning of the pretrained network. This allows us to directly compare results against randomly initializing the network.

The encoder uses AlexNet [62] and in the case of shortcuts we place them at `conv2`, `conv4`, `fc6`. We do not use a dedicated hidden representation  $z$  as fig. 1.5 suggests. We tried this, but found that using `fc7` directly for this purpose yields slightly better results. This still creates a bottleneck since 4,096 features is 2.6% of the input feature size. The

notion of a single central bottleneck also lacks nuance. Adding dropout, which we use, is another way of limiting information bandwidth throughout the entire network (an idea rooted in DAE [122] and expanded in Ladder Networks [120]).

Results are shown in table 1.3. Regular autoencoders offer a modest improvement over random initialization. This is somewhat improved by adding shortcuts, which also makes the network converge faster. However, it still does not perform better than using layer-wise  $k$ -means to initialize the layers, which is similar to if we had initialized the network with a stacked mixture model from section 1.2. Both results are still not satisfactory and these numbers serve to show how difficult it is to prime a network using unlabeled data. We will revisit this in chapter 3 and show that self-supervision is a much more effective method of unsupervised pretraining.



## CHAPTER 2

# AUTOMATIC COLORIZATION

Leaving representation learning aside, we develop a method of automatic colorization and evaluate its use as a graphics application: a way to revitalize old black-and-white photographs. We return to unsupervised learning in chapter 3, where we will use our colorization network to drive representation learning.

### 2.1 Introduction

Colorization of grayscale images is a simple task for the human imagination. A human need only recall that sky is usually blue and grass is green; for many objects, the mind is free to hallucinate any of several plausible colors. The high-level comprehension required for this process is precisely why the development of fully automatic colorization algorithms is challenging. Colorization is therefore intriguing beyond its immediate practical utility in many graphics applications. Automatic colorization serves as a proxy measure for visual understanding. Our work makes this connection explicit; we unify a colorization pipeline with the type of deep neural network architectures driving advances in image classification and object detection.

Both our technical approach and focus on fully automatic results depart from past work. Given colorization’s importance across multiple applications (*e.g.*, historical photographs and videos [117], artist assistance [95, 113]), much research strives to make it cheaper and less time-consuming [13, 18, 19, 23, 38, 54, 71, 83, 125]. However, most methods still require some level of user input [13, 19, 38, 54, 71, 103]. Our work joins the relatively few recent efforts on developing fully automatic colorization algorithms [18, 23, 83]. Some [18, 23] show promising results, especially on photos of certain typical scene types (*e.g.*, beaches and landscapes). However, their success is limited on complex images with foreground objects.

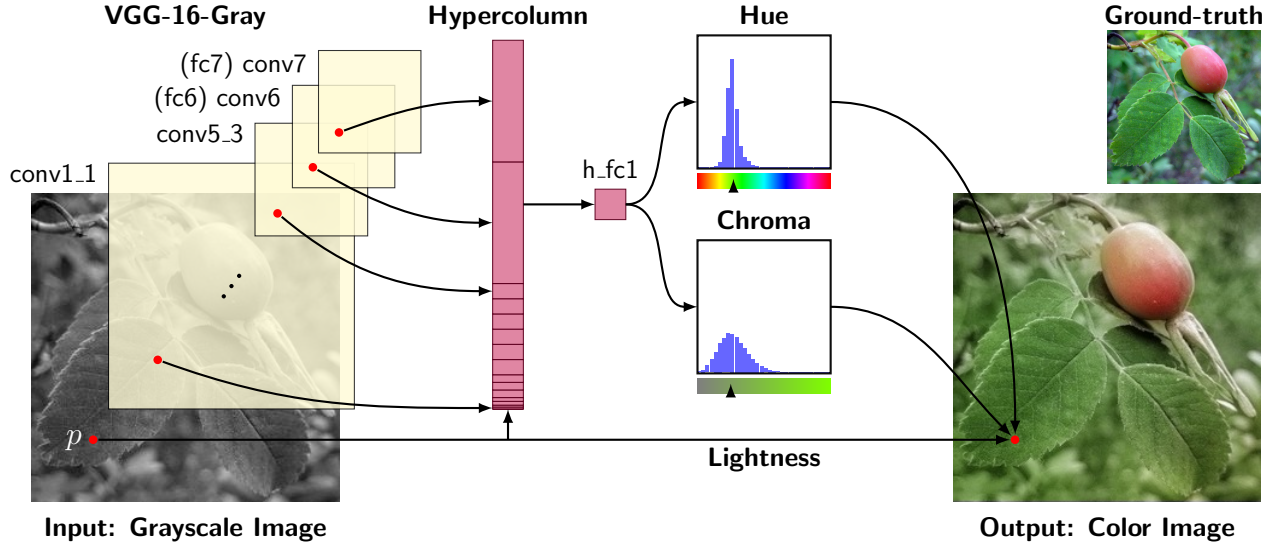


Figure 2.1: **System overview.** We process a grayscale image through a deep convolutional architecture (VGG-16) [106] and take spatially localized multilayer slices (hypercolumns) [39, 76, 84], as per-pixel descriptors. We train our system end-to-end for the task of predicting hue and chroma distributions for each pixel  $p$  given its hypercolumn descriptor. These predicted distributions determine color assignment at test time.

At a technical level, existing automatic colorization methods often employ a strategy of finding suitable reference images and transferring their color onto a target grayscale image [23, 83]. This works well if sufficiently similar reference images can be found, which becomes increasingly difficult for unique grayscale input images. Such a strategy also requires availability and search of a large repository of reference images at test time. In contrast, our approach is entirely free from database search and fast at test time. Section 2.2 provides a more complete view of prior methods, highlighting differences with our proposed algorithm.

Our approach to fully automatic colorization converts two intuitive observations into design principles. First, semantic information matters. In order to colorize arbitrary images, a system must interpret the semantic composition of the visual scene (what is in the image: faces, animals, cars, plants, etc.) as well as localize scene components (where things are). Recent dramatic advances in image understanding rely on deep convolutional neural networks (CNNs) and offer tools to incorporate semantic parsing and localization into a colorization

system.

Our second observation is that while some scene elements can be assigned a single color with high confidence, other elements (*e.g.*, clothes or cars) may draw from many suitable colors. Thus, we design our system to predict a color histogram, instead of a single color, at every image location. Figure 2.1 sketches the CNN architecture we use to connect semantics with color distributions by exploiting features across multiple abstraction levels. Section 2.3 provides details.

Section 2.4 reports extensive experimental validation of our algorithm against competing methods [23, 125] in two settings: fully (grayscale input only) and partially (grayscale input and reference global color histogram provided) automatic colorization. Across every benchmark metric and every dataset [93, 100, 128], our method achieves the best performance. Lacking an established standard colorization benchmark, exhaustive comparison is necessary. To ease this burden for future research, we propose a new colorization benchmark on the ImageNet dataset [100], which may simplify quantitative comparisons and drive further progress. Our system achieves such a drastic performance leap that its fully automatic colorization output is superior to that of prior methods relying on additional information such as reference images or ground-truth color histograms.

Section 2.5 summarizes our contributions:

- A novel technical approach to colorization, bringing semantic knowledge to bear using CNNs, and modeling color distributions.
- State-of-the-art performance across fully and partially automatic colorization tasks.
- A new ImageNet colorization benchmark.

## 2.2 Related work

Previous colorization methods broadly fall into three categories: scribble-based [48, 71, 75, 95, 132], transfer [13, 19, 38, 54, 83, 114, 125], and automatic direct prediction [18, 23].

*Scribble-based* methods, first introduced by Levin *et al.* [71], require manually specifying desired colors of certain regions. These scribble colors are propagated under the assumption that adjacent pixels with similar luminance should have similar color, with the optimization relying on Normalized Cuts [105]. Users can interactively refine results via additional scribbles. Further advances extend similarity to texture [75, 95], and exploit edges to reduce color bleeding [48].

*Transfer-based* methods rely on availability of related *reference* image(s), from which color is transferred to the target grayscale image. Mapping between source and target is established automatically, using correspondences between local descriptors [13, 83, 125], or in combination with manual intervention [19, 54]. Excepting [83], reference image selection is at least partially manual.

In contrast to these method families, our goal is *fully automatic* colorization. We are aware of two recent efforts in this direction. Deshpande *et al.* [23] colorize an entire image by solving a linear system. This can be seen as an extension of patch-matching techniques [125], adding interaction terms for spatial consistency. Regression trees address the high-dimensionality of the system. Inference requires an iterative algorithm. Most of the experiments are focused on a dataset (SUN-6) limited to images of a few scene classes, and best results are obtained when the scene class is known at test time. They also examine another partially automatic task, in which a desired global color histogram is provided.

The work of Cheng *et al.* [18] is perhaps most related to ours. It combines three levels of features with increasing receptive field: the raw image patch, DAISY features [116], and semantic features [74]. These features are concatenated and fed into a three-layer fully connected neural network trained with an  $L_2$  loss. Only this last component is optimized;

the feature representations are fixed.

Unlike [18, 23], our system does not rely on hand-crafted features, is trained end-to-end, and treats color prediction as a histogram estimation task rather than as regression. Experiments in Section 2.4 justify these principles by demonstrating performance superior to the best reported by [18, 23] across all regimes.

Two concurrent efforts also present feed-forward networks trained end-to-end for colorization. Iizuka & Simo-Serra *et al.* [51] propose a network that concatenates two separate paths, specializing in global and local features, respectively. This concatenation can be seen as a two-tiered hypercolumn; in comparison, our 16-layer hypercolumn creates a continuum between low- and high-level features. Their network is trained jointly for classification (cross-entropy) and colorization ( $L_2$  loss in Lab). We initialize, but do not anchor, our system to a classification-based network, allowing for fine-tuning of colorization on unlabeled datasets. This is also what enables us to use colorization for representation learning in chapter 3.

Zhang *et al.* [135] similarly propose predicting color histograms to handle multimodality. Some key differences include their usage of up-convolutional layers, deep supervision, and dense training. In comparison, we use a fully convolutional approach, with deep supervision implicit in the hypercolumn design, and, as Section 2.3 describes, memory-efficient training via spatially sparse samples.

## 2.3 Method

We frame the colorization problem as learning a function  $f : \mathcal{X} \rightarrow \mathcal{Y}$ . Given a grayscale image patch  $\mathbf{x} \in \mathcal{X} = [0, 1]^{S \times S}$ ,  $f$  predicts the color  $\mathbf{y} \in \mathcal{Y}$  of its center pixel. The patch size  $S \times S$  is the receptive field of the colorizer. The output space  $\mathcal{Y}$  depends on the choice of color parameterization. We implement  $f$  according to the neural network architecture diagrammed in fig. 2.1.

Motivating this strategy is the success of similar architectures for semantic segmenta-

tion [15, 32, 39, 74, 84] and edge detection [10, 34, 76, 104, 129]. Together with colorization, these tasks can all be viewed as image-to-image prediction problems, in which a value is predicted for each input pixel. Leading methods commonly adapt deep convolutional neural networks pretrained for image classification [100, 106]. Such classification networks can be converted to *fully convolutional* networks that produce output of the same spatial size as the input, *e.g.* using the shift-and-stitch method [74] or the more efficient *à trous* algorithm [15]. Subsequent training with a task-specific loss fine-tunes the converted network.

Skip-layer connections, which directly link low- and mid-level features to prediction layers, are an architectural addition beneficial for many image-to-image problems. Some methods implement skip connections directly through concatenation layers [15, 74], while others equivalently extract per-pixel descriptors by reading localized slices of multiple layers [39, 76, 84]. We use this latter strategy and adopt the recently coined *hypercolumn* terminology [39] for such slices.

Though we build upon these ideas, our technical approach innovates on two fronts. First, we integrate domain knowledge for colorization, experimenting with output spaces and loss functions. We design the network output to serve as an intermediate representation, appropriate for direct or biased sampling. We introduce an energy minimization procedure for optionally biasing sampling towards a reference image. Second, we develop a novel and efficient computational strategy for network training that is widely applicable to hypercolumn architectures.

### 2.3.1 Color Spaces

We generate training data by converting color images to grayscale according to  $L = \frac{R+G+B}{3}$ . This is only one of many desaturation options and chosen primarily to facilitate comparison with Deshpande *et al.* [23]. For the representation of color predictions, using RGB is over-determined, as lightness  $L$  is already known. We instead consider output color spaces with  $L$

(or a closely related quantity) conveniently appearing as a separate pass-through channel:

- **Hue/chroma.** Hue-based spaces, such as HSL, can be thought of as a color cylinder, with angular coordinate  $H$  (hue), radial distance  $S$  (saturation), and height  $L$  (lightness). The values of  $S$  and  $H$  are unstable at the bottom (black) and top (white) of the cylinder. HSV describes a similar color cylinder which is only unstable at the bottom. However,  $L$  is no longer one of the channels. We wish to avoid both instabilities and still retain  $L$  as a channel. The solution is a color bicone, where chroma ( $C$ ) takes the place of saturation. Conversion to HSV is given by  $V = L + \frac{C}{2}$ ,  $S = \frac{C}{V}$ .
- **Lab and  $\alpha\beta$ .** Lab (or L\*a\*b) is designed to be perceptually linear. The color vector  $(a, b)$  defines a Euclidean space where the distance to the origin determines chroma. Deshpande *et al.* [23] use a color space somewhat similar to Lab, denoted “ab”. To differentiate, we call their color space  $\alpha\beta$ .

### 2.3.2 Loss

For any output color representation, we require a loss function for measuring prediction errors. A first consideration, also used in [18], is  $L_2$  regression in the ab components of Lab:

$$L_{\text{reg}}(\mathbf{x}, \mathbf{y}) = \|f(\mathbf{x}) - \mathbf{y}\|^2 \quad (2.1)$$

where  $\mathcal{Y} = \mathbb{R}^2$  describes the  $(a, b)$  vector space. However, regression targets do not handle multimodal color distributions well. To address this, we instead predict distributions over a set of color bins, a technique also used in [13]:

$$L_{\text{hist}}(\mathbf{x}, \mathbf{y}) = D_{\text{KL}}(\mathbf{y} \| f(\mathbf{x})) \quad (2.2)$$

where  $\mathcal{Y} = [0, 1]^K$  describes a histogram over  $K$  bins, and  $D_{\text{KL}}$  is the KL divergence. The ground-truth histogram  $\mathbf{y}$  is set as the empirical distribution in a rectangular region of size  $R$  around the center pixel. We use  $R = 7$ , but experiments show that  $R = 1$  works well too; in the latter case the loss becomes the log loss. For histogram predictions, the last layer of neural network  $f$  is always a softmax.

There are several choices of how to bin the color space. We bin the Lab axes by evenly spaced Gaussian quantiles ( $\mu = 0, \sigma = 25$ ). They can be encoded separately for  $a$  and  $b$  (as marginal distributions), in which case our loss becomes the sum of two separate terms defined by (2.2). They can also be encoded as a joint distribution over  $a$  and  $b$ , in which case we let the quantiles form a 2D grid of bins. In our experiments, we set  $K = 32$  for marginal distributions and  $K = 16 \times 16$  for joint. We determined these numbers, along with  $\sigma$ , to offer a good compromise of output fidelity and output complexity.

For hue/chroma, we only consider marginal distributions and bin axes uniformly in  $[0, 1]$ . Since hue becomes unstable as chroma approaches zero, we add a sample weight to the hue based on the chroma:

$$L_{\text{hue/chroma}}(\mathbf{x}, \mathbf{y}) = D_{\text{KL}}(\mathbf{y}_C \| f_C(\mathbf{x})) + \lambda_H y_C D_{\text{KL}}(\mathbf{y}_H \| f_H(\mathbf{x})) \quad (2.3)$$

where  $\mathcal{Y} = [0, 1]^{2 \times K}$  and  $y_C \in [0, 1]$  is the sample pixel's chroma. We set  $\lambda_H = 5$ , roughly the inverse expectation of  $y_C$ , thus equally weighting hue and chroma.

### 2.3.3 Inference

Given network  $f$  trained according to a loss function in the previous section, we evaluate it at every pixel  $n$  in a test image:  $\hat{\mathbf{y}}_n = f(\mathbf{x}_n)$ . For the  $L_2$  loss, all that remains is to combine each  $\hat{\mathbf{y}}_n$  with the respective lightness and convert to RGB. With histogram predictions, we consider options for inferring a final color:





Figure 2.2: Artifacts without chromatic fading (*left*).

- **Sample** Draw a sample from the histogram. If done per pixel, this may create high-frequency noise in areas of high-entropy histograms.
- **Mode** Take the  $\arg \max_k \hat{y}_{n,k}$  as the color. This can create jarring transitions between colors, and is prone to vote splitting for proximal centroids.
- **Median** Compute cumulative sum of  $\hat{y}_n$  and use linear interpolation to find the value at the middle bin. Undefined for circular histograms, such as hue.
- **Expectation** Sum over the centroids of the color bins weighted by the histogram.

In the Lab color space, we achieve the best qualitative and quantitative results using expectations. For hue/chroma, the best results are achieved by taking the median of the chroma. Many objects can appear both with and without chroma, which means  $C = 0$  is a particularly common bin. This mode draws the expectation closer to zero, producing less saturated images. As for hue, since it is circular, we first compute the complex expectation:

$$z = \mathbb{E}_{H \sim f_h(\mathbf{x})}[H] \triangleq \frac{1}{K} \sum_k [f_h(x)]_k e^{i\theta_k}, \quad \theta_k = 2\pi \frac{k + 0.5}{K} \quad (2.4)$$

We then set hue to the argument of  $z$  remapped to lie in  $[0, 1)$ .

In cases where the estimate of the chroma is high and  $z$  is close to zero, the instability of the hue can create artifacts (fig. 2.2). A simple, yet effective, fix is chromatic fading:

downweight the chroma if the absolute value of  $z$  is too small. We thus re-define the predicted chroma as:

$$C_{\text{faded}} = \max(\eta^{-1}|z|, 1) \cdot C \quad (2.5)$$

In our experiments, we set  $\eta = 0.03$  (obtained via cross-validation).

### 2.3.4 Ground-Truth Histogram Transfer

So far, we have only considered the fully automatic color inference task. Deshpande *et al.* [23], test a separate task where the ground-truth histogram in the two non-lightness color channels of the original color image is made available.<sup>1</sup> In order to compare, we propose two histogram transfer methods. We refer to the predicted image as the *source* and the ground-truth image as the *target*.

**Lightness-normalized quantile matching.** Divide the RGB representation of both source and target by their respective lightness. Then, compute marginal histograms over the resulting three color channels. Alter each source histogram to fit the corresponding target histogram by quantile matching, and multiply by lightness. Though it does not exploit our richer color distribution predictions, quantile matching beats the cluster correspondence method of [23] (see table 2.4).

**Energy minimization.** We phrase histogram matching as minimizing energy:

$$E = \frac{1}{N} \sum_n D_{\text{KL}}(\hat{\mathbf{y}}_n^* || \hat{\mathbf{y}}_n) + \lambda D_{\chi^2}(\langle \hat{\mathbf{y}}^* \rangle, \mathbf{t}) \quad (2.6)$$

where  $N$  is the number of pixels,  $\hat{\mathbf{y}}, \hat{\mathbf{y}}^* \in [0, 1]^{N \times K}$  are the predicted and posterior distributions, respectively. The target histogram is denoted by  $\mathbf{t} \in [0, 1]^K$ . The first term

---

1. Note that if the histogram of the  $L$  channel were available, it would be possible to match lightness to lightness exactly and thus greatly narrow down color placement.

contains unary potentials that anchor the posteriors to the predictions. The second term is a symmetric  $\chi^2$  distance to promote proximity between source and target histograms. Weight  $\lambda$  defines relative importance of histogram matching. We estimate the source histogram as  $\langle \hat{\mathbf{y}}^* \rangle = \frac{1}{N} \sum_n \hat{\mathbf{y}}_n^*$ . We parameterize the posterior for all pixels  $n$  as:  $\hat{\mathbf{y}}_n^* = \text{softmax}(\log \hat{\mathbf{y}}_n + \mathbf{b})$ , where the vector  $\mathbf{b} \in \mathbb{R}^K$  can be seen as a global bias for each bin. It is also possible to solve for the posteriors directly; this does not perform better quantitatively and is more prone to introducing artifacts. We solve for  $\mathbf{b}$  using gradient descent on  $E$  and use the resulting posteriors in place of the predictions. In the case of marginal histograms, the optimization is run twice, once for each color channel.

### 2.3.5 Neural Network Architecture

Our base network is a fully convolutional version of VGG-16 [106] with two changes: (1) the classification layer (`fc8`) is discarded, and (2) the first filter layer (`conv1_1`) operates on a single intensity channel instead of mean-subtracted RGB. We extract a hypercolumn descriptor for a pixel by concatenating the features at its spatial location in all layers, from `data` to `conv7` (`fc7`), resulting in a 12,417 channel descriptor. We feed this hypercolumn into a fully connected layer with 1024 channels (`h_fc1` in fig. 2.1), to which we connect output predictors.

We initialize with a version of VGG-16 pretrained on ImageNet, adapting it to grayscale by averaging over color channels in the first layer and rescaling appropriately. Prior to training for colorization, we further fine-tune the network for one epoch on the ImageNet classification task with grayscale input. As the original VGG-16 was trained without batch normalization [53], scale of responses in internal layers can vary dramatically, presenting a problem for learning atop their hypercolumn concatenation. Liu *et al.* [73] compensate for such variability by applying layer-wise  $L_2$  normalization. We use an alternative that we call re-balancing the network.

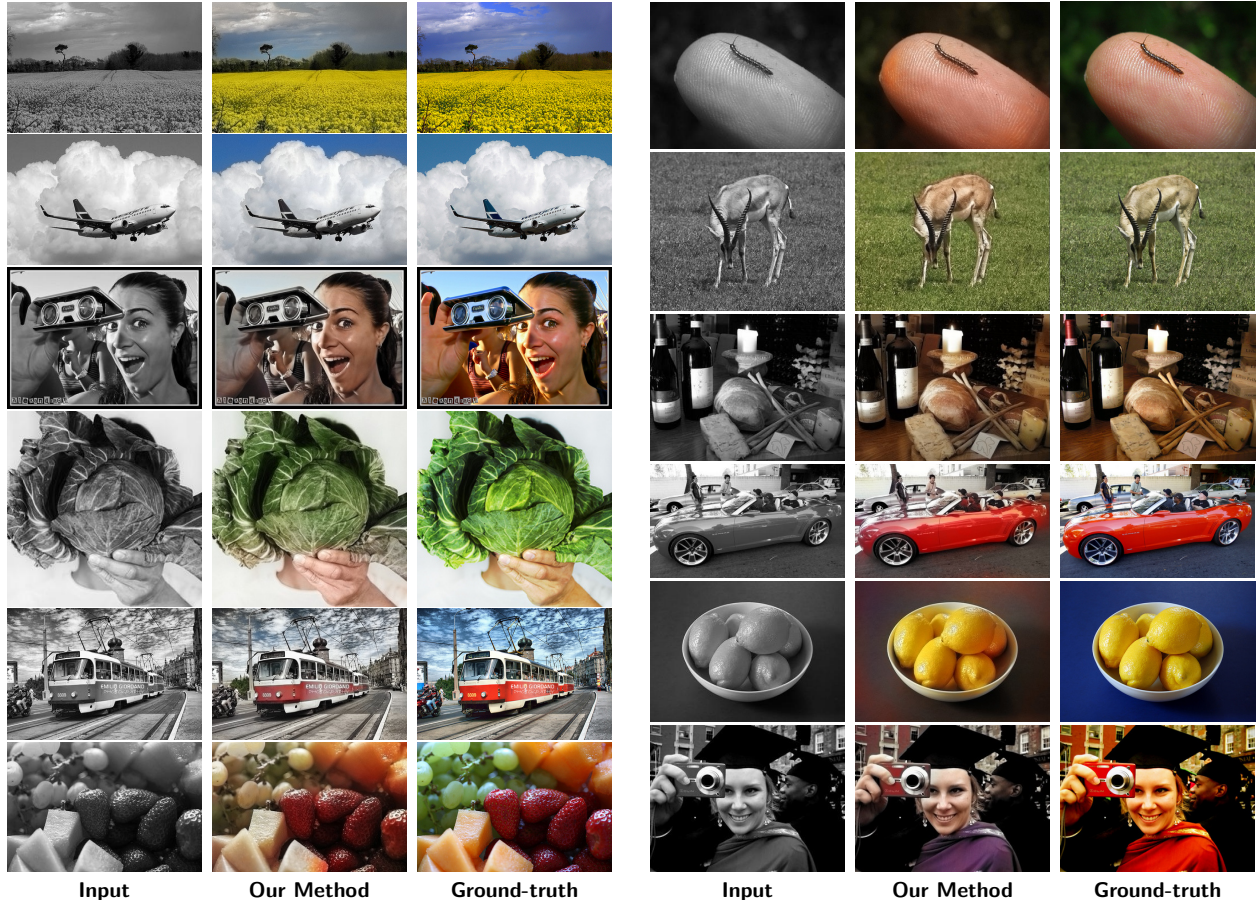


Figure 2.3: **Fully automatic colorization results on ImageNet/ctest10k.** Our system reproduces known object color properties (*e.g.*, faces, sky, grass, fruit, wood), and coherently picks colors for objects without such properties (*e.g.*, clothing).

### 2.3.6 Network Re-Balancing

Before colorization training begins, we take the ImageNet pretrained network and shift weights around such that each layer’s activation has roughly unit second moment ( $\mathbb{E}[X^2] \approx 1$ ). This is made possible thanks to ReLU activations, which are piecewise linear around zero. To adjust the scale of the activations of layer  $l$  by factor  $m$ , without changing any other layer’s activation, the weights  $\mathbf{W}$  and the biases  $\mathbf{b}$  are updated according to:

$$\mathbf{W}_l \leftarrow m\mathbf{W}_l, \quad \mathbf{b}_l \leftarrow m\mathbf{b}_l, \quad \mathbf{W}_{l+1} \leftarrow \frac{1}{m}\mathbf{W}_{l+1} \quad (2.7)$$

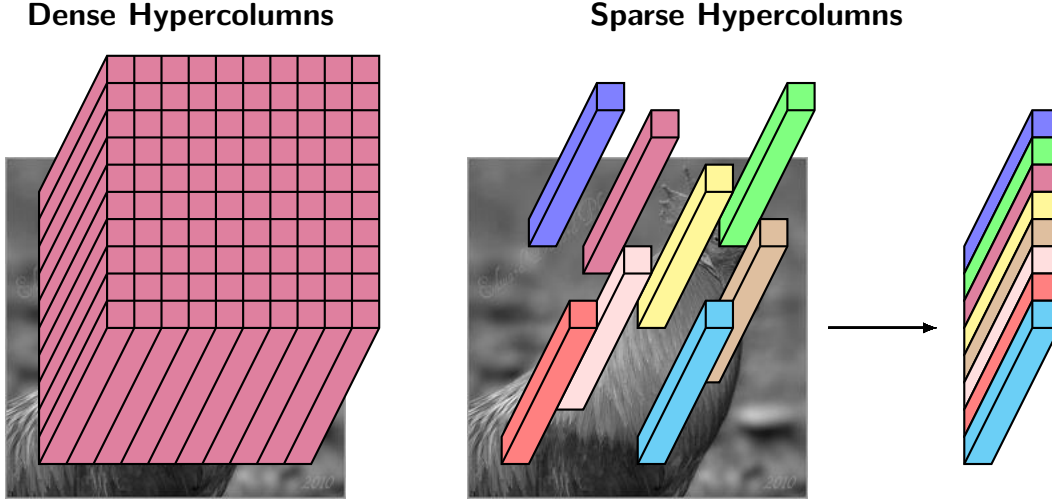


Figure 2.4: **Dense vs. sparse hypercolumns.** To compute a hypercolumn for each pixel in an image, all intermediate layers are resampled and concatenated (left). This has a large memory footprint, but is necessary if we want to colorize all pixels in an image. However, during training, we have found that a sparse sample of hypercolumns that are computed with direct bilinear sampling works equally well and reduces memory usage (right). See table 2.1 for experimental results.

It is easy to show that the activations of layer  $l + 1$  are invariant to  $m$ , while the activations of layer  $l$  change by a factor of  $m$ . We set  $m = \frac{1}{\sqrt{\mathbb{E}[X^2]}}$ , estimated for each layer separately.

### 2.3.7 Dense vs. Sparse Sampling

Computing the hypercolumn for all pixels in an image can be done by re-sampling all layers to a fixed size and concatenating along the feature axis. The fixed size does not have to be the size of the original input and can instead be smaller. For instance, to make the colorizer fast at test time, we recommend setting the target size to a factor 4 smaller than the input size. The image containing the two color channels are finally upsampled and combined with the original-sized lightness channel. Color channels contain far less high-frequency signal than the intensity channel, so this incurs a minimum degradation to the results.

Producing a densely sampled map of hypercolumns is quite fast. At least if we use bilinear resampling and execute it on the GPU with fast convolutional kernels. However, the

Samples/image	Segmentation (%mIU)
1	$54.5 \pm 0.4$
4	$63.6 \pm 0.4$
16	$67.6 \pm 0.4$
64	$68.5 \pm 0.2$
256	$69.2 \pm 0.3$
1024	$68.9 \pm 0.5$

Table 2.1: **Hypercolumn sparsity.** We evaluate on VOC 2012 semantic segmentation (val) the effectiveness of sparse samples. We train on large inputs ( $448 \times 448$ ) made possible by the memory savings. Measurable benefits stop around 256 samples. This is only 0.1% of the pixels in the image and still only 2% if we downsample our dense map by a factor 4.

memory footprint is high and a single hypercolumn together with subsequent layer `h_fc1` (with gradients at single precision) takes about 100 KiB. A dense sampling of a  $256 \times 256$  image would take 6.7 GiB. Reducing the target image to  $64 \times 64$  reduces it to 430 MiB. However, this is per image, so even a batch size of 10 would fill a third of our memory on a 12 GiB GPU. Even worse, depending on the implementation and the software used, intermediate values prior to concatenation often require space too.

Instead, we have discovered that extracting hypercolumns at only a sparse set of locations is good enough during training. The values of each hypercolumn can be computed directly using bilinear interpolation and organized as if it were non-spatial data (see fig. 2.4). A custom layer performs the sparse extraction, which we have made available for both Caffe [57] and TensorFlow [1].<sup>2</sup> In the backward pass, gradients are propagated to the four closest spatial cells involved in the bilinear interpolation. Locks ensure atomicity of gradient updates, without incurring any measurable performance penalty.

We investigate in table 2.1 how many samples suffice when applying sparse samples on the VOC 2012 Semantic Segmentation [30] benchmark. We train on large inputs ( $448 \times 448$ ), afforded by the sparse sampling. After around 256 samples, there is no gain to optimization by increasing sample locations further. This is likely due to the high correlation between the hypercolumns of a single image. The top convolutional layers (`fc6/conv6` and `fc7/conv7`) arguably need the most samples to converge properly. However, even at our input size, these

2. <https://github.com/gustavla/autocolorize>

Model\Metric	RMSE	PSNR
No colorization	0.343	22.98
Lab, $L_2$	0.318	24.25
Lab, $K = 32$	0.321	24.33
Lab, $K = 16 \times 16$	0.328	24.30
Hue/chroma, $K = 32$	0.342	23.77
+ chromatic fading	<b>0.299</b>	<b>24.45</b>

Table 2.2: **ImageNet/cval1k**. Validation performance of system variants. Hue/chroma is best, but only with chromatic fading.

Model\Metric	RMSE	PSNR
data.. <b>fc7</b>	<b>0.299</b>	<b>24.45</b>
data.. <b>conv5_3</b>	0.306	24.13
<b>conv4_1..fc7</b>	0.302	<b>24.45</b>
<b>conv5_1..fc7</b>	0.307	24.38
<b>fc6..fc7</b>	0.323	24.22
<b>fc7</b>	0.324	24.19

Table 2.3: **ImageNet/cval1k**. Ablation study of hypercolumn components.

layers are reduced to  $14 \times 14$  spatial dimensions, containing only 192 distinct elements. At 256 samples, we thus get a complete sample of the high level features, at the cost of only 26 MiB per image.

Sparse sampling also makes it easy and cheap to extract pairs or triplets of hypercolumns. In section 4.7.1 we use this to predict relative optical flow between pairs of locations.

## 2.4 Experiments

Starting from pretrained VGG-16-Gray, described in the previous section, we attach **h\_fc1** and output prediction layers with Xavier initialization [35], and fine-tune the entire system for colorization. We consider multiple prediction layer variants: Lab output with  $L_2$  loss, and both Lab and hue/chroma marginal or joint histogram output with losses according to eqs. (2.2) and (2.3). We train each system variant end-to-end for one epoch on the 1.3M images of the ImageNet training set, each resized to at most 256 pixels in smaller dimension. A single epoch takes approximately 17 hours on a GTX Titan X GPU. At test time, colorizing a single  $512 \times 512$  pixel image takes 0.5 seconds.

We create two disjoint subsets of the ImageNet validation data for our own use: 1,000 validation images (**cval1k**) and 10,000 test images (**ctest10k**). Each set has a balanced representation for ImageNet categories, and excludes any images encoded as grayscale, but



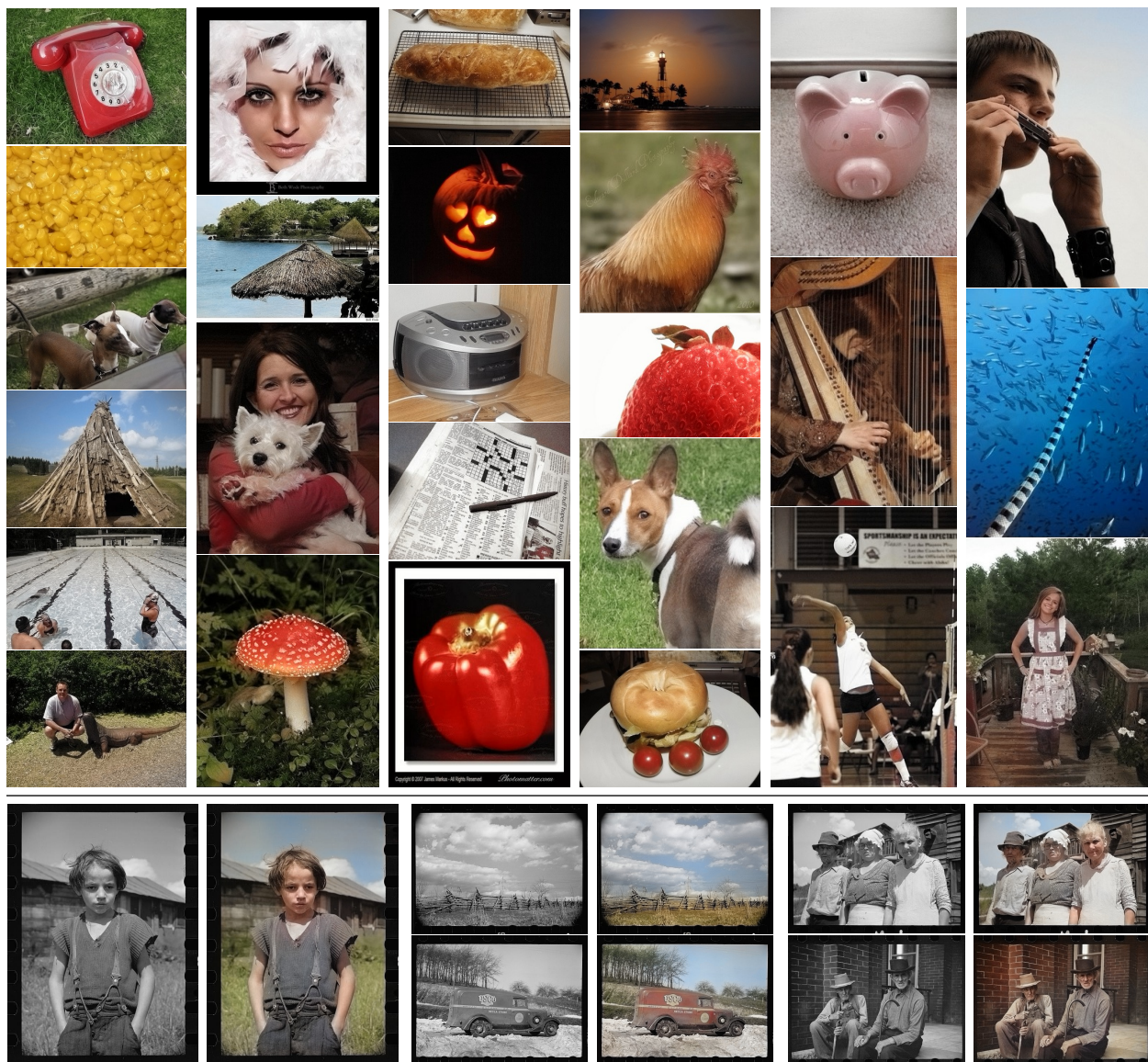


Figure 2.5: **Additional colorization results.** *Top:* Our automatic colorizations of these ImageNet examples are difficult to distinguish from real color images. *Bottom:* B&W photographs.



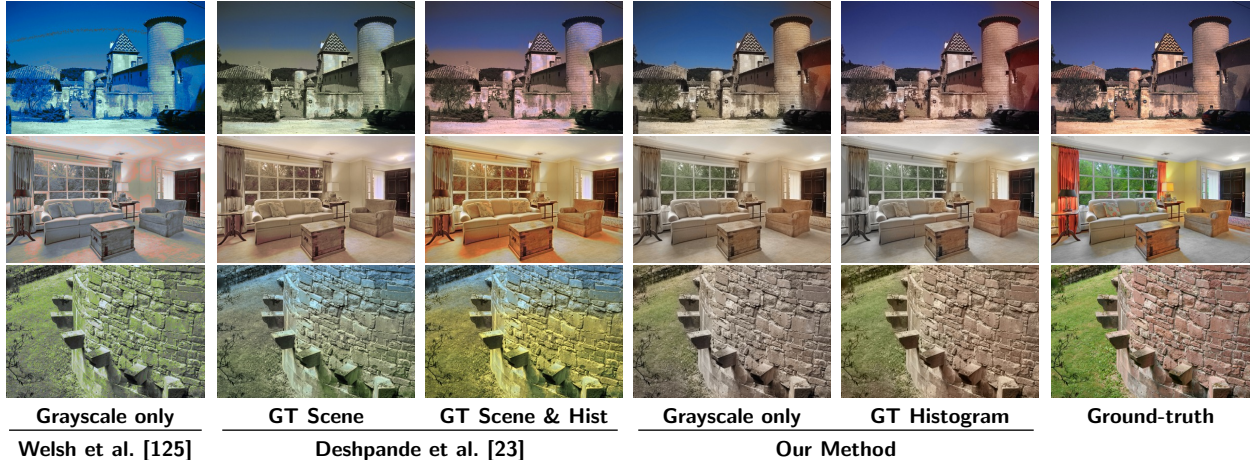


Figure 2.6: **Examples on SUN-6.** GT Scene: test image scene class is available. GT Hist: test image color histogram is available. We obtain colorizations with visual quality better than those from prior work, even though we do not exploit reference images or known scene class. Our energy minimization method (Section 2.3.4) for GT Hist further improves results. In either mode, our method appears less dependent on spatial priors: note splitting of the sky in the first row and correlation of green with actual grass in the last row.

may include images that are naturally grayscale (*e.g.*, closeup of nuts and bolts), where an algorithm should know not to add color. Category labels are discarded; only images are available at test time. We propose **cctest10k** as a standard benchmark with the following metrics:

- **RMSE**: root mean square error in  $\alpha\beta$  averaged over all pixels [23].
- **PSNR**: peak signal-to-noise ratio in RGB calculated per image [18]. We use the arithmetic mean of PSNR over images, instead of the geometric mean as in Cheng *et al.* [18]; geometric mean is overly sensitive to outliers.

By virtue of comparing to ground-truth color images, quantitative colorization metrics can penalize reasonable, but incorrect, color guesses for many objects (*e.g.*, red car instead of blue car) more than jarring artifacts. This makes qualitative results for colorization as important as quantitative; we report both.

Figures 2.3 and 2.5 show example test results of our best system variant, selected accord-

ing to performance on the validation set and trained for a total of 10 epochs. This variant predicts hue and chroma and uses chromatic fading during image generation.

Table 2.2 provides complete validation benchmarks for all system variants, including the trivial baseline of no colorization (returning the grayscale input). On ImageNet test (**ctest10k**), our selected model obtains 0.293 (RMSE,  $\alpha\beta$ , avg/px) and 24.94 dB (PSNR, RGB, avg/im), compared to 0.333 and 23.27 dB for the no colorization baseline.

Table 2.3 examines the importance of different neural network layers to colorization; it reports validation performance of ablated systems that include only the specified subsets of layers in the hypercolumn used to predict hue and chroma. Some lower layers may be discarded without much performance loss, yet higher layers alone (**fc6..fc7**) are insufficient for good colorization.

Our ImageNet colorization benchmark is new to a field lacking an established evaluation protocol. We therefore focus on comparisons with two recent papers [18, 23], using their self-defined evaluation criteria. To do so, we run our ImageNet-trained hue and chroma model on two additional datasets:

- **SUN-A** [93] is a subset of the SUN dataset [128] containing 47 object categories. Cheng *et al.* [18] train a colorization system on 2688 images and report results on 1344 test images. We were unable to obtain the list of test images, and therefore report results averaged over five random subsets of 1344 SUN-A images. We do not use any SUN-A images for training.
- **SUN-6**, another SUN subset, used by Deshpande *et al.* [23], includes images from six scene categories (beach, castle, outdoor, kitchen, living room, bedroom). We compare our results on 240 test images to those reported in [23] for their method as well as for Welsh *et al.* [125] with automatically matched reference images as in [83]. Following [23], we consider another evaluation regime in which ground-truth target color histograms are available.

Method	RMSE
Grayscale (no colorization)	0.285
Welsh <i>et al.</i> [125]	0.353
Deshpande <i>et al.</i> [23]	0.262
+ GT Scene	0.254
Our Method	<b>0.211</b>

Table 2.4: **SUN-6**. Comparison with competing methods.

Method	RMSE
Deshpande <i>et al.</i> (C) [23]	0.236
Deshpande <i>et al.</i> (Q)	0.211
Our Method (Q)	0.178
Our Method (E)	<b>0.165</b>

Table 2.5: **SUN-6 (GT Hist)**. Comparison using ground-truth histograms. Results for Deshpande *et al.* [23] use GT Scene.

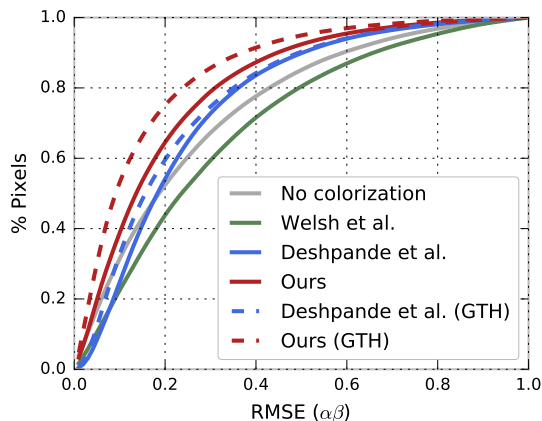


Figure 2.7: **SUN-6**. Cumulative histogram of per-pixel error (higher means more pixels with lower error). Results for Deshpande *et al.* [23] use GT Scene.

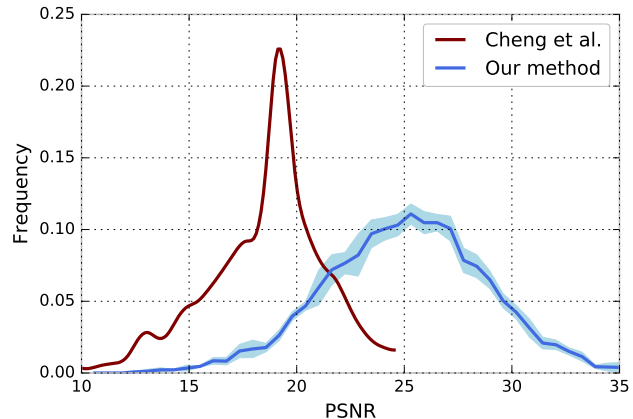


Figure 2.8: **SUN-A**. Histogram of per-image PSNR for [18] and our method. The highest geometric mean PSNR reported for experiments in [18] is 24.2, vs. our **32.7 ± 2.0**.

Figure 2.6 shows a comparison of results on SUN-6. Forgoing usage of ground-truth global histograms, our fully automatic system produces output qualitatively superior to methods relying on such side information. Tables 2.4 and 2.5 report quantitative performance corroborating this view. The partially automatic systems in table 2.5 adapt output to fit global histograms using either: (C) cluster correspondences [23], (Q) quantile matching, or (E) our energy minimization described in section 2.3.4. Our quantile matching results are superior to those of [23] and our new energy minimization procedure offers further improvement.

Figures 2.7 and 2.8 compare error distributions on SUN-6 and SUN-A. As in Table 2.4, our fully automatic approach dominates all competing methods, even those which use aux-

iliary information. It is only outperformed by the version of itself augmented with ground-truth global histograms. On SUN-A, Figure 2.8 shows clear separation between our method and [18] on per-image PSNR.

With regard to concurrent work, Zhang *et al.* [135] include a comparison of our results to their own. The two systems are competitive in terms of quantitative measures of colorization accuracy. Their system, set to produce more vibrant colors, has an advantage in terms of human-measured preferences. In contrast, an off-the-shelf VGG-16 network for image classification, consuming our system’s color output, more often produces correct labels, suggesting a realism advantage. We refer interested readers to [135] for the full details of this comparison.

Though we achieve significant improvements over prior state-of-the-art, our results are not perfect. Figure 2.9 shows examples of significant failures. Minor imperfections are also present in some of the results in Figures 2.3 and 2.5. We believe a common failure mode correlates with gaps in semantic interpretation: incorrectly identified or unfamiliar objects and incorrect segmentation. In addition, there are “mistakes” due to natural uncertainty of color – *e.g.* the graduation robe at the bottom right of Figure 2.3 is red, but could as well be purple.

Since our method produces histograms, we can provide interactive means of biasing colorizations according to user preferences. Rather than output a single color per pixel, we can sample color for image regions and evaluate color uncertainty. Specifically, solving our energy minimization formulation (Equation 2.6) with global biases  $\mathbf{b}$  that are not optimized based on a reference image, but simply “rotated” through color space, induces changed color preferences throughout the image. The uncertainty in the predicted histogram modulates this effect.

Figure 2.10 shows multiple sampled colorizations, together with a visualization of uncertainty. Here, uncertainty is the entropy of the predicted hue multiplied by the chroma. Our

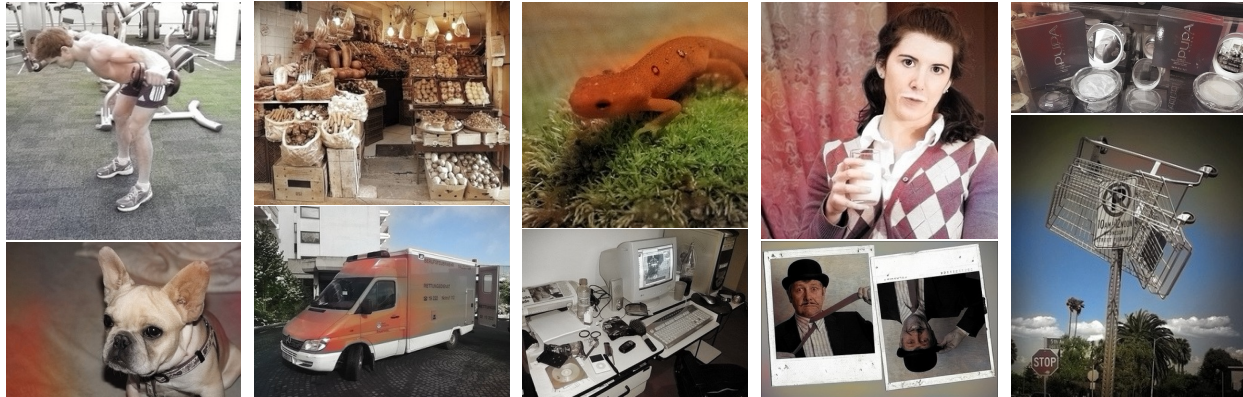


Figure 2.9: **Failure modes.** *Top row, left-to-right:* texture confusion, too homogeneous, color bleeding, unnatural color shifts ( $\times 2$ ). *Bottom row:* inconsistent background, inconsistent chromaticity, not enough color, object not recognized (upside down face partly gray), context confusion (sky).



Figure 2.10: **Sampling multiple colorizations.** *Left:* Image and 3 samples; *Right:* Uncertainty map.

distributional output and energy minimization framework open the path for future investigation of human-in-the-loop colorization tools.

## 2.5 Conclusion

We present a system that demonstrates state-of-the-art ability to automatically colorize grayscale images. Two novel contributions enable this progress: a deep neural architecture that is trained end-to-end to incorporate semantically meaningful features of varying complexity into colorization, and a color histogram prediction framework that handles uncertainty and ambiguities inherent in colorization while preventing jarring artifacts. Our fully automatic colorizer produces strong results, improving upon previously leading methods by large margins on all datasets tested; we also propose a new large-scale benchmark for

automatic image colorization, and establish a strong baseline with our method to facilitate future comparisons. Our colorization results are visually appealing even on complex scenes, and allow for effective post-processing with creative control via color histogram transfer and intelligent, uncertainty-driven color sampling.

In chapter 3, we reveal that colorization has utility beyond its immediate application as a promising avenue for self-supervised visual learning.

## CHAPTER 3

### SELF-SUPERVISED REPRESENTATION LEARNING

Returning to representation learning, we demonstrate in this chapter how colorization can be used for self-supervised representation learning and how it relates and compares to supervised pretraining.

#### 3.1 Introduction

The success of deep feed-forward networks is rooted in their ability to scale up with more training data. The availability of more data can generally afford an increase in model complexity. However, this need for expensive, tedious and error-prone human annotation is severely limiting, reducing our ability to build models for new domains, and for domains in which annotations are particularly expensive (e.g., image segmentation). At the same time, we have access to enormous amounts of unlabeled visual data, which is essentially free. This work is an attempt to improve means of leveraging this abundance. We manage to bring it one step closer to the results of using labeled data, but the eventual long term goal of self-supervision may be to supplant supervised pretraining completely.

Alternatives to supervised training that do not need labeled data have seen limited success, as demonstrated in chapter 1. Unsupervised learning methods, such as compressed embeddings trained by minimizing reconstruction error, have seen more success in image synthesis [59], than for representation learning. Semi-supervised learning, jointly training a supervised and an unsupervised loss, offers a middle ground [36, 101]. However, recent works tend to prefer a sequential combination instead (unsupervised pretraining, supervised fine-tuning) [25, 27], possibly because it prevents the unsupervised loss from being disruptive in the late stages of training. Perhaps more importantly, it reduces the engineering and computational burden if a pretrained network is widely disseminated. A related endeavor to un-



## Learning a representation via $(x, y)$ pairs

### Classification

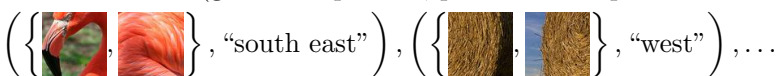


### Self-supervision

Ex. 1: **Inpainting** (remove patch and then predict it)



Ex. 2: **Context** (given two patches, predict their spatial relation)



Ex. 3: **Colorization** (predict color given intensity)



Figure 3.1: **Self-supervision.** Using a representation that was originally trained for classification on  $(x, y)$  pairs to initialize a network has become standard practice in computer vision. Self-supervision is a family of alternative pretraining methods that do not require any labeled data, since labels are “manufactured” through unlabeled data. Examples include inpainting [92], context prediction [26], and, the main focus of this chapter, automatic colorization [67, 68, 135].

supervised learning is developing models that work with weaker forms of supervision [6, 130].

This reduces the human burden only somewhat and pays a price in model performance.

Recently, *self-supervision* has emerged as a new flavor of unsupervised learning [25, 91, 124]. The key observation is that perhaps part of the benefit of labeled data is that it leads to using a discriminative loss. This type of loss may be better suited for representation learning than, for instance, a reconstruction or likelihood-based loss. Self-supervision is a way to use a discriminative loss on unlabeled data by partitioning each input sample in two, predicting the parts’ association. We focus on self-supervised colorization, where each image is split into its intensity and its color, as described in chapter 2.

Our main contributions to self-supervision are:

- The idea of using colorization for self-supervision with state-of-the-art results on VOC 2007 Classification and VOC 2012 Segmentation, among methods that do not use ImageNet labels.



- The first in-depth analysis of self-supervision via colorization. We study the impact of loss, network architecture and training details, showing that there are many important aspects that influence results.
- An empirical study of various formulations of ImageNet pretraining and how they compare to self-supervision.

## 3.2 Related Work

In our work on replacing classification-based pretraining for downstream supervised tasks, the first thing to consider is clever network initializations. Networks that are initialized to promote uniform scale of activations across layers, converge more easily and faster [35, 40]. The uniform scale however is only statistically predicted given broad data assumptions, so this idea can be taken one step further by looking at the activations of actual data and normalizing [79]. Using some training data to initialize weights blurs the line between initialization and unsupervised pretraining. For instance, using layer-wise  $k$ -means clustering [21, 61] should be considered unsupervised pretraining (see chapter 1), even though it may be a particularly fast one.

Unsupervised pretraining can be used to facilitate optimization or to expose the network to orders of magnitude larger unlabeled data. The former was once a popular motivation, but fell out of favor as it was made unnecessary by improved training techniques (*e.g.*, introduction of non-saturating activations [86], better initialization [35] and training algorithms [58, 94]). The second motivation of leveraging more data, which can also be realized as semi-supervised training, is an open problem with current best methods rarely used in competitive vision systems. Recent methods of self-supervised feature learning have seen several incarnations, broadly divided into methods that exploit temporal or spatial structure in natural visual data:

**Temporal.** There have been a wide variety of methods that use the correlation between

adjacent video frames as a learning signal. One way is to try to predict future frames, which is an analogous task to language modeling and often uses similar techniques based on RNNs and LSTMs [96, 112]. It is also possible to train an embedding where temporally close frames are considered similar (using either pairs [55, 56, 82] or triplets [124]). Another method that uses a triplet loss presents three frames and tries to predict if they are correctly ordered [81]. Pathak *et al.* [90] learn general-purpose representation by predicting saliency based on optical flow. Owens *et al.* [89], somewhat breaking from the temporal category, operate on a single video frame to predict a statistical summary of the audio from the entire clip. The first video-based self-supervision methods were based on Independent Component Analysis (ICA) [49, 121]. Recent follow-up work generalizes this to a nonlinear setting [50].

**Spatial.** Methods that operate on single-frame input typically use the spatial dimensions to divide samples for self-supervision. Given a pair of patches from an image, Doersch *et al.* [25] train representations by predicting which of eight possible spatial compositions the two patches have. Noroozi & Favaro [88] take this further and learns a representation by solving a 3-by-3 jigsaw puzzle. The task of inpainting (remove some pixels, then predict them) is utilized for representation learning by Pathak *et al.* [91]. There has also been work on adding encoders to Generative Adversarial Networks that can be used to learn representations [27, 29]. This is not what we typically regard as self-supervision, but it does similarly pose a supervised learning task (*real* vs. *synthetic*) on unlabeled data to drive representation learning.

**Colorization.** Lastly there is colorization [67, 68, 135, 136]. Broadly speaking, the two previous categories split input samples along a spatio-temporal line, either predicting one given the other or predicting the line itself. Automatic colorization departs from this as it asks to predict color over the same pixel as its center of input, without discarding any spatial information. We speculate that this may make it more suitable to tasks of similar nature, such as semantic segmentation; we demonstrate strong results on this benchmark.

Figure 3.2: **Feature re-use/re-purpose.** The left column visualizes top activations from the colorization network (same as in fig. 3.5). The right column visualizes the corresponding feature after the network has been fine-tuned for semantic segmentation. Features are either re-used as is (top), specialized (middle), or scrapped and replaced (bottom). See fig. 3.3 for a quantitative study.



### 3.3 Method

We discuss training separately in two parts, pretraining (when colorization is the target task) and fine-tuning (when colorization is a proxy task).

#### 3.3.1 Colorization as the Target Task

In this section we revisit training an automatic colorizer from chapter 2. However, we re-evaluate some of the design decisions that were made with the goal of producing aesthetic color images and instead consider their impact on learning representations.

**Loss.** We again consider both a regression loss for Lab color values [52, 67, 135], as well as a KL divergence loss for hue/chroma histograms [67]. We evaluate their ability to learn representations, disregarding their ability to do colorization. In our comparison, we make sure that the losses are scaled similarly, so that their effective learning rates are as close as possible (even better would be to use NormSGD described in section 4.5.3).

**Hypercolumn.** In chapter 2, hypercolumns were used with sparse samples to train our colorization network. Note that hypercolumns can be used for colorization pretraining, as

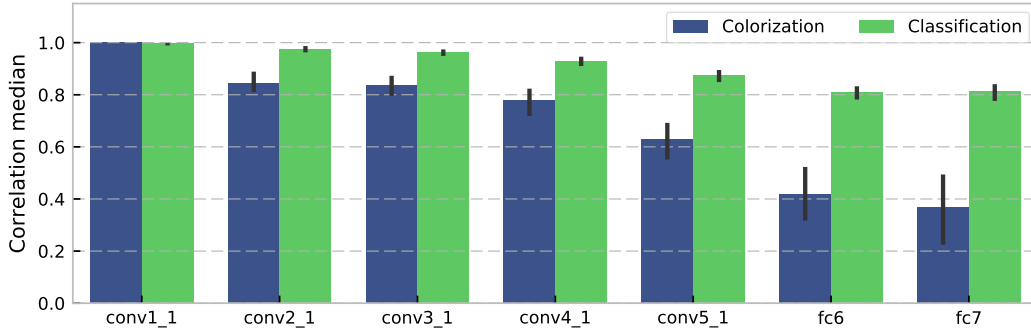


Figure 3.3: **Feature shift.** The correlation between feature activations for layers of VGG-16 before and after fine-tuning for semantic segmentation. The bar heights indicate median correlation and error bars indicate interquartile range. See section 3.2 for qualitative examples.

well as for segmentation as a downstream task. We know it is beneficial for downstream tasks [84] and evaluate its use for pretraining. Since we have reasons to believe that hypercolumn training may disrupt residual training, we do not train our ResNet colorizer from scratch with hypercolumns.

**Dataset.** We train on 3.7M *unlabeled* images by combining 1.3M from ImageNet [100] and 2.4M from Places205 [139]. The dataset contains some grayscale images and we do not make an effort to sort them out, since there is no way to tell a legitimately achromatic image from a desaturated one.

**Training.** All training is done with standard Stochastic Gradient Descent with momentum set to 0.9. The colorization network is initialized with Xavier initialization [35] and trained with batch normalization without re-biasing or re-scaling parameters [53]. Each time an image is processed, it is randomly mirrored and the image is randomly scaled such that the shortest side is between 352 and 600. Finally, a 352-by-352 patch is extracted and desaturated and then fed through the network. In our comparative studies, we train using a colorization loss for 3 epochs (spending 2 epochs on the initial learning rate). In our longer running experiments, we train for about 10 epochs. For our best ResNet model, we train significantly longer (35 epochs), although on smaller inputs (224-by-224); we found large

input sizes to be more important during downstream training. Code and trained models are made publicly available.<sup>1</sup>

### 3.3.2 *Colorization as a Proxy Task*

The downstream task is trained by initializing weights from the colorization-from-scratch network. Some key training considerations follow:

**Early stopping.** Training on a small sample size is prone to overfitting. We find that the most effective method of preventing this is careful cross validation of the learning rate schedule. Models that initialize differently (random, colorization, classification), need very different early stopping schedules. Finding a method that works well in all these settings was key to a fair and informative study. We split the training data 90/10 and only train on the 90%; the rest is used to monitor overfitting. Each time the 10% validation score (not surrogate loss) stops improving, the learning rate is dropped. After this is done twice, the training is concluded. For our most competitive experiments (table 3.1), we then re-train using 100% of the data with the cross-validated learning rate schedule fixed.

**Receptive field.** Previous work on semantic segmentation has shown the importance of large receptive fields [84, 133]. One way to accomplish this is by using dilated convolutions [127, 133]. However, this redefines the interpretation of filters and thus requires re-training. Instead, we add two additional blocks (2-by-2 max pooling of stride 2, 3-by-3 convolution with 1024 features) at the top of the network, each expanding the receptive field with 160 pixels per block (320 in total). In tables, we denote this change as “+FoV.” We train on large input images (448-by-448) in order to appreciate the enlarged receptive field. Using sparsely sampled targets (section 2.3.7) is particularly important for such large input size.

**Hypercolumn.** Note that using a hypercolumn when the downstream task is semantic

---

1. <https://github.com/gustavla/self-supervision>

segmentation is a separate design choice that does not need to be coupled with the use of hypercolumns during colorization pretraining. In either case, the post-hypercolumn parameter weights are never re-used. For ResNet, we use a subset of the full hypercolumn.<sup>2</sup>

**Batch normalization.** The models trained from scratch use parameter-free batch normalization. However, for downstream training, we absorb the mean and variance into the weights and biases and train without batch normalization (with the exception of ResNet, where in our experience it is still necessary). For networks that were not trained with batch normalization and are not well-balanced in scale across layers (*e.g.*, ImageNet-pretrained VGG-16), we re-balance the network so that each layer’s activation has unit variance (see section 2.3.6).

**Padding.** For our ImageNet pretraining experiments, we observe that going from a classification network to a fully convolutional network can introduce edge effects due to each layer’s zero padding. A problem not exhibited by the original VGG-16, leading us to suspect that it may be due to the introduction of batch normalization. For the newly trained networks, activations increase close to the edge, even though the receptive fields increasingly hang over the edge of the image, reducing the amount of semantic information. Correcting for this<sup>3</sup> makes activations well-behaved, which was important in order to appropriately visualize top activations. However, it does not offer a measurable improvement on downstream tasks, which means the network can correct for this during the fine-tuning stage.

**Color.** Since the domain of a colorization network is grayscale, our downstream experiments operate on grayscale input unless otherwise stated. When colorization is re-introduced, we convert the grayscale filters in `conv1_1` to RGB (replicate to all three channels, divide by three) and let them fine-tune on the downstream task.

---

2. ResNet-152 hypercolumn: `conv1`, `res2{a,b,c}`, `res3b{1,4,7}`, `res4b{5,10,15,20,25,30,35}`, `res5c`

3. We pad with the bias from the previous layer, instead of with zeros. This is an estimate of the expectation value, since we use a parameter-free batch normalization with zero mean, leaving only the bias.

Initialization	Architecture		Classification %mAP	Segmentation %mIU
ImageNet	VGG-16	(+FoV)	86.9	69.5
Random (ours)	AlexNet		46.2	23.5
Shortcut Autoencoder (ours)	AlexNet		53.3	28.7
Random [91]	AlexNet		53.3	19.8
$k$ -means [27, 61]	AlexNet		56.6	32.6
$k$ -means [61]	VGG-16		56.5	-
$k$ -means [61]	GoogLeNet		55.0	-
Pathak <i>et al.</i> [91]	AlexNet		56.5	29.7
Wang & Gupta [124]	AlexNet		58.7	-
Donahue <i>et al.</i> [27]	AlexNet		60.1	35.2
Doersch <i>et al.</i> [25, 27]	AlexNet		65.3	-
Zhang <i>et al.</i> (col) [135]	AlexNet		65.6	35.6
Zhang <i>et al.</i> (s-b) [136]	AlexNet		67.1	36.0
Noroozi & Favaro [88]	Modified AlexNet		68.6	-
Our method	AlexNet		65.9	38.4
	VGG-16	(+FoV)	<b>77.2</b>	56.0
	ResNet-152	(+FoV)	<b>77.3</b>	<b>60.0</b>
Our ensemble	3×ResNet-152	(+FoV)	<b>79.8</b>	<b>61.6</b>

Table 3.1: **VOC Comparison.** Comparison with other initialization and self-supervision methods on VOC 2007 Classification (test) and VOC 2012 Segmentation (val). First, we see how poorly our autoencoder really performed, with greedy layer-wise pretraining outperforming it and sometimes random initialization. However, it is worth mentioning that we perturb detection scores before calculating mAP, since otherwise even a trivial solution can incorrectly get around 53%; we cannot confirm that this ever happened to numbers that are not ours, however we do caution the reader that numbers in this range may not be reliable. Our baseline AlexNet results (38.4%) are also the most competitive among AlexNet models. The use of a hypercolumn instead of FCN is partly responsible: running Zhang *et al.*’s colorization model with a hypercolumn yields 36.4%, only a slight improvement over 35.6%. Switching to ResNet, adding a larger FoV, and training even longer yields a significantly higher result at 60.0% mIU. This number can be improved further with an ensemble of three colorization-pretrained networks. Note, the “+FoV” only affects the segmentation results. The modified AlexNet used by Noroozi & Favaro has the same number of parameters as AlexNet, with a spatial reduction of 2 moved from conv1 to pool5, increasing the size of the intermediate activations.

### 3.4 Results

We first present results on two established PASCAL VOC benchmarks, followed in section 3.5 by an investigation into different design choices and pretraining paradigms.

#### 3.4.1 PASCAL

**VOC 2012 Semantic Segmentation.** We train on the standard extended segmentation data (10,582 samples) and test on the validation set (1,449 samples). We sample random crops at the original scale. Our AlexNet results show that colorization is a front-runner among self-supervised methods at 38.4% mIU. Using our ResNet-152 model with extended field-of-view we achieve 60.0% mIU (see table 3.1), the highest reported results on this benchmark that do not use supervised pretraining. It is noticeable that this value is considerably higher than the AlexNet-based FCN [74] (48.0%) and even slightly higher than the VGG-16-based FCN (59.4%<sup>4</sup>), both methods train on ImageNet with class annotations.

**VOC 2007 Classification.** We train on *trainval* (5,011 samples) and test on *test* (4,952 samples). We use the same training procedure and loss with 10-crop testing as in [27]. Our AlexNet results at 65.9% mAP match state-of-the-art compared to other models. Our ResNet results improve this to 77.3% mAP (see table 3.1), setting a new state-of-the-art when no ImageNet labels are used.

These values can be improved further to 61.6% and 79.8%, respectively, by forming an ensemble with our best ResNet model (trained for 35 epochs) and two separately trained ResNet models (trained for 10 epochs each).



Pretraining Loss	Seg. (%mIU)
Regression	48.0
Histograms (no hypercolumn)	52.7
Histograms	52.9

Table 3.2: **Self-supervision loss.** (VGG-16) The choice of loss has a significant impact on downstream performance. However, pretraining with a hypercolumn does not seem to benefit learning. We evaluate this on VOC 2012 Segmentation (val) with a model that uses hypercolumns, regardless of whether or not it was used during pretraining.

Initialization	Grayscale	Color
Classification	66.5	69.5
Colorization	56.0	55.9

Table 3.3: **Color vs. grayscale input.** (VOC 2012 Segmentation, %mIU) Even though our classification-based model does 3 points better using color, re-introducing color yields no benefit.

## 3.5 Experiments

We present a wide range of experiments, highlighting important aspects of our competitive results. For these studies, in addition to VOC 2012 Semantic Segmentation, we also use two classification datasets that we constructed:

**ImNt-100k/ImNt-10k.** Similar to ImageNet classification with 1000 classes, except we have limited the training data to exactly 100 and 10 samples/class, respectively. In addition, all images are converted to grayscale. We test on ImageNet *val* with single center crops of size 224-by-224, making the results easy to compare with full ImageNet training. For our pretraining experiments in table 3.5, we also use these datasets to see how well they are able to substitute the entire ImageNet dataset for representation learning.

### 3.5.1 Loss

As seen in table 3.2, regressing on color in the Lab space yields a 5-point lower result (48.0%) than predicting histograms in hue/chroma (52.9%). This demonstrates that the choice of loss is of crucial importance to representation learning. This is a much larger difference than chapter 2 reports in colorization performance between the two methods (24.25 and 24.45 dB

---

4. Both of these values refer to VOC 2011 and evaluated on only 736 samples, which means the comparison is imprecise.

Architecture	Initialization	Epochs	Segmentation %mIU	+FoV	ImNt-100k %top-5	-10k
AlexNet	Random	-	23.5	24.6	39.1	6.7
AlexNet	Colorization	3	36.2	40.8	48.2	17.4
AlexNet	Colorization	10	38.4	42.5	49.7	18.8
VGG-16	Random	-	32.8	35.1	43.2	8.6
VGG-16	Colorization	3	50.7	52.9	59.0	23.3
VGG-16	Colorization	10	55.0	56.0	63.1	28.9
ResNet-152	Random	-	*9.9	*10.5	42.5	8.1
ResNet-152	Colorization	3	52.3	53.9	63.1	29.6
ResNet-152	Colorization	10	57.5	59.1	68.1	32.9
ResNet-152	Colorization	35	58.7	60.0	68.8	35.0

Table 3.4: **Architectures.** Evaluation of the impact of network architecture and pre-training time. The networks are evaluated on VOC 2012 semantic segmentation (val) and two small-sample ImageNet classification tasks. For our segmentation results, we also consider the effects of increasing the receptive field size (+FoV). Training residuals from scratch (marked with a \*) is possibly compromised by the hypercolumn, causing the low values.

PSNR / 0.318 and 0.299 RMSE). Histogram predictions are meant to address the problem of color uncertainty. However, the way they instantiate an image by using summary statistics from the histogram predictions, means this problem to some extent is re-introduced. Since we do not care about instantiating images, we do not suffer this penalty and thus see a much larger improvement using a loss based on histogram predictions. Our choice of predicting separate histograms in the hue/chroma space also yields an interesting finding in fig. 3.5, where we seem to have non-semantic filters that respond to input with high chromaticity as well as low chromaticity, clearly catering to the chroma prediction.

### 3.5.2 Network Architecture

The investigation into the impact of network architecture has been a neglected aspect of recent self-supervision work, which has focused only on the dated AlexNet. We present the first detailed study into the untapped potential of using more modern networks. These

Pretraining	$N$	Epochs	Seg. %mIU
None	-	-	35.1
C1000	1.3M	80	66.5
C1000	1.3M	20	62.0
C1000	100k	250	57.1
C1000	10k	250	44.4
E10	(1.17M) 1.3M	20	61.8
E50	(0.65M) 1.3M	20	59.4
H16	1.3M	20	60.0
H2	1.3M	20	46.1
R50	1.3M	20	57.3
		40	59.4
R16	1.3M	20	42.6
		40	53.5

Example: E30 (30% randomly re-assigned labels)

Example: H3 (3 hierarchical label buckets)

Example: R3 (3 random label buckets)

Table 3.5: **ImageNet pretraining variations.** We evaluate how useful various modifications of ImageNet are for VOC 2012 Segmentation (val-gray). We create new datasets either by reducing sample size or by reducing the label space. The former is done simply by reducing sample size or by introducing 10% (E10) or 50% (E50) label noise. The latter is done using hierarchical label buckets (H16 and H2) or random label buckets (R50 and R16). The model trained for 80 epochs is the publicly available VGG-16 (trained for 76 epochs) that we fine-tuned for grayscale for 4 epochs. The rest of the models were trained from scratch on grayscale images.

results are presented in table 3.4.

It is not entirely obvious that an increase in model complexity will pay off, since our focus is small-sample datasets and a smaller network may offer a regularizing effect. Take ImNt-100k, where AlexNet, VGG-16, and ResNet-152 all perform similarly when trained from scratch (39.1%, 43.2%, 42.5%). However, the percentage point improvement when utilizing 10 epochs of colorization pretraining follows a clear trend (+10.6, +19.9, +25.6). This shows that self-supervision allows us to benefit from higher model complexity even in small-sample regimes. Compare this with  $k$ -means initialization [61], which does not show any improvements when increasing model complexity (table 3.1).

Training ResNet from scratch for semantic segmentation is an outlier value in the table. This is the only experiment that trains a residual network from scratch together with a hypercolumn; this could be a disruptive combination as the low numbers suggest.

### 3.5.3 *ImageNet Pretraining*

We relate self-supervised pretraining to ImageNet pretraining by revisiting and reconsidering various aspects of this paradigm (see table 3.5). First of all, we investigate the importance of 1000 classes (C1000). To do this, we join ImageNet classes together based on their place in the WordNet hierarchy, creating two new datasets with 16 classes (H16) and only two classes (H2). We show that H16 performs only slightly short of C1000 on a downstream task with 21 classes, while H2 is significantly worse. If we compare this to our colorization pretraining, it is much better than H2 and only slightly worse than H16.

Next, we study the impact of sample size, using the subsets ImNt-100k and ImNt-10k described in section 3.5. ImNt-100k does similarly well as self-supervised colorization (57.1% vs. 56.0% for VGG-16), suggesting that our method has roughly replaced 0.1M labeled samples with 3.7M unlabeled samples. Reducing samples to 10 per class sees a bigger drop in downstream results. This result is similar to H2, which is somewhat surprising: collapsing

the label space to a binary prediction is roughly as bad as using 1/100th of the training data. Recalling the improvements going from regression to histogram prediction for colorization, the richness of the label space seems critical for representation learning.

We take the 1000 ImageNet classes and randomly place them in 50 (R50) or 16 (R16) buckets that we dub our new labels. This means that we are training a highly complex decision boundary that may dictate that a golden retriever and a minibus belong to the same label, but a golden retriever and a border collie do not. We consider this analogous to self-supervised colorization, since the supervisory signal similarly considers a red car arbitrarily more similar to a red postbox than to a blue car. Not surprisingly, our contrived dataset R50 results in a 5-point drop on our downstream task, and R16 even more so with a 20-point drop. However, we noticed that the training loss was still actively decreasing after 20 epochs. Training instead for 40 epochs showed an improvement by about 2 points for R50, while 11 points for R16. In other words, complex classes can provide useful supervision for representation learning, but training may take longer. This is consistent with our impression of self-supervised colorization; although it converges slowly, it keeps improving its feature generality with more training.

Finally, we test the impact of label noise. When 10% of the training images are re-assigned a random label (E10), it has little impact on downstream performance. Increasing the label noise to 50% (E50) incurs a 2.6-point penalty, but it is still able to learn a competitive representation.

### *3.5.4 Training Time and Learning Rate*

We show in fig. 3.4 that it is crucial for good performance on downstream tasks to reduce learning rate during pretraining. This result was not obvious to us, since it is possible that the late stage of training with low learning rate is too task-specific and will not benefit feature generality.

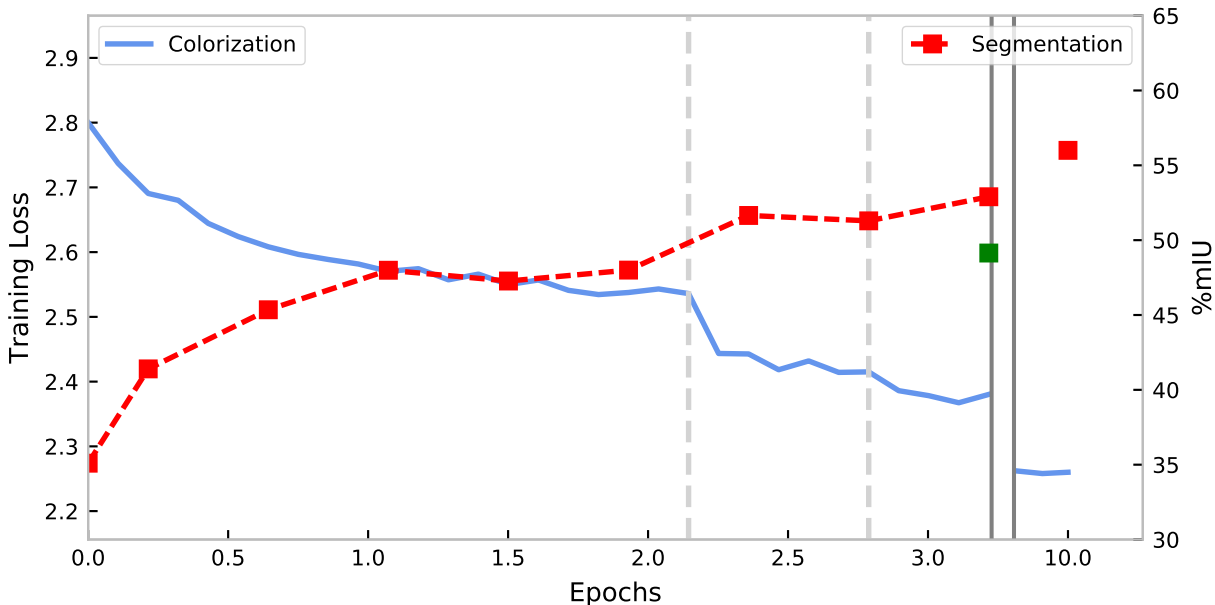


Figure 3.4: **Learning rate.** The blue line shows colorization training loss and the vertical dashed lines are scheduled learning rate drops. The red squares are results on a downstream task (VOC 2012 Segmentation) initialized by the corresponding snapshot of the colorization network. Some key observations: We quickly get value for our money, with a 6-point improvement over random initialization with only 0.2 epochs of training. Furthermore, improvements on the downstream task do not quickly saturate, with results improving further when trained 10 epochs in total. Dropping the learning rate on the pretraining task helps the downstream task, with a similarly abrupt improvement as with the training loss around 2 epochs. Training the full 3 epochs without ever dropping the learning rate results in 49.1% (green square) compared to 52.9% mIU.

In addition, we show the importance of training time by demonstrating that training for three times as long (10 epochs, 37M samples) improves results from 52.9% to 56.0% mIU on VOC 2012 Segmentation. Our ResNet-152 model (60.0% mIU) trained for 4 months on a single GPU.

### 3.5.5 Latent Representation

Good results on secondary tasks only give evidence that our self-supervised network has the potential to be shaped into a useful representation. We investigate if the representation

Fine-tuned layers (VGG-16)		Random	Colorization	Classification
$\emptyset$	□□□□□□	3.6	36.5	60.8
fc6, fc7	□□□□■	-	42.6	63.1
conv4_1..fc7	□□■	-	53.6	64.2
conv1_1..fc7	■	35.1	56.0	66.5

Table 3.6: **End-to-end fine-tuning.** (VOC 2012 Segmentation, %mIU) Classification-based pretraining needs less fine-tuning than our colorization-based method. This is consistent with our findings that our network experiences a higher level of feature shift (fig. 3.3). We also include results for a randomly initialized network, which does not work at all without fine-tuning (3.6%). This is to show that it is not simply by virtue of the hypercolumn that we are able to do reasonably well (36.5%) without any fine-tuning of the base network.

learned through colorization is immediately useful or only holds a latent representation. If the latter, how is our representation different from a good initialization scheme?

First, we visualize features to get a sense of how the colorization network has organized the input into features. We posit that we will find features predictive of color, since we know that the colorization network is able to predict color with good accuracy. In fig. 3.5, we visualize top activations from the network’s most high-level layer, and indeed we find color-specific features. However, we also find semantic features that group high-level objects with great intra-class variation (color, lighting, pose, etc.). This is notable, since no labeled data was used to train the network. The notion of objects has emerged purely through their common color and visual attributes (compare with [138]). Object-specific features should have high task generality and be useful for downstream tasks. Features that are specific to both object and color (bottom-right quadrant in fig. 3.5) can be divided into two categories: The first is when the object generally has a unimodal color distribution (e.g. red bricks, brown wood); the second is when the network has learned a color sub-category of an object with multimodal color distribution (e.g. white clothing, yellow vehicle). These should all have high task generality, since it is easy for a task-specific layer to consolidate several color sub-categories into color-invariant notions of objects.

So how much do the features change when fine-tuned? We visualize top activations before

and after in section 3.2 and show in fig. 3.3 that the colorization features change much more than supervised features. Some features are completely re-purposed, many are only pivoted, and others remain more or less the same. These results are consistent with the four quadrants in fig. 3.5, that show that some features are specific to colorization, while others seem to have general purpose.

Next, we look at how much fine-tuning is required for the downstream task. Table 3.6 tells us that even though fine-tuning is more important than for supervised pretraining (consistent with the correlation results in fig. 3.3), it is able to perform the task with the colorization features alone similarly well as randomly initializing the network and training it end-to-end from scratch.

Somewhat poor results without fine-tuning and a lower percentage of feature re-use supports the notion that the colorization network in part holds *latent* features. However, the visualized features and the strong results overall suggest that we have learned something much more powerful than a good initialization scheme.

### 3.5.6 Color

We show in table 3.3 that re-introducing color yields no benefit (consistent with the findings of Zhang *et al.* [135]). However, concurrent work [136] presents a better method of leveraging the color channels by separately training a network for the “opposite” task (predicting intensity from color). The two separate networks are combined for downstream use.

## 3.6 Conclusion

Using the high-level semantic requirements of automatic colorization, we have proposed it as a drop-in replacement for ImageNet pretraining. This method presents state-of-the-art results on semantic segmentation and small-sample classification that do not use ImageNet labels. Our investigation is focused, but not limited in purpose, to automatic colorization.



The investigation into the benefits of network architecture, training scheduling, loss, etc., may benefit self-supervision in general. A detailed investigation into self-supervised colorization shows the importance of the loss, network architecture and training details in achieving competitive results. We conjecture that many of these findings are relevant beyond colorization and will benefit the broader self-supervision effort. We also draw parallels between this and ImageNet pretraining, by exploring how robust labeled data is for representation learning. This study shows that self-supervision is on par with several methods using annotated data.

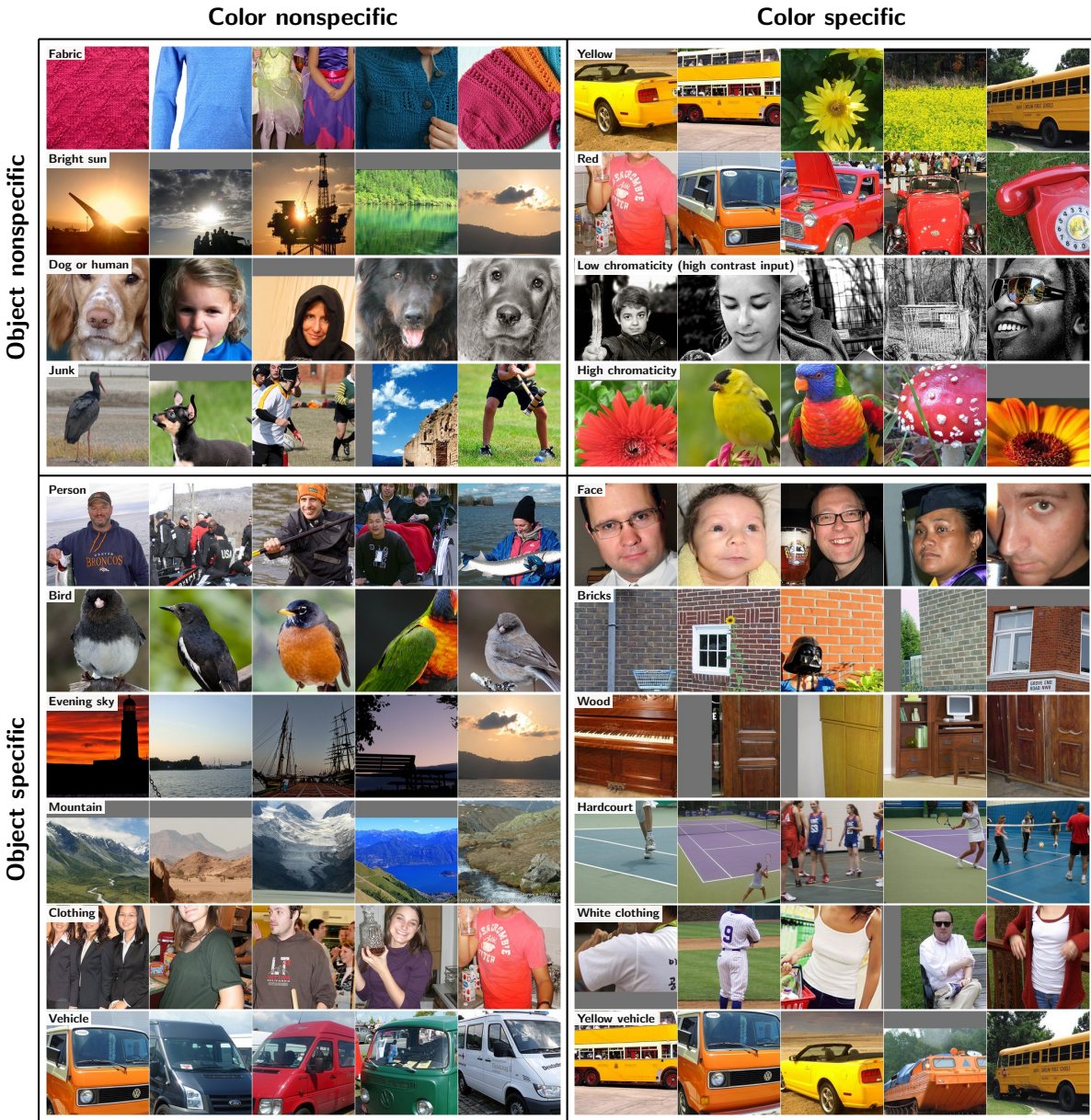


Figure 3.5: **Feature visualization.** Patches around activations from held-out images are visualized for a select number of `fc7` features (VGG-16). Even though the network takes only grayscale input, we visualize each patch in its original color for the benefit of the reader. As a result, if all the activations are consistent in color (right column), the feature is predictive of color. Similarly, if a feature is semantically coherent (bottom row), it means the feature is predictive of an object class. The names of each feature are manually set based on the top activations.

## CHAPTER 4

### MULTI-PROXY REPRESENTATION LEARNING

In this chapter we explore the possibility of combining several self-supervised proxy tasks to evaluate if it can lead to more robust and general-purpose representations.

#### 4.1 Introduction

Colorization can act as a proxy task for visual representation learning, as demonstrated in chapter 3. However, we have also seen that the representation that is learned is in many ways specialized for colorization. It is also unable to successfully use color as a prediction input in the final model. We note that there are other methods of self-supervision that achieve competitive results, such as jigsaw solving [88] and optical flow-based segmentation [90]. Other methods have their own idiosyncrasies. For instance, jigsaw solvers trained on color images learn to respond to color only through green-purple edges (see fig. 4.6). We explore the possibility of combining multiple self-supervision methods, in order to average out these idiosyncrasies and learn a more versatile and robust representation. As new ideas for self-supervised learning signals are developed, they may not beat existing methods alone. However, it is still possible that they collectively add to the improvement of self-supervised representation learning, if there is a method of combining multiple self-supervision proxy tasks. We evaluate several techniques, grouped into what we call *offline* and *online* model aggregation methods:

**Offline.** An offline method combines multiple already trained models into one and does not revisit the original task loss. The main benefit of such system is that the research and engineering effort is distributed. Taking the research community as an example, a group of researchers, using their own favorite deep learning software, can develop a new self-supervision method and put the model online. This could then be downloaded by separate

researchers and used to build stronger self-supervised representations. We will consider the offline methods model distillation (section 4.3) and model concatenation (section 4.4.1).

**Online.** Online methods involve actively training several methods together. Unlike offline methods, they do not have the benefits of distributed effort. However, the potential benefits of being able to train the network with all methods actively involved may warrant this sacrifice. It does have the engineering downside that each method has to be re-implemented into a single framework. We will consider online methods where base network weights from different proxy tasks are disjoint (section 4.4.2) or shared (section 4.5).

We show that offline and online methods both show promise on test benchmarks based on supervised pretraining where the level of diversity between tasks is controlled. However, this does not yet translate to the self-supervised setting, suggesting that the level of diversity between representations is perhaps not as high as we initially conjectured, or simply not high enough for current methods to appreciate.

Contributions in this chapter include:

- A new model distillation loss that works on both probabilistic and non-probabilistic activations, with much less need to tune the temperature parameter.
- We formulate *task-agnostic model distillation* and propose an effective method to learn from multiple teachers that were not trained for a single task.
- We diagnose the issue of imbalanced gradient norms when combining multiple tasks and propose an easy but effective fix using global gradient normalization.
- We implement three self-supervision methods into a single framework and evaluate joint training. In addition to colorization and jigsaw solving, we propose a new simple self-supervision method based on predicting optical flow in videos.

## 4.2 Related Work

The two primary areas that we relate our work to is model distillation (offline method) and multi-task learning (online method).

**Model Distillation.** Transferring the information of a large network (often an ensemble of several networks) into a smaller one is called *model compression*, *model distillation*, or *student-teacher learning*. The process involves passing samples through both the teacher (the large network) and the student (the small network), updating only the student so that its top-level activations closely match the teacher’s activation as specified by a distance or divergence loss. The task was introduced by Buciluă *et al.* [11] in 2006. Their approach involved building a large ensemble of networks and then using the hard predictions of the ensemble to label a large sample of synthetic data. This new dataset was subsequently used to train a smaller network.

The concept of model compression attracted renewed attention a decade later. This time, neural networks had become ubiquitous and the ambition grew to run them on low-power devices, such as mobile phones or hearing aids. Ba and Caruana published a follow-up work in 2014 [4] where they suggest, as a replacement for hard targets, using squared  $L_2$  or softmax and KL divergence to penalize discrepancies between the student and the teacher. Their main conclusion is that it is possible to take a multi-layer neural network and compress it into a single layer. However, Urban *et al.* [119] revisit this claim and demonstrate evidence to refute it, especially in the context of convolutional neural networks. This does not invalidate the concept of model compression however, since it is still possible to make student networks significantly smaller without going all the way to single-layer networks.

In the same wave of renewed attention, Hinton *et al.* [43] promoted the work of Caruana and colleagues in a NIPS workshop contribution. In addition, they contributed the notion of temperature, a loss parameter that allows gradually trading off between hard target predictions and squared  $L_2$ .

More broadly, it has also become a trend to approximate non-feedforward models into neural networks, which can be seen as a form of model compression. The source is typically a costly iterative algorithm and the purpose is to make it faster and potentially generalize better. Approximating a hand-coded algorithm by a neural network is also a way to make it more versatile, allowing fine-tuning on downstream tasks. To mention a few, Liang *et al.* [72] initially trains a highly structured Conditional Random Field (CRF) with costly inference. To make it cheaper, they subsequently train a regression model on samples labeled by the CRF. Pathak *et al.* [90] train a CNN to predict the results of an unsupervised segmentation algorithm based on optical flow and a graph-based algorithm.

**Multi-Task Learning.** The method for our primary online method comes from Caruana’s doctoral thesis “Multitask Learning,” [12] where he trains multiple tasks at once using neural networks with shared weights. Much follow-up work under this name has focused on single-layer neural networks or kernel methods [3, 14, 31, 64]. There is recent work using CNNs focusing on optimizing the performance on all tasks together, for instance by making the exact branching point more fluid [80] or by using tensor factorization to separate general and task-specific features [131]. This is different from our goal, since we do not care about the proxy task performance (only insofar as it is correlated with representation performance) and we prefer to keep the base network as standard as possible. Our approach follows that of Caruana’s original and the more recent UberNet [60]: training all tasks with the same base network and a minimal number of task-specific layers for each task. UberNet uses a single network to train a wide range of supervised vision tasks, both high-level (*e.g.*, semantic segmentation), and more low-level (*e.g.*, boundary detection).

### 4.3 Model Distillation

Student-teacher learning is the act of distilling the knowledge of a teacher network into a, typically smaller, student network. A common choice of teacher is an ensemble of separately

trained networks:

$$f_{\text{teacher}}(x) = \frac{1}{M} \sum_m f_m(x)$$

An ensemble often leads to better prediction results than each individual model alone. The improvement depends on the correlation of errors between models, with lower correlation resulting in larger gains [118]. Inference in the ensemble, however, is  $M$  times as expensive as a single network. The ambition of model distillation is to compress it back down to a single network with fast inference, while preserving, to the extent possible, the predictive benefits of the ensemble.

A popular loss for distillation is KL divergence after a temperature-adjusted softmax

$$L(x) = T^2 D_{\text{KL}}(\text{softmax}(\mathbf{y}/T) \parallel \text{softmax}(\mathbf{z}/T)), \quad (4.1)$$

where  $\mathbf{y} = f_{\text{teacher}}(x)$  and  $\mathbf{z} = f_{\text{student}}(x)$ . The temperature,  $T$ , allows control over the relative importance between high scoring and low scoring classes. In the temperature limits two special cases merge: squared  $L_2$  at  $T \rightarrow \infty$  (low and high scores are equally important), and hard predictions at  $T \rightarrow 0$  (only highest scoring class matters). At test time, we often care only about hard predictions, which is arguably why this is the only information we need to preserve from the teacher. However, a squared  $L_2$  has shown to provide better generalization properties for out-of-sample predictions, since it conveys a more nuanced view of the teacher. Temperature introduces control over this trade-off.

#### 4.3.1 Task-Agnostic Distillation

If we train several models on different tasks, it is not possible to average scores into an ensemble. Is it still possible to do student-teacher type distillation? We call this *task-agnostic* student-teacher learning and we will demonstrate that it is possible and can yield positive results. The solution that we propose is to move the target layer from the task

layer to the top non-task layer (*e.g.*, `fc7` in VGG-16). Two issues need to be addressed: (1) We need a distillation loss that is appropriate and works well on non-probabilistic feature activations, and (2) we need a method of combining multiple networks into a single teacher signal that is compatible with the student network. The first problem is addressed by introducing a new distillation loss in section 4.3.2 and the second by sampling subsets of features in section 4.3.4.

### 4.3.2 New Distillation Loss

We propose a new distillation loss that can be used for both task-driven (distillation at task layer) and task-agnostic (distillation at top intermediate layer) student-teacher learning. It closely resembles temperature-adjusted KL divergence, with a few important differences. In section 4.3.3, we further show that this is a special case of the Alpha-Beta (AB) divergence and demonstrate how it can be configured to achieve a variety of properties.

The new distillation loss is defined as follows:

$$L_{\text{new}}(x; T) = \frac{T^2}{C} D_{\text{KL}}(\exp(\hat{\mathbf{y}}/T) \| \exp(\hat{\mathbf{z}}/T)) \quad (4.2)$$

The normalized exponential (softmax) in (4.1) has been changed to an unnormalized exponential. Division by the number of features,  $C$ , makes the scale of the loss invariant to  $C$  and the loss easily interpretable as the average loss per feature. Using unnormalized exponentials produces unnormalized measures, prompting the use of the *generalized* KL divergence [63]:

$$D_{\text{KL}}(\mathbf{p} \| \mathbf{q}) = \sum_i \left[ p_i \log \frac{p_i}{q_i} - p_i + q_i \right] \quad \mathbf{p}, \mathbf{q} \in \mathbb{R}_+^C \quad (4.3)$$

The features are instead pre-normalized using statistics of the teacher signal:

$$\hat{\mathbf{y}} = \left( \frac{y_1}{s_1}, \dots, \frac{y_C}{s_C} \right), \quad \hat{\mathbf{z}} = \left( \frac{z_1}{s_1}, \dots, \frac{z_C}{s_C} \right), \quad s_c = \sqrt{\hat{\mathbb{E}}[y_c^2]} \text{ for all } c \quad (4.4)$$



The normalization has two purposes. First, since temperature effectively adjusts feature scale, this is a way to establish a universal temperature scale that does not change depending on the natural scale of the network. This can optionally be done with a single teacher statistic used for all features,  $s = \sqrt{\hat{\mathbb{E}}[y^2]}$ . However, if the teacher vector is a concatenation of several networks with different natural scale, individual statistics are preferred. We can also optionally remove the normalization from  $\mathbf{z}$ , which would cause the student to learn well-normalized top activations, without trying to mimic the teacher precisely.

A side-by-side comparison of the change in gradients show how similar the updated loss is ( $L_{\text{old}}$  is  $L$  from (4.1)):

$$\frac{\partial L_{\text{old}}}{\partial z_i} = T \left( \frac{e^{z_i/T}}{\sum_j e^{z_j/T}} - \frac{e^{y_i/T}}{\sum_j e^{y_j/T}} \right) \quad \frac{\partial L_{\text{new}}}{\partial z_i} = T \left( \frac{e^{\hat{z}_i/T}}{C} - \frac{e^{\hat{y}_i/T}}{C} \right)$$

Apart from feature pre-normalization, the only difference is that the sums over all exponentials have been replaced by  $C$ . We note that both normalization sums in the old loss approaches  $C$  as  $T \rightarrow \infty$ . Removing the cross-terms in the denominator means re-visiting the intuition for temperature. Instead of affecting the entropy of the activation vector, it simply changes the shape of the loss that operates on each activation separately. This makes it easy to visualize and promotes better intuition.

The old loss was shift invariant for both student and teacher activations. This means that if we add a constant to  $\mathbf{y}$ , the loss does not change. This is independently true for  $\mathbf{z}$ , which means that the loss does not drive the student and the teacher to have the same mean over activations. The new loss instead forces this, which is an innocuous change for task-driven distillation that is easily accommodated by biases in the student. For task-agnostic distillation however, the change is important since when the network is finally used for a downstream task, the top activations are passed through a ReLU before a task prediction layer. The ReLU is not shift invariant, so it is important that the student activations have the same mean as the teacher activations.

### 4.3.3 AB Divergence

The AB divergence is borrowed from work in non-negative matrix factorization [20]. It takes unnormalized measures and has two parameters,  $(\alpha, \beta) \in \mathbb{R}^2$ , that control the properties of the divergence. The divergence is defined as a sum over the elements of the measures, without cross-terms, as

$$D_{\text{AB}}^{(\alpha, \beta)}(\mathbf{p} \parallel \mathbf{q}) = \sum_i d_{\text{AB}}^{(\alpha, \beta)}(p_i, q_i), \quad (4.5)$$

where

$$d_{\text{AB}}^{(\alpha, \beta)}(p, q) = \begin{cases} -\frac{1}{\alpha\beta} \left( p^\alpha q^\beta - \frac{\alpha}{\alpha+\beta} p^{\alpha+\beta} - \frac{\beta}{\alpha+\beta} q^{\alpha+\beta} \right) & \alpha, \beta, \alpha + \beta \neq 0 \\ \frac{1}{\alpha^2} \left( p^\alpha \log \frac{p^\alpha}{q^\alpha} - p^\alpha + q^\alpha \right) & \alpha \neq 0, \beta = 0 \\ \frac{1}{\alpha^2} \left( \log \frac{q^\alpha}{p^\alpha} + \left( \frac{q^\alpha}{p^\alpha} \right)^{-1} - 1 \right) & \alpha = -\beta \neq 0 \\ \frac{1}{\beta^2} \left( q^\beta \log \frac{q^\beta}{p^\beta} - q^\beta + p^\beta \right) & \alpha = 0, \beta \neq 0 \\ \frac{1}{2} (\log p - \log q)^2 & \alpha, \beta = 0. \end{cases} \quad (4.6)$$

For readers familiar with the Rényi divergence (also known as the Alpha divergence) [98], the AB divergence can be interpreted as extending it with the notion of temperature. The sum  $\alpha + \beta$  of the AB divergence is the inverse temperature and controls the importance of large activations.

The new loss presented in (4.2) is a special case where  $\beta = 0$ :

$$L_{\text{new}}(x; T) = \frac{1}{C} D_{\text{AB}}^{(1/T, 0)}(\exp(\hat{\mathbf{y}}) \parallel \exp(\hat{\mathbf{z}})) \quad (4.7)$$

It even provides the  $T^2$  scale correction from (4.1) and (4.2). By adjusting both  $\alpha$  and  $\beta$  we can explore a variety of divergences. First of all, at  $(0, 0)$ , coupled with the exponential activation function, we get the squared  $L_2$  loss. For the traditional loss (4.1), this was only true in the limit  $T \rightarrow \infty$  and when both feature vectors were assumed to have zero mean.

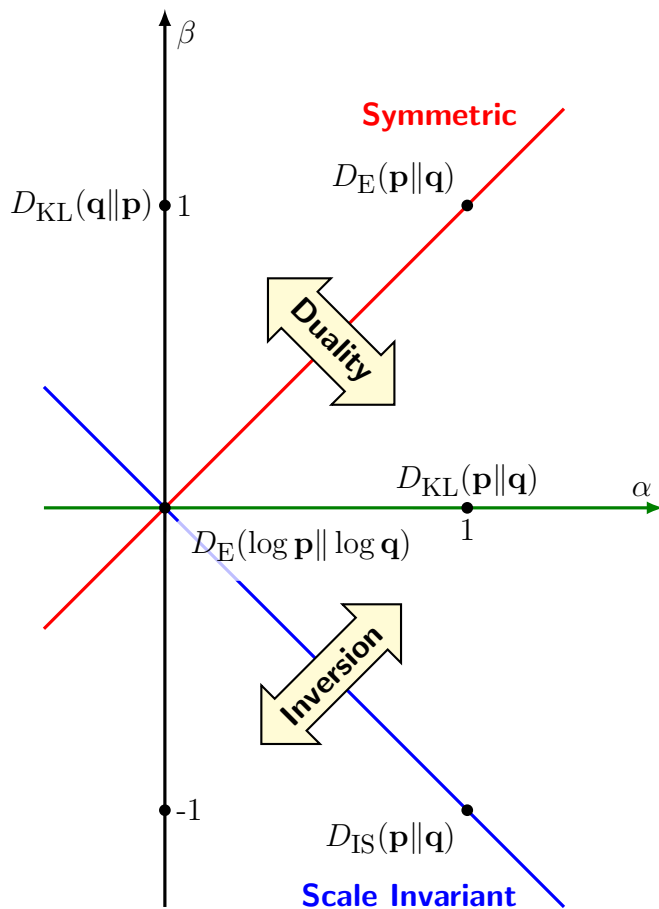


Figure 4.1: **AB divergence.** Adjusting  $(\alpha, \beta)$  changes the properties of the divergence. The red line  $\alpha = \beta$  describes symmetric divergences, where  $D(\mathbf{p} \parallel \mathbf{q}) = D(\mathbf{q} \parallel \mathbf{p})$ . Reflecting a point around this duality line causes arguments to be swapped (*e.g.*, the reverse KL divergence is found at  $(0, 1)$ ). The blue line  $\alpha = -\beta$  describes scale invariant divergences,  $D(\mathbf{p} \parallel \mathbf{q}) = D(c\mathbf{p} \parallel c\mathbf{q})$ , which results in shift invariance in the feature space. Two points reflected around this inversion line describes two scale variant divergences: one that penalizes larger values more and one that penalizes smaller values more. This figure is a replica of one in the original AB divergence paper [20].

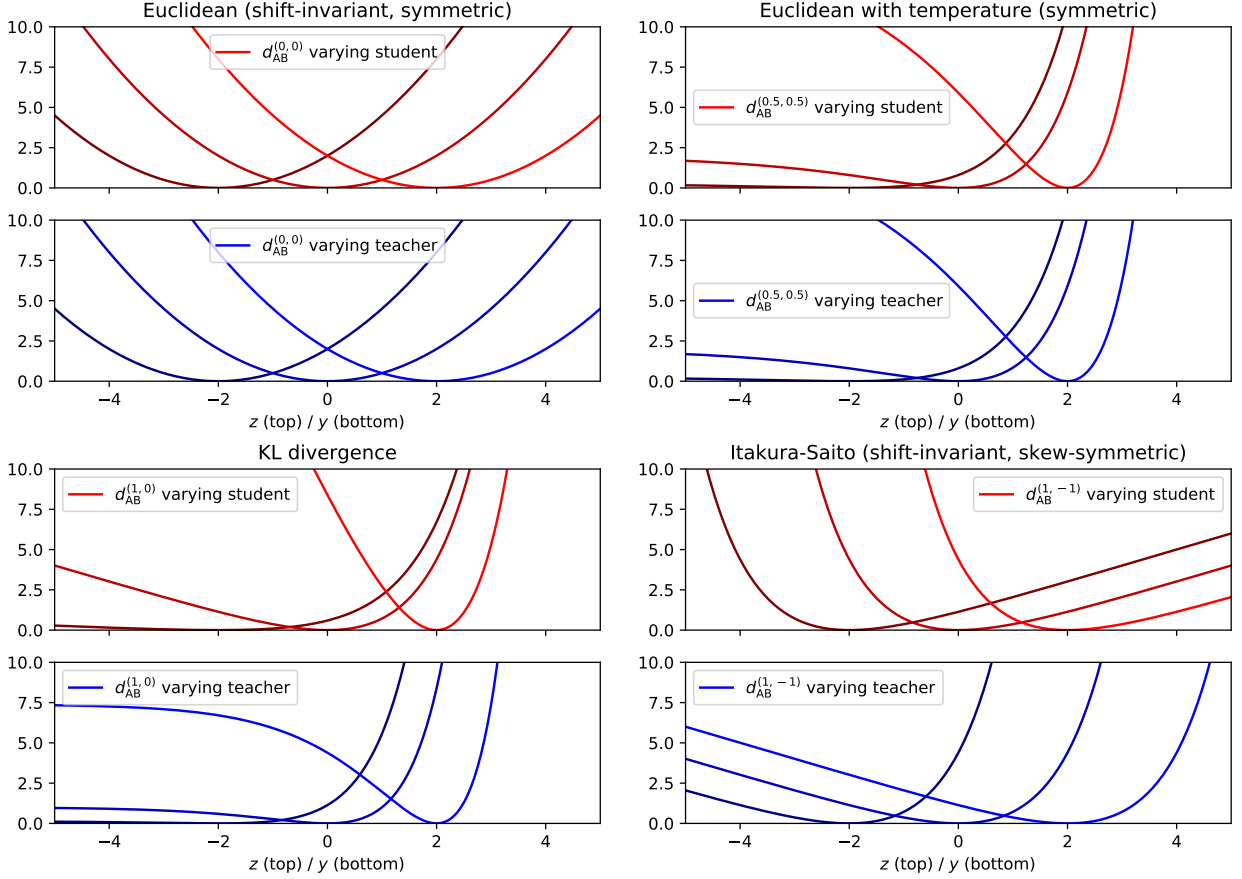


Figure 4.2: **Shape of AB divergence.** Four AB divergences coupled with exponential activations are visualized in two plots each. The top (red) shows three anchor points of the teacher score (-2, 0, 2) while varying the student score. The bottom (blue) shows three anchor points of the student score (-2, 0, 2) while varying the teacher score. The anchor points are not labeled, but are easy to identify since they reach exactly 0 only at the anchor value. The divergence is symmetric if the red and blue plots are the same ( $D(p||q) = D(q||p)$ ) and shift-invariant if the plots for the three anchor points have the same shape. These four divergences are evaluated quantitatively in fig. 4.5.

Furthermore, by moving along the  $\alpha = \beta$  line, we get a symmetric divergence with the notion of temperature. If we instead move along the  $\alpha = -\beta$  line, we preserve shift invariance in  $\mathbf{y}$  and  $\mathbf{z}$ , while changing the balance between how much we penalize over-estimation versus under-estimation. Since the divergence has no cross terms and  $d_{AB}$  operates on scalars, it makes it easy to visualize the loss. See fig. 4.1 for a schematic of the parameter space and fig. 4.2 for concrete examples visualized.

#### 4.3.4 Feature Compatibility

Now that we have a loss that works well on intermediate activations, we move on to the second problem of task-agnostic distillation: compatibility of the feature vector between the student and the teacher. For instance, consider a teacher that is the concatenation of  $F$  top activations of  $M$  identical architectures trained on different tasks. Such teacher will now have  $MF$  features and thus not compatible with the student, which has only  $F$ . We consider several solutions to address this.

**Adapt student.** A simple way is to allow the student to have the same number of features as the teacher at the necessary layer. Since this only affects one layer, it is still possible to make the student smaller in terms of parameters. However, this skews the network more and more as the teacher grows (*e.g.*, as  $M$  increases), and it makes fair comparisons between methods harder. For these reasons, we will restrict ourselves to methods that can abide by the student architecture without changing it.

**Auxiliary layer.** One way of addressing this is to pass the  $F$  features of the student through a fully connected layer with  $MF$  output activations. The distillation loss is then applied on top of this additional layer, where both student and teacher have  $MF$  features. The extra layer is discarded after distillation training, so it would be unfortunate if it has captured important high-level semantics. Note that a ReLU is applied before the fully connected layer, since we want the top activations of the student to be able to pass through

a ReLU with meaningful results.

**Feature subset.** Another approach, that admittedly seems less powerful, is to take a random subset of  $F$  from the teacher’s  $MF$  features. This gives better results than any auxiliary layer approach that we tried (see table 4.4). Although not experimentally tested here, a slight improvement might be offered by first training the student with a wide layer (equivalent to “adapt student”) and then subsetting the features to reduce it to the target network. This would allow all features of the teacher vector to drive representation learning for all previous layers of the network.

#### 4.3.5 *Data Augmentation, Dropout, and Warm Start*

Even with the distillation loss and network compatibility addressed, it can still be a challenge to perform a successful model distillation. Since training data for distillation does not need annotations, this can and should be drawn from a large data source. However, it is important to be mindful of the data distribution. For instance, a preliminary investigation showed that ImageNet downsampled to 32-by-32 was not a good source of unlabeled distillation samples for a model originally and eventually operating on CIFAR-100. However, using data augmentation on CIFAR-100 during the distillation phase is helpful.

When distillation data is limited, we found that the best source of regularization is dropout in the student network (see section 4.6.1). Adding dropout in the teacher has a limited effect on results, so we do not do it for any of the experiments.

Finally, in the case where the teacher is  $M$  networks of the same architecture as the student, it may help to warm start the student with one of the teacher networks. We will see that in our experiments in table 4.4 this offers only a minor improvement, which is a good sign that our distillation training trains well on its own.

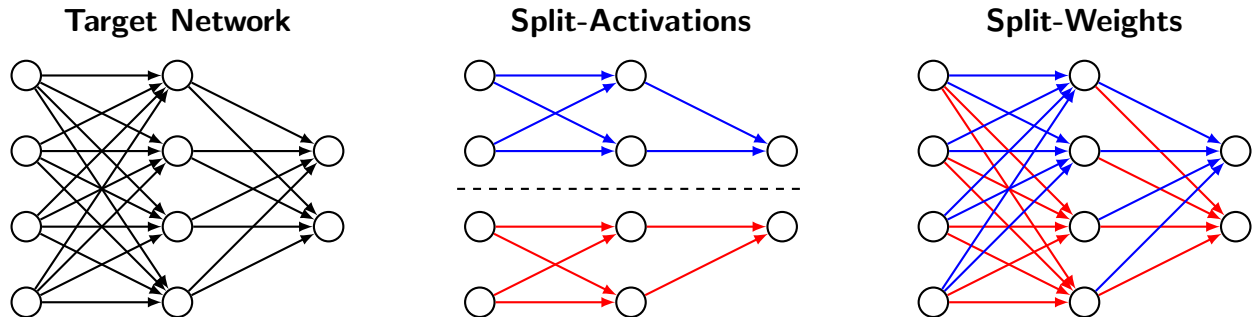


Figure 4.3: **Schematic of disjoint weights training.** The target network represents the base neural network architecture. The split-activations method (section 4.4.1) concatenates separately trained networks that have been made thinner in order to conform to the target network. In this example there are two tasks, visualized as red and blue, respectively. The thinness of the two networks means we lose the weights that would ordinarily cross the dashed line (cross-weights). The split-weights method (section 4.4.2) is similar to split-activations, except it assigns those cross-weights to the task associated with the destination node.

## 4.4 Disjoint Weights Training

We move on to other aggregation methods, namely two where each parameter in the final network is associated with a single task. This prevents multiple tasks from operating on the same parameter, which is associated with an issue of uneven gradients described in section 4.5.1.

### 4.4.1 Split-Activations

The first method we consider is performed offline and simply concatenates multiple separately trained networks. This technique has been successfully applied to complementary self-supervision tasks, where it is called the *split-brain autoencoder* [136].

For the final concatenated network to resemble our target student, each task network must be thinner than the original by a factor  $1/M$  (see fig. 4.3). This becomes a subset of the student network, since cross-connections between task columns are removed. This does not scale well in  $M$ , since the number of parameters in the combined network will change

by a factor  $1/M$ . Of course, we could widen the networks accordingly to preserve the total number of parameters. This is an avenue that makes fair network comparisons harder, so we do not explore it here. Note, in our implementation during downstream training, once the network has been combined, we allow cross-weights to update freely after a minimally disruptive random initialization.

#### 4.4.2 *Split-Weights*

Inspired by split-activations, we propose split-weights. Instead of partitioning the activations at each layer into separate columns, we partition the weights. This means that, similar to split-activations, no weight in the base network receives gradients from more than one task. The cross-weights that were previously discarded are now assigned to the column that they go into. This means that a task column can look and use activations from other tasks and no weights are left untrained (see fig. 4.3).

This offers an improvement over split-activations, even at  $M = 2$ . The gap widens as  $M$  is increased and split-weights loses more and more parameters to cross-terms. The downside is that it no longer enjoys the benefits of an offline method and needs to be trained jointly.

### 4.5 Shared Weights Training

Finally, we discuss the method proposed by Caruana [12], to add the losses and use weight sharing for the base network. We can think of this as keeping separate copies of a base network, each with a task-specific appendage. A forward-backward pass is performed on each with their respective task loss. The gradients are finally aggregated and applied to all networks by element-wise summation. Using this formulation, each task can have its own data source and different tasks can even operate on differently sized input.<sup>1</sup>

---

1. Fully connected layers are re-interpreted as 1-by-1 convolutional layers.



### 4.5.1 Uneven Gradients Problem

Initial attempts at training a colorizer and a jigsaw solver together, resulted in features reminiscent of a network trained only for the jigsaw task. Upon closer inspection, it turned out that the gradients coming from the jigsaw loss dominated the colorization loss in terms of size of gradient norms. A consequence of this can be seen in fig. 4.6, where the first convolutional filters only resemble those from a jigsaw solver and not from a colorizer.

There are many reasons why this might happen, especially with such network diversity where one uses a hypercolumn and the other one does not. Here is a far more simple example that illustrates how easily this can happen. Imagine two linear classifiers sitting atop a base network with similar types of tasks. The weight gradients are directly proportional to the loss,  $\|\nabla_{\mathbf{w}} L\| \propto L$ , and it is easy to show that if we change the loss to  $L' = \alpha L$ , each element of the gradient is proportionally changed as well:

$$\frac{\partial L'}{\partial w_i} = \frac{\partial L'}{\partial L} \frac{\partial L}{\partial w_i} = \alpha \frac{\partial L}{\partial w_i} \quad (4.8)$$

As a result, we can change the influence of the two losses. However, this should not lead to the conclusion that because two losses are similarly scaled so will their gradients be. There are many aspects underlying this discrepancy, such as choice of loss and structure and initialization of task-specific appendages.

We explore two options for making sure the gradients are well-balanced and that the contributions are close to equal. Both solutions involve optimization algorithms that are *loss scale invariant*, meaning the gradients do not change if we multiply the loss by an arbitrary factor.

### 4.5.2 *Separate Adaptive Optimizers*

There are many popular choices of gradient optimizers (*e.g.*, SGD, Adadelta, Adam). We will phrase these optimizers as being pre-processing routines of the gradient vector. The network weights are then updated based on the pre-processed gradient and the learning rate. For instance, in this view of optimizers, Stochastic Gradient Descent (SGD) is the identity function, since all it does is perform the update step with the raw gradients. The routine does not need to be a mathematical function and can be a subroutine with internal state. For instance, if we add momentum [94], the routine is an exponential smoother with an internal state that keeps track of the gradient of the last time frame. An adaptive optimizer is when the routine normalizes the gradient and thus becomes invariant to the loss scale.

In multi-task learning, separate networks are maintained for each task. Forward-backward passes compute the raw gradients for each instance of the base network and these are then aggregated (by summation or averaging) into a single gradient. This gradient is then passed through an optimizer pre-processing routine and finally applied to update the weights of each instance of the base network. If `optimizer` is the gradient pre-processing routine,  $\mathbf{g}_m$  the gradient of task  $m$ , the final gradient  $\mathbf{g}$  is computed as:

$$\mathbf{g} \leftarrow \text{optimizer} \left( \frac{1}{M} \sum_t \mathbf{g}_m \right) \quad (4.9)$$

One solution to the uneven gradients problem is to first change the order around, so that the gradient pre-processing is performed separately for each task before the aggregation:

$$\mathbf{g} \leftarrow \frac{1}{T} \sum_m \text{optimizer}_m(\mathbf{g}_m) \quad (4.10)$$

Now there are  $M$  separate optimizers, one for each task  $m$ . If adaptive optimizers are used, then any imbalance will be normalized away before aggregation. We refer to this solution to the uneven gradients problem as using separate adaptive optimizers.

There are potential issues with this. First, let us discuss some of the popular adaptive optimizers, such as Adagrad [28], Adadelata [134], RMSprop [115], and Adam [58]. What all these optimizers have in common, apart from being loss scale invariant, is that they in various ways normalize the size of gradients *per feature*. This may in some cases cause unwanted acceleration of learning in certain areas of the network. For instance, in the beginning of training, it is common for early layer gradients to be particularly small, since changes are dampened by the randomly initialized network. As a result, it can take a while until the early layers start updating properly. Adaptive optimizers are more aggressive and will take small gradients and amplify them. In our experience, this has both the potential to benefit *and* damage representation learning. We observe this in table 4.5, where Adam consistently under-performs compared to SGD across all tasks. The aggressiveness can be softened by introducing a small constant,  $\epsilon$ , in the gradient normalization denominator. However, this  $\epsilon$  technically breaks loss scale invariance and the greater the  $\epsilon$  is (more softening), the more this is broken. Typical values for  $\epsilon$  are extremely small (*e.g.*,  $10^{-5}$ ) and only meant to avoid numerical instabilities.

Additionally, as with momentum, many optimizers use an internal state. If we require a separate optimizer state for each task, we incur additional memory overhead. For instance, the parameters of VGG-16 takes roughly 0.5 GiB and corresponding state for an Adam solver takes 1 GiB. To use separate Adam instances for each task, this number needs to be multiplied by  $M$ , which quickly becomes a significant portion of the GPU memory.

### 4.5.3 Globally Normalized SGD (*NormSGD*)

We propose another solution that makes sure that gradients are balanced between tasks, using a single optimizer and not requiring an adaptive optimizer. Although it can be coupled with any optimizer, we will use it with mini-batch momentum-SGD and refer to the combination as NormSGD. The trick is to globally normalize the gradients using the pre-processing

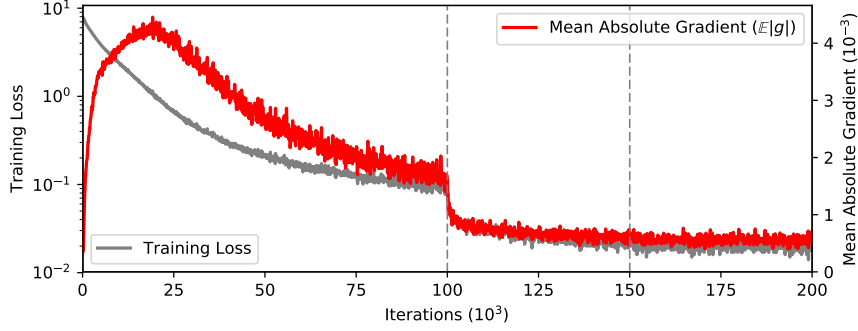


Figure 4.4: **Gradient norm.** This shows the loss (in gray) and gradient norm (in red) over time for supervised training on CIFAR-100. We draw attention to two observations. First, there is a warm-up phase, where gradients quickly increase in norm. Second, after this phase the norm drops over time, especially when the learning rate is dropped by a factor 10 at 100,000.

function

$$\text{norm}(\mathbf{g}) = \frac{\mathbf{g}}{\frac{1}{P}\|\mathbf{g}\|_1} = \frac{\mathbf{g}}{\mathbb{E}[|g|]} = \frac{\mathbf{g}}{\frac{1}{P}\sum_p |g_p|}, \quad (4.11)$$

where  $P$  is the total number of parameters for the entire base network. This can be combined with other optimizer pre-processing routines (*e.g.*, momentum) by making subsequent calls. This normalization is reminiscent of RMSprop [115] and Adadelta [134], where each gradient element is divided by its absolute value. However, we instead compute a single normalization statistic and use it for all elements of the gradient. This preserves the gradient direction and does not boost individual features with low gradient.

However, this still changes the nature of SGD. To see why, we plot in fig. 4.4 the size of the gradient over time when training with standard SGD. We first observe that there is an acceleration phase where gradients increase in size as the network starts finding the quickest paths to loss reduction. Next, as the loss keeps dropping, so does the size of the gradients. In other words, two things may happen differently when globally normalizing the gradients: (1) It may be a bit too aggressive in the early stages when the gradient norm is low, and (2) the learning rate only drops according to schedule without also being naturally diminished as the loss approaches zero. We offer corrections to these to bring it even closer to SGD.

The first issue of aggressive starts is minor and can be solved by using a brief period of learning rate warm up. A fix to the second problem is much more pressing, since without it we have observed occasional training instabilities and divergence. This is perhaps because gradients with small norm and low signal-to-noise ratio get boosted, increasing the risk of jolting the network into a bad state. The fix is to freeze the gradient norm statistics before reaching this point, which in our experience can be anytime before dropping the initial learning rate, but after the initial warm-up phase.

NormSGD can be beneficial for single-task training. Loss scale and learning rate are according to eq. (4.8) two equivalent ways to control the size of gradient steps. NormSGD eliminates this over-parameterization, giving the control rightly to the learning rate alone. We have observed that it is much easier to switch between losses, without having to re-calibrate the learning rate. Furthermore, it can be applied prior to gradient aggregation when training  $T$  tasks simultaneously, as in (4.10).

What guarantees do we have about the “contribution” of each task under this gradient transformation? By design, all pre-processed task gradients have the same  $L_1$  norm, *i.e.*  $\|\text{optimizer}(\mathbf{g}_i)\|_1 = \|\text{optimizer}(\mathbf{g}_j)\|_1$ , for all  $i, j$ . However, if we consider contribution to mean how much of a single task gradient is preserved in the aggregated gradient (for instance quantified by  $\mathbf{g} \cdot \mathbf{g}_i$ ), then we have no guarantees beyond trivial upper bounds. For instance, in a three-way multi-task loss, we could theoretically end up having two sets of perfectly canceling gradients, in which case the aggregated gradient would be only a scale factor different from the third one. Seen in a different way, each task has the same vote, but a vote does not guarantee influence. This can be seen as a feature, since it will favor updates with a quorum. We present evidence in table 4.5 supporting the benefits of NormSGD, along with qualitative results in fig. 4.6 that suggest even contributions of tasks.

#### 4.5.4 Round-Robin Scheduling

Despite memory saving of not having separate instances of an adaptive optimizer, training multiple losses still does not scale well in the number of tasks  $M$ . There is work to make back-propagation on computational graphs more memory efficient [16, 37], used for instance by UberNet [60]. As an alternative, we can keep only one task active, switching task in a circular order after a fixed time slice or *quantum* ( $Q$ ). If we set the quantum to one iteration ( $Q = 1$ ), it will be close to joint training. However, constant context switching will significantly slow down training. Ideally, we set the quantum high enough for the context switch to become a negligible or at least justifiable cost.

A context switch involves marshaling the compute graph for one task and transferring it from the GPU memory to the CPU memory, as well as reviving another task’s state from the CPU into the GPU. Even if your favorite deep learning software does not explicitly allow such operations, standard snapshotting to file can be used on a RAM-mounted file system (*e.g.*, `ramfs` or `tmpfs` on Linux).

When using round-robin scheduling, we never perform gradient aggregation (eq. 4.10). Nevertheless, similar issues of unbalanced gradients still apply. The memory overhead of multiple adaptive optimizers is no longer an issue, which makes them viable. However, if adaptive optimizers do not perform well (as for us), NormSGD still works well for round-robin scheduling.

## 4.6 Evaluation

We evaluate the aggregation techniques on a variety of supervised pretraining tasks created from CIFAR-100. We use supervised tasks because they require less training and give a clearer signal of the benefits since we can carefully control the level of potential benefits from multi-task learning. Once we have developed a method that works well in this setting, we apply it to self-supervision in section 4.7.

Name: <i>Deep</i>				Name: <i>Shallow</i>			
Type	Size/Stride	Channels	Dropout	Type	Size/Stride	Channels	Dropout
Conv	$5 \times 5/1$	64		Conv	$5 \times 5/1$	8	
Conv	$3 \times 3/1$	64		Pool	$2 \times 2/2$	-	
Pool	$2 \times 2/2$	-		Conv	$3 \times 3/1$	16	0.1
Conv	$3 \times 3/1$	128	0.1	Pool	$2 \times 2/2$	-	
Conv	$3 \times 3/1$	128	0.1	Conv	$3 \times 3/1$	32	0.2
Pool	$2 \times 2/2$	-		Pool	$2 \times 2/2$	-	
Conv	$3 \times 3/1$	192	0.2	Conv	$3 \times 3/1$	32	0.3
Conv	$3 \times 3/1$	192	0.2	Conv	$3 \times 3/1$	192	0.3
Pool	$2 \times 2/2$	-		Pool	$2 \times 2/2$	-	
Conv	$3 \times 3/1$	192	0.3	Flatten	-	3072	
Conv	$3 \times 3/1$	192	0.3	Task	-	100	
Pool	$2 \times 2/2$	-					
Flatten	-	3072					
Task	-	100					

Table 4.1: **Test architectures.** Description of architectures *Deep* and *Shallow* for distillation and multi-task experiments.

#### 4.6.1 Distillation

We evaluate our ability to do task-driven and task-agnostic distillation. For this, we use two typical convolutional networks, *Deep* (8 layers) and *Shallow* (5 thin layers) described in detail in table 4.1. The *top layer* has 3,072 features and feeds into a *task layer* with typically 100 features (depending on the task). Five distillation scenarios are formulated and described in table 4.2. The prefix *Task* denotes traditional distillation that occurs at the task layer, while *Top* indicates task-agnostic distillation at the top layer. For the latter, we use a held-out portion of the training data to see how well it can train a linear classifier on the distilled network’s top layer. The problems are briefly summarized as *Copy* (make an exact copy), *Compress* (compress into smaller network), and *Ensemble* (compress multiple networks into one).

All models are evaluated on the CIFAR-100 test set. The distillation loss is evaluated in table 4.3. Temperature generally offers an improvement. The gains are greater when the task is harder and we are compressing into a smaller network. For *Top-Copy*, the network copy is close to perfect even for squared  $L_2$ , so temperature offers no improvement. For

Problem	Description
<i>Task-Copy</i>	<ol style="list-style-type: none"> <li>1. Train <i>Deep</i> on all 50,000 samples</li> <li>2. Duplicate model at task layer using all 50,000 samples</li> </ol>
<i>Task-Compress</i>	<ol style="list-style-type: none"> <li>1. Train <i>Deep</i> on all 50,000 samples</li> <li>2. Compress into <i>Shallow</i> at task layer using all 50,000 samples</li> </ol>
<i>Task-Ensemble</i>	<ol style="list-style-type: none"> <li>1. Train six <i>Deep</i> on all 50,000 samples and ensemble</li> <li>2. Compress into <i>Deep</i> at task layer using all 50,000 samples (with data augmentation described in [69] and no student dropout)</li> </ol>
<i>Top-Copy</i>	<ol style="list-style-type: none"> <li>1. Train <i>Deep</i> on first the 40,000 samples</li> <li>2. Duplicate model at top layer using the first 40,000 samples</li> <li>3. Add a task layer and train a linear classifier (do not fine-tune end-to-end) using the last 10,000 samples</li> </ol>
<i>Top-Compress</i>	<ol style="list-style-type: none"> <li>1. Train <i>Deep</i> on first the 40,000 samples</li> <li>2. Compress into <i>Shallow</i> at top layer using the first 40,000 samples</li> <li>3. Add a task layer and train a linear classifier (do not fine-tune end-to-end) using the last 10,000 samples</li> </ol>

Table 4.2: **Distillation problems.** Problems to tests various model distillation scenarios. The *Copy* problems are not what we typically refer to as distillation, since the information is not transferred into a smaller network. However, it still uses the same training mechanisms and it is interesting since a perfect copy should be possible, so any in performance loss is caused entirely by the training procedure and not by reduced model complexity. All problems are evaluated on the CIFAR-100 test set. See fig. 4.5 and table 4.3.



Loss	<i>Task-Ensemble</i>	<i>Task-Copy</i>	<i>Task-Compress</i>	<i>Top-Copy</i>	<i>Top-Compress</i>
$D_{AB}^{(0,0)} (L_2)$	$61.7 \pm 0.1$	$57.8 \pm 0.2$	$36.1 \pm 0.3$	$52.5 \pm 0.1$	$38.4 \pm 0.3$
$D_{AB}^{(\alpha,0)}$	$62.5 \pm 0.1$	$58.6 \pm 0.4$	$38.0 \pm 0.3$	$52.6 \pm 0.2$	$39.0 \pm 0.6$
Teacher	66.0	$59.7 \pm 0.3$	$59.7 \pm 0.3$	$52.2 \pm 0.5$	$52.2 \pm 0.5$

Table 4.3: **Distillation loss.** (Test accuracy, %) We evaluate on five student-teacher tasks (see section 4.6.1) the importance of temperature-adjusted KL divergence ( $\alpha \neq 0$ ) as opposed to a squared  $L_2$  loss ( $\alpha = 0$ ). Temperature becomes more important with higher degree of compression and less important at non-task layers (*Top-* tasks). Parameters of  $D_{AB}$  work well across situations, demonstrated here by the fact that we ended up using  $\alpha = \frac{1}{4}$  for all tasks. More values of  $(\alpha, \beta)$  are explored in fig. 4.5.

*Top-Compress*, temperature helps over squared  $L_2$ , but not as much as for *Task-Compress*.

The results for *Task-Ensemble* show that we can successfully improve single-model results from  $59.7 \pm 0.3$  to  $62.5 \pm 0.1$  by ensemble training followed by model distillation with temperature. Without temperature, the improvements are somewhat lower, but still better than the baseline, at  $61.7 \pm 0.1$ .

One of the primary benefits of the new distillation loss is that it works well in diverse settings without having to re-tune the parameters  $\alpha$  and  $\beta$ . Across all five problems, we found that  $D_{AB}^{(0.25,0)}$  worked best. The old loss (4.1) can in each situation be made close to equivalent, but it would result in widely different temperatures.

Student dropout may help if training data is scarce. For instance, the two numbers for *Task-Copy* in table 4.3 drop significantly without dropout ( $57.8 \pm 0.2 \rightarrow 54.4 \pm 0.4$  and  $58.6 \pm 0.4 \rightarrow 54.7 \pm 0.3$ ). However, since we use data augmentation for *Task-Ensemble*, dropout can cause over-regularization which is why we do not use it. If we do use it, accuracy goes down ( $61.7 \pm 0.1 \rightarrow 57.2 \pm 0.1$  and  $62.5 \pm 0.1 \rightarrow 59.0 \pm 0.2$ ).

The methods of creating a teacher signal compatible with the student are evaluated in table 4.4. Feature subsets offer a significant improvement over the use of auxiliary layers (see section 4.3.4). Warm-starting the distillation with a single-task network offers faster

Method	$\dot{\cup}25\%$
Auxiliary layer	40.9
Auxiliary layer (warm start)	41.7
Feature subset	43.6
Feature subset (warm start)	43.7

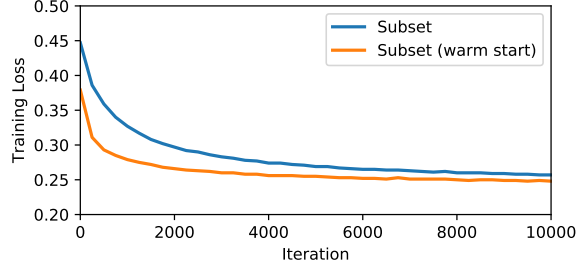


Table 4.4: **Distillation methods.** (Test accuracy, %) Distillation works well, offering a dramatic improvement over a single model (32.4%). Using an auxiliary layer to make student and teacher compatible for training works reasonably well. However, the simpler approach of taking a subset of the teacher’s features work even better. In these experiments, there is little gain in warm-starting the network with a single network’s weights. However, it does converge faster (*right*) and benefits may be more prominent on larger network architectures that are harder to train well from scratch.

convergence but modest benefits to the end results.

Furthermore, we evaluate AB divergences where  $\beta \neq 0$  on the *Task-Compress* problem. The results are compiled in fig. 4.5 and show to our surprise that several variants improve over the baseline with results statistically indistinguishable from temperature-adjusted KL divergence. This includes the symmetric  $D_{AB}^{(t,t)}$  and the scale invariant  $D_{AB}^{(t,-t)}$ . Our recommendation is to use the KL divergence line ( $D_{AB}^{(t,0)}$ ), however the AB divergence does offer fertile ground for future experimentation.

#### 4.6.2 Multi-Task Representation Learning

For multi-task representation learning, we split the CIFAR-100 training data into 40,000 samples for pretraining and 10,000 for fine-tuning. The 40,000, are split further into a wide variety of different tasks that are designated as unrelated in the multi-task regime. Each of 4 tasks can for instance randomly sample 50% of the data, which we denote  $\cup 50\%$ , where  $\cup$  denotes that each sample is independent. Alternatively, if the data is split into 4 pieces, we denote it  $\dot{\cup}25\%$ , where the added dot indicates the tasks for a *disjoint* partition. The splits can be done by random samples or by class. For instance, 4 tasks split using  $\cup 50\%$  by class, means that each task gets a random subset of 50% of the classes and all the samples that go

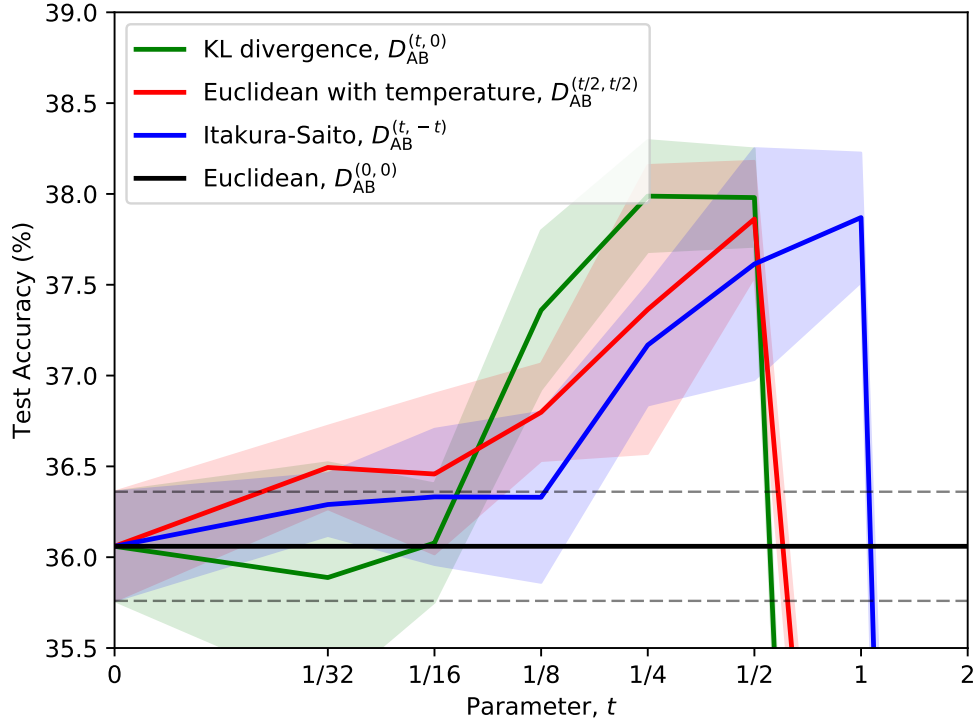


Figure 4.5: **AB divergence as a distillation loss.** We evaluate three types of AB divergences as a distillation loss on the *Task-Compress* problem (see section 4.6.1). The parameter  $t$  moves along different straight lines on the  $(\alpha, \beta)$  parameter space, with colors corresponding to fig. 4.1. For KL divergence and Euclidean,  $t$  corresponds to inverse temperature ( $T^{-1}$ ). All values improve over  $L_2$  loss ( $t = 0$ ), but reach abrupt instabilities as they go too far away from the origin. There is no statistically significant winner among the top values ( $38.0 \pm 0.3$ ,  $37.9 \pm 0.3$ , and  $37.9 \pm 0.4$ ). However, KL divergence remains a natural choice, in addition to having a broader peak. Visualization of these losses can be seen in fig. 4.2

with it. This particular situation may result in classes lacking any pretraining representation at all.

The generated datasets are now considered separate tasks and will serve as analogs to different self-supervision methods. A representation is now learned using any of method outlined in this chapter. For instance, in the case of model distillation, each task is trained separately, the task layer is discarded, and model distillation is performed at the top layer. For joint training, all tasks are attached to the top layer of the base network and trained together. Regardless of the method used, it will produce a trained base network without a task layer. A task layer is then attached to this base network and trained on the 10,000 held out for fine-tuning. In order to emphasize the representation learning, we do not use end-to-end fine-tuning and only the new task layer is allowed to update.

Results are presented in table 4.5. First, we note that distillation does quite well, offering substantial improvements over the baseline of using only a single task for representation learning. It is often on par with split-weights training and sometimes does better, even though it is an online method. Split-activations, the only other method that enjoys the benefits of an offline method, fails to train at all for 10 tasks and is strongest for two tasks (since this eliminates the least amount of parameters from pretraining). However, we see no benefits of this model since at two tasks the distillation is still superior with a 7-point margin. In fact, distillation is as good as the best online method when combining only two tasks.

Joint training consistently does well, although our fears of adaptive methods are confirmed by consistently under-performing compared to SGD by about 2 points. It may seem that using 4 tasks of 50% overlapping classes should be better than 4 tasks with only 25% disjoint classes. However, there is only a slight trend in this direction, which may be explained by the fact that in the overlapping case, a few classes fail to get representation at all.

The right-most column is labeled *Mixed*. For these four tasks, we use four distinct losses for the task: multi-class softmax KL divergence, squared  $L_2$ , multi-label sigmoid KL divergence, and multi-label hinge loss. The softmax and sigmoid both train a decent model alone, but  $L_2$  and multi-label hinge loss struggle and bring the single task mean down. Since they struggled individually, we did not evaluate this for offline methods; it would not be fair to give them failed models that they are not allowed to change. Online methods on the other hand can benefit from joint training, in that maybe the failed losses simply had a hard time getting close to a good solution or were too prone to diverge into failed states. Training them together seems to alleviate this, since most methods are able to train reasonable models. First, we see that Adam does better than SGD. It is not entirely clear why, since Adam does not individually normalize the tasks. Even more surprisingly is that using separate Adam optimizers (“Multi-Adam”) as described in section 4.5.2 does *worse* than Adam. Perhaps it is boosting poor gradients from the struggling methods too much. NormSGD addresses and resolves the issues of SGD to the surprising extent that it becomes on par with results using the same loss.

Are there still settings where Multi-Adam may be beneficial over Adam? Yes, if we do a more contrived mixed loss, by simply using softmax KL divergence for all, but with each loss multiplied by a random factor. In this setting, Multi-Adam and NormSGD are equivalent to their same-loss counter-parts, while Adam and SGD do take a performance hit. Even though there are situations where Multi-Adam does solve a problem that Adam does not, we still prefer NormSGD due to the trend toward better results for representation learning.

Table 4.6 shows that joint training with NormSGD can be implemented using round-robin scheduling. This approach scales better in  $M$  in terms of memory use. If tasks are sufficiently different, the time costs of a forward-backward pass may vary. In joint training, this means that all other tasks must wait for the bottleneck task; an issue that is avoided using round-robin scheduling.

Tasks	4	4	2	4	10	4
Task loss	Same	Same	Same	Same	Same	Mixed
Classes		$\dot{\cup}$ 50%	$\dot{\cup}$ 50%	$\dot{\cup}$ 25%	$\dot{\cup}$ 10%	$\dot{\cup}$ 25%
Sample size	$\dot{\cup}$ 25%					
Single task (mean)	38.4	42.1	41.6	32.4	24.4	16.8
Single task (max)	38.8	43.0	42.1	33.3	26.5	32.2
Distillation (subset)	44.0	46.7	54.2	47.2	42.2	-
Split-activations	29.4	39.8	47.3	33.0	1.0	-
Split-weights	47.0	50.3	52.3	46.0	25.5	-
Joint (Adam)	52.1	49.2	51.7	49.3	45.2	46.6
Joint (Multi-Adam)	52.9	50.7	52.8	49.5	44.3	44.3
Joint (SGD)	54.1	52.2	54.0	51.3	46.5	38.5
Joint (NormSGD)	54.4	51.4	54.1	51.5	47.9	<b>51.1</b>
Pretrained on full dataset	55.5	55.5	55.5	55.5	55.5	55.5

Table 4.5: **Multi-task learning.** (Test accuracy, %) Each task is a subset of CIFAR-100, either by class or by sample size. The subset can be a disjoint partition ( $\dot{\cup}$ ) or independently sampled per task allowing overlaps ( $\cup$ ). The *single task* results should be considered a baseline; a method fails to have practical use if it falls below this value. On the other end, we do not expect methods to exceed pretraining on the entire dataset, so this can be considered an upper bound. Two of the mixed losses did not train well individually, causing the single task mean to be low. It is unfair to evaluate them for offline methods. However, online methods have the potential to prop up poor choices of losses, which is exactly what happened with NormSGD (shown in bold) and to a lesser degree with Adam. Multi-Adam did worse than Adam, ruling it out as a solution to uneven losses. Joint training can also be substituted by round-robin scheduling (see table 4.6).

Method	$Q$ ( $\times 10^3$ )	$I$	4 Same $N \cup 25\%$	4 Same $C \cup 50\%$	2 Same $C \cup 50\%$	4 Same $C \cup 25\%$	10 Same $C \cup 10\%$	4 Mixed $C \cup 25\%$
Joint	-	200	54.4	51.4	54.1	51.5	47.9	51.1
Round-robin	1	200	54.4	52.7	53.6	52.2	47.7	51.5
Round-robin	10	200	54.2	51.3	52.2	51.0	48.2	51.2

$Q$ : Quantum (time between task switch),  $I$ : Iterations,  $M$ : Tasks

Table 4.6: **Round-robin task scheduling.** (Test accuracy, %) Keeping only a single task active at any time is an alternative to joint training. This often works equally well as joint training, even when the quantum is high. For instance, when the quantum is  $Q = 10,000$ , the total iterations  $I = 200,000$  (learning rate drops at 100,000 and 150,000) and tasks  $M = 10$ , then each task only gets a single segment at the original learning rate and only half at once-dropped and the other half at twice-dropped learning rate. Despite such high quantum, the last row has almost no effect on the results. The only task that suffers a bit is when  $M = 2$ . All methods use NormSGD.

## 4.7 Multi-Proxy Self-Supervision

We finally turn our attention to combining multiple self-supervision methods. Since joint training with NormSGD shows the most promise for multi-task representation learning, we now apply it to multi-proxy self-supervised representation learning. We use three self-supervised tasks outlined below. Our implementation does not use round-robin scheduling, although it would be an appropriate strategy for a future implementation, especially if  $M$  is increased further.

Following chapters 1 and 3, we evaluate the representation learned from multi-proxy training on classification and semantic segmentation from the PASCAL VOC challenges (see section 3.4.1).

### 4.7.1 Proxy Tasks

A brief summary of the different self-supervision methods that are combined.

**Colorization.** The colorization method is described in chapters 2 and 3. We use a re-implementation in TensorFlow (as opposed to Caffe used in earlier chapters), and this might

be a reason why it tests lower than our Caffe implementation with the same amount of training. When training jointly, the first convolutional layer must have three-channel filters, so we instead feed it an RGB-encoded grayscale version, where the same intensity image is replaced three times.

**Jigsaw.** The original jigsaw method [88] uses a modified version of AlexNet and does not pretrain `fc6` and `fc7` at all. This is to allow each patch to be rather small (128-by-128) so that a 3-by-3 puzzle can be used. We want the jigsaw solver to contribute to all layers, so we opted for a 2-by-2 puzzle that are fed 500-by-500 images, with each puzzle piece the canonical input size at 227-by-227 (the extra pixels are necessary for wiggle room between the pieces). At 2-by-2, we use all 24 possible permutations of the puzzle as the output of the prediction task. We use ImageNet [100] and Places205 [139] as a combined source of unlabeled images for both Colorization and Jigsaw.

**Video.** For video, we use a novel approach developed for the purpose of this experiment. It is inspired by Pathak *et al.* [90], however we take a simpler approach of leveraging optical flow for ease of implementation.<sup>2</sup> We compute Farnebäck optical flow [33] and associate it with a single frame. We sample random locations uniformly from the image. Next, for each location we sample another location anchored to the first by two independent Gaussian distributions. For these pairs of locations, the relative optical flow is computed and its amplitude is placed into one of 32 bins. Sparse hypercolumns (see section 2.3.7) are extracted and the paired hypercolumns are concatenated and fed to a prediction layer that outputs a distribution over the 32 bins of relative flow amplitude. Note, since we are only considering relative flow, this method is invariant to camera translation and therefore to some extent invariant to camera rotation. We use the Hollywood2 [78] dataset as source of unlabeled video input. Since this is a small dataset and we do not plan to use any of the labels, we use both the training and testing data. This consists of 2517 clips of median length 10 seconds.

---

2. Simply using their pre-processed data would be easier, but it had not been publicly available yet.



### 4.7.2 Method

The three methods share the same base network. We implement this by keeping separate instances of this network with tied weights. This is necessary since we feed the networks differently sized inputs from different data sources. If two methods use the same data source and size, they can use a single network instance with two sets of task-specific appendages. Keeping separate network instances also allows placing them on different GPUs for parallel processing, with a synchronization phase at the end of each iteration.

The base network is AlexNet and we use NormSGD (section 4.5.3) for training. Colorization and Video both use complete hypercolumns, extracted from all layers, and a fully connected layer with 1024 channels prior to the task layer. We train for 2M iterations, with factor 10 drops of the learning rate at 1M and 1.5M. Batch sizes are 8 when tasks are trained individually and 4 for each task when trained jointly. This means that “C+J” sees the same amount of data, but the gradients are likely noisier. To avoid making the gradients even noisier, we did not drop this further for “C+J+V,” even though this technically means more data was fed during training. The code for jointly training models, with additional implementation details for all three methods, is made publicly available.<sup>3</sup>

### 4.7.3 Results

Results are seen in table 4.7. We try combining both two tasks (Colorization and Jigsaw), and three tasks (Colorization, Jigsaw, and Video). However, the downstream performance results neither increase nor decrease as a result of multi-proxy learning.

Training Colorization and Jigsaw together with SGD, we observe that Jigsaw gradients dominate the Colorization gradients. As a result, the filters of the first convolutional layer were similar to the filters of Jigsaw trained alone. Using NormSGD, although it does not result in improved downstream results, it produces filters that have the appearance of being

---

3. <https://github.com/gustavla/self-supervision>

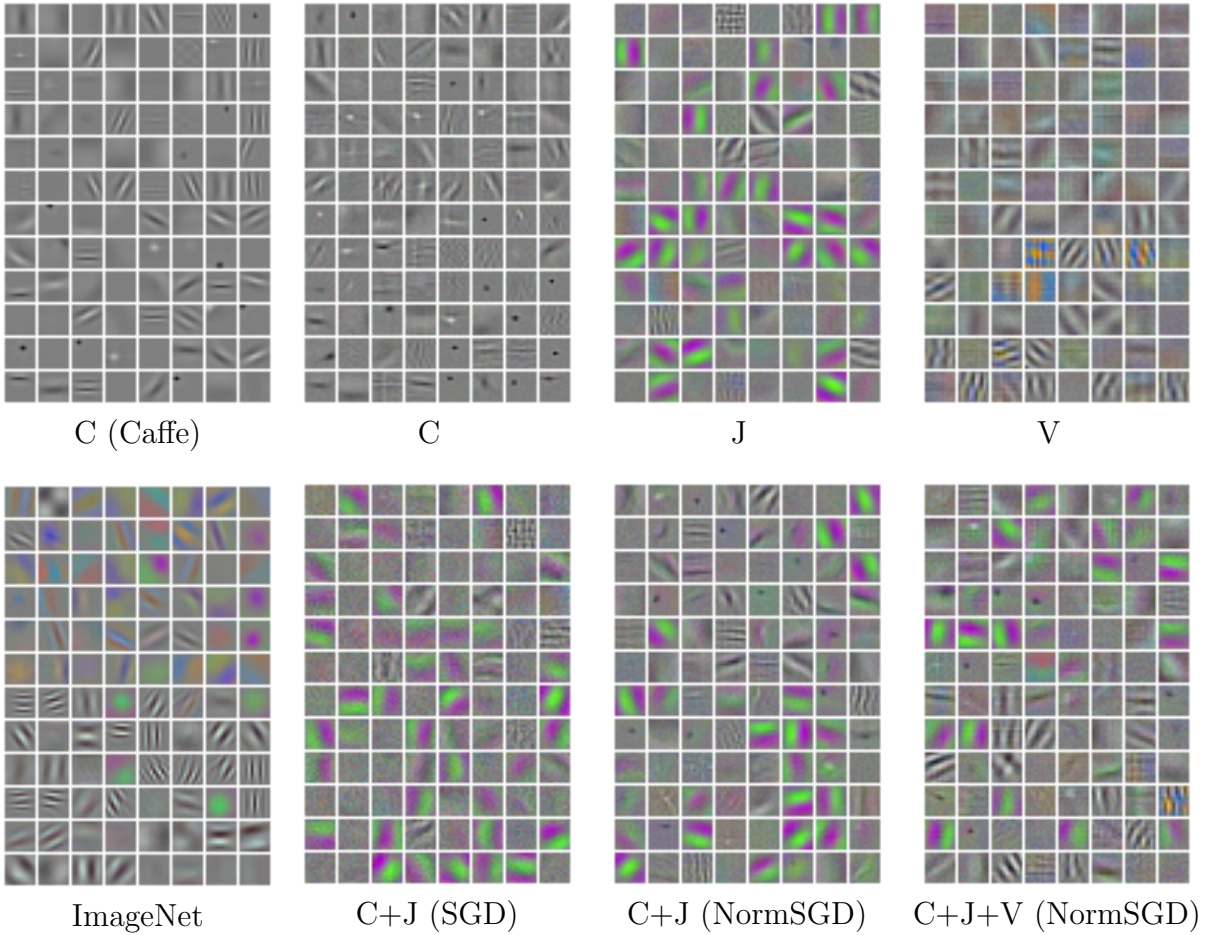


Figure 4.6: **First convolutional filters.** The first filters of AlexNet are large enough for meaningful visual inspection. We note that all three self-supervised methods have very distinct characteristics. Colorization (C) is grayscale and has Gabor-like filters as well as blobs. We also show our Caffe implementation from chapter 3, which was trained longer and is therefore a bit smoother. Jigsaw (J) oddly has a lot of green-purple edges, although this is consistent with the original paper [88]. Video (V) has more color with broad edges and many high-frequency Fourier filters (without tapering off as Gabor filters). Our initial attempt at combining two methods (C+J) resulting in one dominating the other and filters indistinguishable from J alone (except a bit grainier here, due to shorter training). This was resolved by NormSGD and we get a more even mix of green-purple edges (from J) and blobs/Gabor filters (from C). With three proxy tasks we see characteristics of all methods, suggesting a fairly even focus on all three tasks. The diversity of filters for “C+J+V” makes it the closest to the filters trained on ImageNet. Each set of filters is individually stretched out in scale, in a symmetric way such that middle-gray represents 0.

more evenly mixed between both tasks (see fig. 4.6).

To further investigate what might be happening, we try pretraining on one proxy task to see if it helps another proxy task. These results are plotted in fig. 4.7 and indicate that tasks generally make the other tasks converge faster. However, we also see that initializing with a jointly trained network makes all three tasks quickly learn the task much better than using either of the other self-supervised tasks. In summary, we have trained a more general network by training jointly and it is conceivable that there exist tasks where this would be expressed. However, our tests on classification and semantic segmentation do not give expression to these potential benefits.

## 4.8 Conclusion

In this chapter we have considered a wide range of methods for combining proxy tasks that learn a single representation. This goal is different from multi-task learning, since we do not really care how we perform on the throw-away proxy tasks. We consider both offline methods (train separately and combine) and online methods (train together). For offline methods, task-agnostic distillation by taking feature subsets at the top layer is a competitive method. In developing this approach, we also develop a new distillation loss that can be used for at task layers as well as task-agnostic layers. For online methods, we show that joint training is effective, but it is important to be aware of the possibility of uneven gradients. We address this problem by proposing NormSGD, which is invariant to loss scale and thus suited when combining disparate losses. If the memory overhead of joint training becomes a problem, we show that training a single task at a time using round-robin scheduling is also fine for representation learning.

Despite promising results on test benchmarks, we show no improved results by jointly training self-supervision methods. This is a curious negative result that could suggest that there is not much to gain from the apparent diversity of the different self-supervision methods.

Method	Classification (%mAP)	Segmentation (%mIU)
No Pretraining	46.2	23.5
C (Colorization)	61.1	36.3
J (Jigsaw)	60.0	33.7
V (Video)	60.6	35.9
C+J	59.2	35.5
C+J+V	60.2	36.1

Table 4.7: **Multi-proxy self-supervision.** (AlexNet) We implement three entirely separate self-supervision methods (see section 4.7.1) with similar pretraining benefits. Two or three methods are then trained jointly using NormSGD. Note, colorization results for AlexNet are even better in table 3.1 due to longer training and possibly subtle implementation details.

However, it could also mean that harnessing the diversity is more difficult than we envisioned, and the methods outlined here is only a first step in achieving this long-term goal. If this is the case, we hope that our work can offer a good starting point.

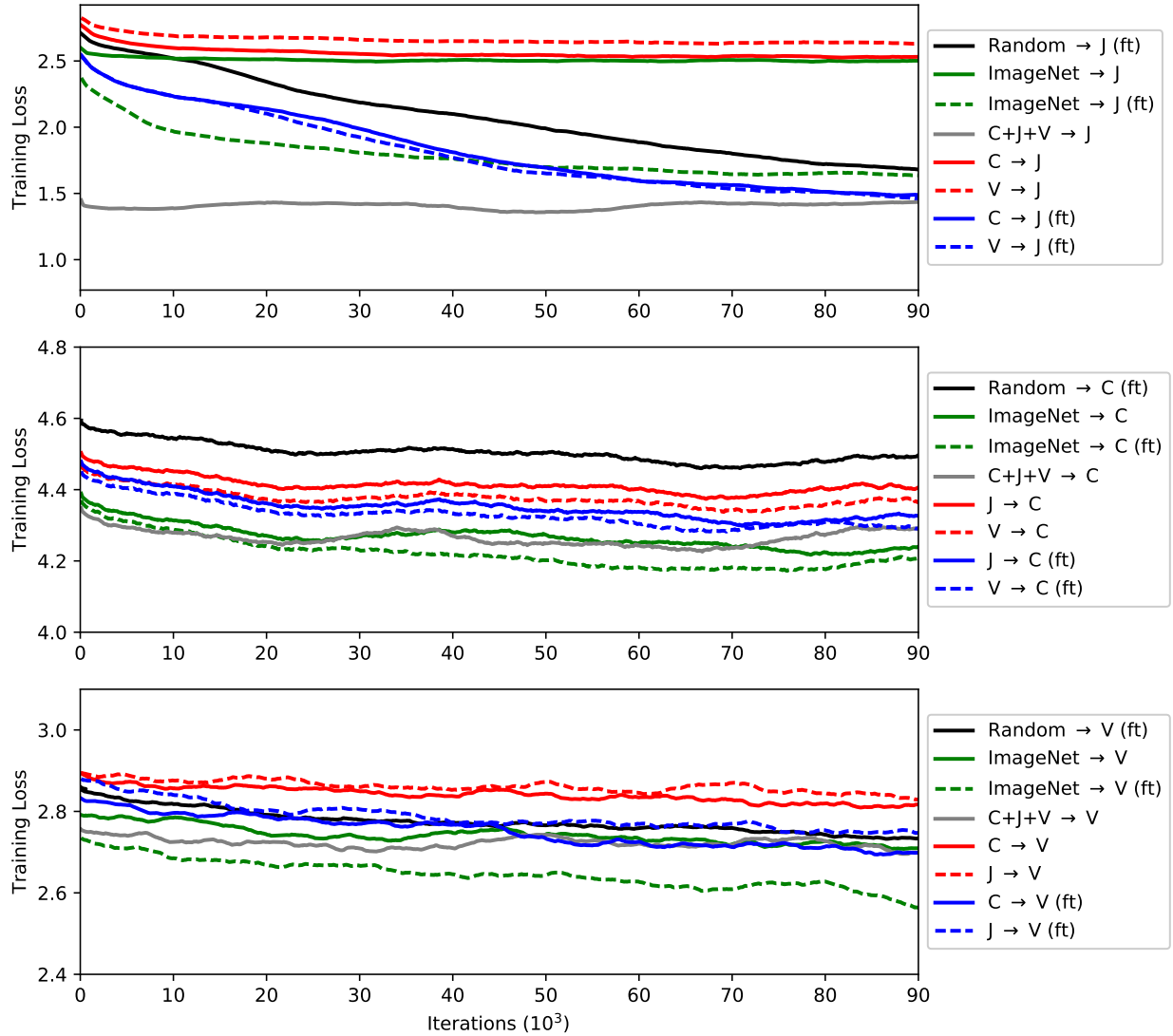


Figure 4.7: **Inter-proxy training loss.** We plot the initial learning curves for the tasks C (Colorization), J (Jigsaw), and V (Video). The notation “ImageNet  $\rightarrow$  C (ft)” means that Colorization was trained after initializing from an ImageNet pretrained network, with “ft” indicating end-to-end fine-tuning as opposed to task-specific fine-tuning only. The first observation we make is that initializing with other self-supervised tasks is almost always beneficial, with Video the only exception where it did not help. Moreover, Jigsaw, which is the only one without hypercolumns, does not do well without fine-tuning, even when initializing with ImageNet. We also try initializing with “C+J+V” and we see that the network as expected has learned all three tasks to some degree. Finally, it is hard to get clear signals from C and V, since they are difficult tasks and the dynamic range of the loss is small even over long training periods. We improved this by turning off randomizing samples for Colorization, which is why all lines share trends.

## CONCLUSION

We have demonstrated two unsupervised methods for representation learning, highlighting limitations of traditional methods of unsupervised learning. The first method failed due to the limitations of greedy training, which makes it difficult to leverage the model complexity of deep networks. The second method overcomes this issue through end-to-end training. However, it still falls short since it uses an unsupervised loss based on reconstruction error that fails to emphasize high-level semantics.

Instead, we use a supervised loss on a task manufactured from unlabeled data (self-supervised). We propose to do this with automatic colorization, which we separately develop into a graphics application with state-of-the-art results. Colorization turns out to be an excellent vehicle for representation learning. The primary reason for its success is that the task requires high-level visual understanding, unlike the reconstruction error used in traditional unsupervised methods. We show that this new proxy task leads to significant progress in closing the gap between supervised and unsupervised pretraining.

We hope that this gap can be further closed by combining multiple self-supervision techniques through model aggregation or joint training. However, we have shown that this is nontrivial as is evidenced by our extensive investigation showing no improvement over single-model results. Further work in this direction may still turn out to be worthwhile, in which case we hope that our progress offers a foundation for future work.

# APPENDIX A

## PERMUTATION EM

### A.1 Introduction

We present further details and derivations of Permutation EM described in section 1.2.4.

#### A.1.1 Cyclic Groups

Even though the algorithm is general to any set of permutations, it is particularly suited for products of cyclic groups. Consider for instance two cyclic groups of image transformations: one group of rotations  $(G_{\text{rot}}, \circ)$  of size  $R$  and one group of edge polarities  $(G_{\text{pol}}, \circ)$  of size  $T = 2$ . The symbol  $\circ$  denotes function composition of the transformations. Either of these two cyclic groups can be used as a latent transformation, as well as their direct product  $G = G_{\text{rot}} \times G_{\text{pol}}$ . Let the transformations be denoted  $(g_{\text{rot}}, g_{\text{pol}}) \in G$  and  $g = g_{\text{rot}} \circ g_{\text{pol}}$ . Let  $g_p$  denote the transformation  $p$  in  $g$ . For each sample, a complete sample can be constructed by concatenating all transformations applied to the sample:

$$\mathbf{x} = [g_1(x), g_2(x), \dots, g_P(x)] \quad (\text{A.1})$$

Each cyclic group is generated by a single transformation, such as  $\Phi_{\text{rot}}(x)$  (rotate  $\frac{360}{R}$  degrees) and  $\Phi_{\text{pol}}(x)$  (flip intensity).

#### A.1.2 Permutations

Let  $\sigma_N = (0\ 1\ \dots\ N-1)$  be a cyclic permutation.<sup>1</sup> We create the permutation matrix by letting  $\sigma_R \times \sigma_T$  generate pairs of indices, where one cycles through the rotations and one

---

1. This is written in cycle notation and means that  $\sigma_N(n) = (n+1) \bmod N$ .

through the polarities. Finally, we create a bijection between these pairs into a flattened index space, corresponding to the order in which we did the transformations.

As an example, let  $R = 3$  and  $T = 2$ , and let the flattened index be  $i = Rt + r$ , so that indices  $\{0, 1, 2\}$  are all rotations of one polarity and  $\{3, 4, 5\}$  are all rotations of the other. The matrix becomes

$$A = \begin{bmatrix} \sigma_R & \sigma_R + R \\ \sigma_R + R & \sigma_R \end{bmatrix} = \begin{pmatrix} 0 & 1 & 2 & 3 & 4 & 5 \\ 1 & 2 & 0 & 4 & 5 & 3 \\ 2 & 0 & 1 & 5 & 3 & 4 \\ 3 & 4 & 5 & 0 & 1 & 2 \\ 4 & 5 & 3 & 1 & 2 & 0 \\ 5 & 3 & 4 & 2 & 0 & 1 \end{pmatrix}, \quad (\text{A.2})$$

where we allow  $\sigma_R$  to be treated as an  $R \times R$  matrix. From here on, we will not mention  $R$  and  $T$  anymore since they are abstracted away through the total number of permutations  $P = RT$  and the permutation matrix  $A$ .

### A.1.3 Notation

If  $F$  is the size of a set,  $\mathcal{F} = \{0, \dots, F-1\}$  is the set of indices and  $f \in \mathcal{F}$  is an index. Zero-based indexing will be particularly useful for our cyclic groups. I will follow this notation for  $P$  (permutations),  $D$  (features, both spatial and incoming channels),  $F$  (canonical parts) and  $N$  (samples). Let  $X$  denote by context either a random vector corresponding to a complete sample ( $\mathbf{x}$  from (A.1)) or a sample. Let  $\mathbf{X} = (X^{(1)}, \dots, X^{(N)})$  denote the entire training dataset. Similar notation follows for the latent space using  $Z$  and  $W$ . To improve readability, the  $(i, j)$  index of the permutation matrix  $A$  will be denoted as  $A(i, j)$ , to avoid small fonts.



## A.2 Model

Let  $Z \in \mathcal{F}$  be a latent variable indicating which cluster component or “part” and let  $W \in \mathcal{P}$  denote the latent permutation. Then, parts are assumed to be generated from the following distribution

$$(Z, W) \sim \text{Cat}(\pi),$$

$$X_{w',d} \mid Z = z, W = w \sim \text{Bern}(\mu_{z,A(w,w'),d}), \quad \forall w', d$$

where  $\mu \in [0, 1]^{F \times P \times D}$  represents the parts model and  $\pi \in [0, 1]^{F \times P}$  the joint priors over  $(Z, W)$ . As we can see, the permutation parameter  $W$  dictates which segment of  $\mu$  a block of  $X$  is generated from. An illustration of this is seen in fig. A.1.

## A.3 Expectation Maximization

The parameters  $\theta = (\pi, \mu)$  are trained using the Expectation Maximization (EM) algorithm. Starting with the E-step:

$$\begin{aligned} Q(\theta, \theta^{(\text{old})}) &= \mathbb{E}_{\mathbf{Z}, \mathbf{W} \mid \mathbf{X}; \theta^{(\text{old})}} [\log \Pr(\mathbf{X}, \mathbf{Z}, \mathbf{W}; \theta)] \\ &= \sum_n \mathbb{E}_{Z^{(n)}, W^{(n)} \mid X^{(n)}; \theta^{(\text{old})}} [\log \Pr(X^{(n)}, Z^{(n)}, W^{(n)}; \theta)] \\ &= \sum_{n, Z, W} \underbrace{\Pr(Z, W \mid X^{(n)}; \theta^{(\text{old})})}_{\gamma_{n, Z, W}} \log \Pr(X^{(n)}, Z, W; \theta) \end{aligned}$$

The responsibilities,  $\gamma \in [0, 1]^{N \times F \times P}$ , are computed as follows

$$\begin{aligned} \gamma_{Z, W}^{(n)} &= \Pr(Z, W \mid X^{(n)}; \theta^{(\text{old})}) \\ &= \frac{\Pr(X^{(n)} \mid Z, W; \mu^{(\text{old})}) \Pr(Z, W; \pi^{(\text{old})})}{\sum_{Z', W'} \Pr(X^{(n)} \mid Z', W'; \mu^{(\text{old})}) \Pr(Z', W'; \pi^{(\text{old})})} \end{aligned}$$

Introducing unnormalized responsibilities  $\gamma'$  and expanding the probabilities gives

$$\gamma_{z,w}^{(n)} = \frac{\tilde{\gamma}_{z,w}^{(n)}}{\sum_{z',w'} \tilde{\gamma}_{z',w'}^{(n)}}, \quad \tilde{\gamma}_{z,w}^{(n)} = \pi_{z,w} \prod_{w',d} p(X_{A(w,w'),d}^{(n)}; \mu_{z,w',d}),$$

where,  $p(X; \mu) = \mu^X (1 - \mu)^{1-X}$ . When implementing this, it is better to calculate the log of the unnormalized responsibilities and use the log-sum-exp trick to avoid underflow. The complete log-likelihood is given by

$$\begin{aligned} \log \Pr(X, Z, W; \theta) &= \log \Pr(X \mid Z, W; \mu) \Pr(Z, W; \pi) \\ &= \log \pi_{Z,W} + \sum_{W',d} \log p(X_{A(W,W'),d}; \mu_{Z,W',d}), \end{aligned}$$

where we note that  $\log p(x; \mu) = x \log \mu + (1 - x) \log(1 - \mu)$ .

The M-step is

$$\theta^{(\text{new})} = \arg \max_{\theta} Q(\theta, \theta^{(\text{old})})$$

Starting with  $\pi$ , this follows the same update as a regular Bernoulli EM. This is given by adding a Lagrange multiplier that ensures that  $\sum_{z',w'} \pi_{z',w'} = 1$ , deriving and setting the result to zero:

$$\pi_{z,w}^{(\text{new})} = \frac{\sum_n \gamma_{z,w}^{(n)}}{N}.$$

For  $\mu$ , we have

$$\frac{\partial Q(\theta, \theta^{(\text{old})})}{\partial \mu_{f,w,d}} = \sum_{n,w'} \gamma_{f,w'}^{(n)} \left[ \frac{X_{A(w,w'),d}^{(n)}}{\mu_{f,w,d}} - \frac{1 - X_{A(w,w'),d}^{(n)}}{1 - \mu_{f,w,d}} \right].$$

Setting this to zero and re-arranging yields

$$\mu_{f,w,d}^{(\text{new})} = \frac{\sum_{n,w'} \gamma_{f,w'}^{(n)} X_{A(w,w'),d}^{(n)}}{\sum_{n,w'} \gamma_{f,w'}^{(n)}}$$

## A.4 Coding Features

Once the parameters  $\mu$  have been determined, we code a certain feature over a patch by finding the maximum likelihood part over it. If we were true to the model, we would set

$$(Z^{(\text{ML})}, W^{(\text{ML})}) = \arg \max_{Z,W} \Pr(X \mid Z, W; \mu),$$

where  $X$  is arranged as in (A.1). However, this requires the tedious and computationally intensive task of rotating and polarity-flipping the patch. Instead, we rely on the nearly perfect correlation between the transformed patches and match only the original patch to one of the transformations. This is equivalent of taking the parts model and considering it to be  $\mu \in [0, 1]^{FP \times D}$ , where  $FP$  now is the number of parts. In this formulation, the coding of the parts is identical to the original model without a latent permutation parameter.

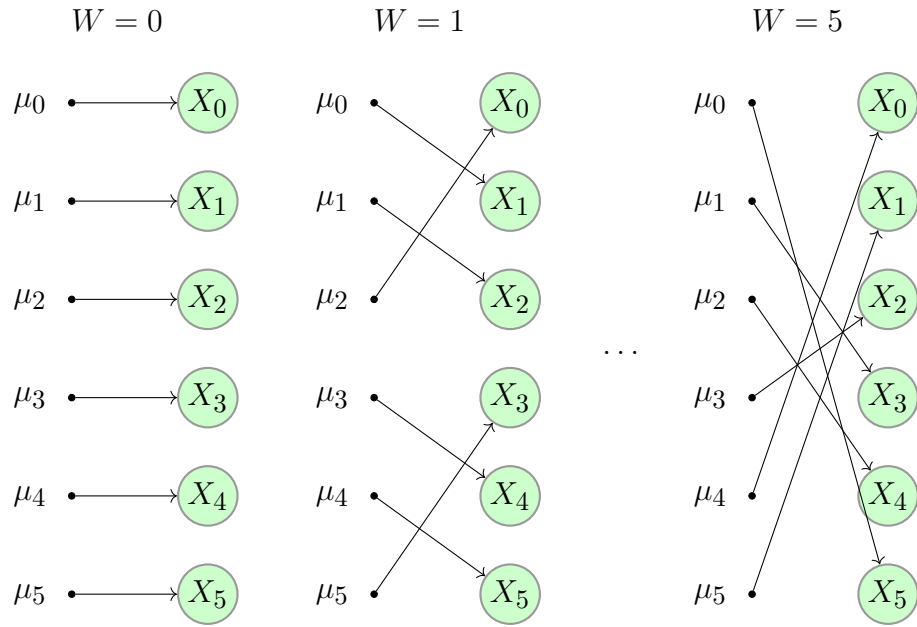


Figure A.1: **Latent permutations.** This illustrates how the latent permutation parameter  $W$  controls how the blocks of the parameter  $\mu$  are paired with the blocks of the data  $X$ . In this case  $R = 3$  and  $T = 2$  and the permutations follow the matrix in (A.2).

## REFERENCES

- [1] Martín Abadi, Ashish Agarwal, Paul Barham, Eugene Brevdo, Zhifeng Chen, Craig Citro, Greg S. Corrado, Andy Davis, Jeffrey Dean, Matthieu Devin, Sanjay Ghemawat, Ian Goodfellow, Andrew Harp, Geoffrey Irving, Michael Isard, Yangqing Jia, Rafal Jozefowicz, Lukasz Kaiser, Manjunath Kudlur, Josh Levenberg, Dan Mané, Rajat Monga, Sherry Moore, Derek Murray, Chris Olah, Mike Schuster, Jonathon Shlens, Benoit Steiner, Ilya Sutskever, Kunal Talwar, Paul Tucker, Vincent Vanhoucke, Vijay Vasudevan, Fernanda Viégas, Oriol Vinyals, Pete Warden, Martin Wattenberg, Martin Wicke, Yuan Yu, and Xiaoqiang Zheng. TensorFlow: Large-scale machine learning on heterogeneous systems, 2015. Software available from tensorflow.org. 40
- [2] Yali Amit and Alain Trouvé. Pop: Patchwork of parts models for object recognition. *International Journal of Computer Vision*, 75(2):267–282, 2007. 9
- [3] Andreas Argyriou, Theodoros Evgeniou, and Massimiliano Pontil. Convex multi-task feature learning. *Machine Learning*, 73(3):243–272, 2008. 72
- [4] Jimmy Ba and Rich Caruana. Do deep nets really need to be deep? In *Advances in Neural Information Processing Systems (NIPS)*, pages 2654–2662, 2014. 71
- [5] Dana H Ballard. Modular learning in neural networks. In *AAAI*, pages 279–284, 1987. 21
- [6] Amy Bearman, Olga Russakovsky, Vittorio Ferrari, and Li Fei-Fei. What’s the Point: Semantic Segmentation with Point Supervision. In *European Conference on Computer Vision (ECCV)*, 2016. 50
- [7] Yoshua Bengio, Pascal Lamblin, Dan Popovici, Hugo Larochelle, et al. Greedy layer-wise training of deep networks. *Advances in Neural Information Processing Systems (NIPS)*, 19:153, 2007. 21, 24
- [8] Yoshua Bengio, Eric Thibodeau-Laufer, Guillaume Alain, and Jason Yosinski. Deep generative stochastic networks trainable by backprop. In *International Conference on Machine Learning (ICML)*, pages 226–234, 2014. 23
- [9] Elliot Joel Bernstein and Yali Amit. Part-based statistical models for object classification and detection. In *Conference on Computer Vision and Pattern Recognition (CVPR)*, volume 2, pages 734–740. IEEE, 2005. 5, 8, 16
- [10] Gedas Bertasius, Jianbo Shi, and Lorenzo Torresani. Deepedge: A multi-scale bifurcated deep network for top-down contour detection. In *Conference on Computer Vision and Pattern Recognition (CVPR)*, 2015. 32
- [11] Cristian Buciluă, Rich Caruana, and Alexandru Niculescu-Mizil. Model compression. In *Proceedings of the 12th ACM SIGKDD international conference on Knowledge discovery and data mining*, pages 535–541. ACM, 2006. 71

- [12] Rich Caruana. Multitask learning. In *Learning to learn*, pages 95–133. Springer, 1998. 72, 82
- [13] Guillaume Charpiat, Matthias Hofmann, and Bernhard Schölkopf. Automatic image colorization via multimodal predictions. In *European Conference on Computer Vision (ECCV)*, 2008. 27, 30, 33
- [14] Jianhui Chen, Jiayu Zhou, and Jieping Ye. Integrating low-rank and group-sparse structures for robust multi-task learning. In *Proceedings of the 17th ACM SIGKDD international conference on Knowledge discovery and data mining*, pages 42–50. ACM, 2011. 72
- [15] Liang-Chieh Chen, George Papandreou, Iasonas Kokkinos, Kevin Murphy, and Alan L Yuille. Semantic image segmentation with deep convolutional nets and fully connected crfs. In *International Conference on Learning Representations (ICLR)*, 2015. 32
- [16] Tianqi Chen, Bing Xu, Chiyuan Zhang, and Carlos Guestrin. Training deep nets with sublinear memory cost. *arXiv preprint arXiv:1604.06174*, 2016. 88
- [17] Gong Cheng, Peicheng Zhou, and Junwei Han. Rofd-cnn: Rotation-invariant and fisher discriminative convolutional neural networks for object detection. In *Proceedings of the IEEE Conference on Computer Vision and Pattern Recognition*, pages 2884–2893, 2016. 8
- [18] Zezhou Cheng, Qingxiong Yang, and Bin Sheng. Deep colorization. In *ICCV*, 2015. 27, 30, 31, 33, 43, 44, 45, 46
- [19] Alex Yong-Sang Chia, Shaojie Zhuo, Raj Kumar Gupta, Yu-Wing Tai, Siu-Yeung Cho, Ping Tan, and Stephen Lin. Semantic colorization with internet images. *ACM Transactions on Graphics (TOG)*, 30(6), 2011. 27, 30
- [20] Andrzej Cichocki, Sergio Cruces, and Shun-ichi Amari. Generalized alpha-beta divergences and their application to robust nonnegative matrix factorization. *Entropy*, 13(1):134–170, 2011. 76, 77
- [21] Adam Coates, Honglak Lee, and Andrew Y Ng. An analysis of single-layer networks in unsupervised feature learning. In *Artificial Intelligence and Statistics Conference (AISTATS)*, 2011. 5, 10, 51
- [22] Taco S Cohen and Max Welling. Group equivariant convolutional networks. In *International Conference on Machine Learning (ICML)*, 2016. 8
- [23] Aditya Deshpande, Jason Rock, and David Forsyth. Learning large-scale automatic image colorization. In *ICCV*, 2015. 27, 28, 29, 30, 31, 32, 33, 36, 43, 44, 45
- [24] Sander Dieleman, Jeffrey De Fauw, and Koray Kavukcuoglu. Exploiting cyclic symmetry in convolutional neural networks. In *International Conference on Machine Learning (ICML)*, 2016. 8

- [25] Carl Doersch, Abhinav Gupta, and Alexei A. Efros. Unsupervised visual representation learning by context prediction. In *International Conference on Computer Vision (ICCV)*, 2015. 49, 50, 52, 57
- [26] Carl Doersch, Abhinav Gupta, and Alexei A. Efros. Unsupervised visual representation learning by context prediction. In *International Conference on Computer Vision (ICCV)*, pages 1422–1430, 2015. 50
- [27] Jeff Donahue, Philipp Krähenbühl, and Trevor Darrell. Adversarial feature learning. In *International Conference on Learning Representations (ICLR)*, 2017. 25, 49, 52, 57, 58
- [28] John Duchi, Elad Hazan, and Yoram Singer. Adaptive subgradient methods for online learning and stochastic optimization. *Journal of Machine Learning Research (JMLR)*, 12(Jul):2121–2159, 2011. 85
- [29] Vincent Dumoulin, Ishmael Belghazi, Ben Poole, Alex Lamb, Martin Arjovsky, Olivier Mastropietro, and Aaron Courville. Adversarially learned inference. In *International Conference on Learning Representations (ICLR)*, 2017. 52
- [30] M. Everingham, L. Van Gool, C. K. I. Williams, J. Winn, and A. Zisserman. The PASCAL Visual Object Classes Challenge 2012 (VOC2012) Results. <http://www.pascal-network.org/challenges/VOC/voc2012/workshop/index.html>. 40
- [31] Theodoros Evgeniou and Massimiliano Pontil. Regularized multi-task learning. In *Proceedings of the tenth ACM SIGKDD international conference on Knowledge discovery and data mining*, pages 109–117. ACM, 2004. 72
- [32] Clement Farabet, Camille Couprie, Laurent Najman, and Yann LeCun. Learning hierarchical features for scene labeling. *IEEE Transactions on Pattern Analysis and Machine Intelligence (PAMI)*, 35(8), 2013. 32
- [33] Gunnar Farneback. Two-frame motion estimation based on polynomial expansion. *Image analysis*, pages 363–370, 2003. 98
- [34] Yaroslav Ganin and Victor S. Lempitsky.  $N^4$ -fields: Neural network nearest neighbor fields for image transforms. In *Asian Conference on Computer Vision (ACCV)*, 2014. 32
- [35] Xavier Glorot and Yoshua Bengio. Understanding the difficulty of training deep feedforward neural networks. In *Artificial Intelligence and Statistics Conference (AISTATS)*, 2010. 41, 51, 54
- [36] Yves Grandvalet and Yoshua Bengio. Semi-supervised learning by entropy minimization. In *Advances in Neural Information Processing Systems (NIPS)*, 2004. 49

- [37] Audrunas Gruslys, Remi Munos, Ivo Danihelka, Marc Lanctot, and Alex Graves. Memory-efficient backpropagation through time. In *Advances in Neural Information Processing Systems (NIPS)*, pages 4125–4133, 2016. 88
- [38] Raj Kumar Gupta, Alex Yong-Sang Chia, Deepu Rajan, Ee Sin Ng, and Huang Zhiyong. Image colorization using similar images. In *ACM international conference on Multimedia*, 2012. 27, 30
- [39] B. Hariharan, P. Aberl  ez an R. Girshick, and J. Malik. Hypercolumns for object segmentation and fine-grained localization. *Conference on Computer Vision and Pattern Recognition (CVPR)*, 2015. 28, 32
- [40] Kaiming He, Xiangyu Zhang, Shaoqing Ren, and Jian Sun. Delving deep into rectifiers: Surpassing human-level performance on imagenet classification. *CoRR*, abs/1502.01852, 2015. 51
- [41] Kaiming He, Xiangyu Zhang, Shaoqing Ren, and Jian Sun. Deep residual learning for image recognition. In *Conference on Computer Vision and Pattern Recognition (CVPR)*, pages 770–778, 2016. 23
- [42] Geoffrey Hinton, Alex Krizhevsky, and Sida Wang. Transforming auto-encoders. *Artificial Neural Networks and Machine Learning (ICANN)*, pages 44–51, 2011. 23
- [43] Geoffrey Hinton, Oriol Vinyals, and Jeff Dean. Distilling the knowledge in a neural network. In *NIPS (workshop)*, 2015. 71
- [44] Geoffrey E Hinton. Training products of experts by minimizing contrastive divergence. *Neural computation*, 14(8):1771–1800, 2002. 6
- [45] Geoffrey E Hinton. To recognize shapes, first learn to generate images. *Progress in brain research*, 165:535–547, 2007. 9
- [46] Geoffrey E Hinton and Ruslan R Salakhutdinov. Reducing the dimensionality of data with neural networks. *science*, 313(5786):504–507, 2006. 6, 21
- [47] Geoffrey E Hinton and Terrence J Sejnowski. Learning and releaming in boltzmann machines. *Parallel Distrlimted Processing*, 1, 1986. 6
- [48] Yi-Chin Huang, Yi-Shin Tung, Jun-Cheng Chen, Sung-Wen Wang, and Ja-Ling Wu. An adaptive edge detection based colorization algorithm and its applications. In *ACM international conference on Multimedia*, 2005. 30
- [49] Jarmo Hurri and Aapo Hyv  rinen. Simple-cell-like receptive fields maximize temporal coherence in natural video. *Neural Computation*, 15(3):663–691, 2003. 52
- [50] Aapo Hyvarinen and Hiroshi Morioka. Unsupervised feature extraction by time-contrastive learning and nonlinear ica. In *Advances in Neural Information Processing Systems (NIPS)*, 2016. 52



- [51] Satoshi Iizuka, Edgar Simo-Serra, and Hiroshi Ishikawa. Let there be Color!: Joint End-to-end Learning of Global and Local Image Priors for Automatic Image Colorization with Simultaneous Classification. *ACM Transactions on Graphics (SIGGRAPH)*, 35(4), 2016. 31
- [52] Satoshi Iizuka, Edgar Simo-Serra, and Hiroshi Ishikawa. Let there be Color!: Joint End-to-end Learning of Global and Local Image Priors for Automatic Image Colorization with Simultaneous Classification. *ACM Transactions on Graphics (SIGGRAPH)*, 35(4), 2016. 53
- [53] Sergey Ioffe and Christian Szegedy. Batch normalization: Accelerating deep network training by reducing internal covariate shift. In *ICML*, 2015. 37, 54
- [54] Revital Irony, Daniel Cohen-Or, and Dani Lischinski. Colorization by example. In *Eurographics Symp. on Rendering*, 2005. 27, 30
- [55] Phillip Isola, Daniel Zoran, Dilip Krishnan, and Edward H Adelson. Learning visual groups from co-occurrences in space and time. *arXiv preprint arXiv:1511.06811*, 2015. 52
- [56] Dinesh Jayaraman and Kristen Grauman. Slow and steady feature analysis: higher order temporal coherence in video. In *Conference on Computer Vision and Pattern Recognition (CVPR)*, 2016. 52
- [57] Yangqing Jia, Evan Shelhamer, Jeff Donahue, Sergey Karayev, Jonathan Long, Ross Girshick, Sergio Guadarrama, and Trevor Darrell. Caffe: Convolutional architecture for fast feature embedding. *arXiv preprint arXiv:1408.5093*, 2014. 40
- [58] Diederik P. Kingma and Jimmy Ba. Adam: A method for stochastic optimization. In *International Conference on Learning Representations (ICLR)*, 2015. 51, 85
- [59] Diederik P Kingma and Max Welling. Auto-encoding variational bayes. In *International Conference on Learning Representations (ICLR)*, 2014. 23, 49
- [60] Iasonas Kokkinos. Ubernet: Training a universal convolutional neural network for low-, mid-, and high-level vision using diverse datasets and limited memory. *arXiv preprint arXiv:1609.02132*, 2016. 72, 88
- [61] Philipp Krähenbühl, Carl Doersch, Jeff Donahue, and Trevor Darrell. Data-dependent initializations of convolutional neural networks. In *International Conference on Learning Representations (ICLR)*, 2016. 25, 51, 57, 62
- [62] Alex Krizhevsky, Ilya Sutskever, and Geoffrey E Hinton. Imagenet classification with deep convolutional neural networks. In *Advances in Neural Information Processing Systems (NIPS)*, pages 1097–1105, 2012. 23, 25
- [63] Solomon Kullback and Richard A Leibler. On information and sufficiency. *The annals of mathematical statistics*, 22(1):79–86, 1951. 74

- [64] Abhishek Kumar and Hal Daumé III. Learning task grouping and overlap in multi-task learning. In *International Conference on Machine Learning (ICML)*, 2012. 72
- [65] Hugo Larochelle and Yoshua Bengio. Classification using discriminative restricted boltzmann machines. In *International Conference on Machine Learning (ICML)*, pages 536–543. ACM, 2008. 7
- [66] Hugo Larochelle, Dumitru Erhan, Aaron Courville, James Bergstra, and Yoshua Bengio. An empirical evaluation of deep architectures on problems with many factors of variation. In *International Conference on Machine Learning (ICML)*, pages 473–480. ACM, 2007. 17, 19
- [67] Gustav Larsson, Michael Maire, and Gregory Shakhnarovich. Learning representations for automatic colorization. In *European Conference on Computer Vision (ECCV)*, 2016. 50, 52, 53
- [68] Gustav Larsson, Michael Maire, and Gregory Shakhnarovich. Colorization as a proxy task for visual understanding. In *Conference on Computer Vision and Pattern Recognition (CVPR)*, 2017. 50, 52
- [69] Gustav Larsson, Michael Maire, and Gregory Shakhnarovich. Fractalnet: Ultra-deep neural networks without residuals. In *International Conference on Learning Representations (ICLR)*, 2017. 25, 90
- [70] Honglak Lee, Roger Grosse, Rajesh Ranganath, and Andrew Y Ng. Unsupervised learning of hierarchical representations with convolutional deep belief networks. *Communications of the ACM*, 54(10):95–103, 2011. 6, 18
- [71] Anat Levin, Dani Lischinski, and Yair Weiss. Colorization using optimization. *ACM Transactions on Graphics (TOG)*, 23(3), 2004. 27, 30
- [72] Percy Liang, Hal Daumé III, and Dan Klein. Structure compilation: trading structure for features. In *International Conference on Machine Learning (ICML)*, pages 592–599. ACM, 2008. 72
- [73] Wei Liu, Andrew Rabinovich, and Alexander C Berg. Parsenet: Looking wider to see better. *arXiv preprint arXiv:1506.04579*, 2015. 37
- [74] Jonathan Long, Evan Shelhamer, and Trevor Darrell. Fully convolutional networks for semantic segmentation. In *Conference on Computer Vision and Pattern Recognition (CVPR)*, 2015. 30, 32, 58
- [75] Qing Luan, Fang Wen, Daniel Cohen-Or, Lin Liang, Ying-Qing Xu, and Heung-Yeung Shum. Natural image colorization. In *Eurographics conference on Rendering Techniques*, 2007. 30

- [76] Michael Maire, Stella X. Yu, and Pietro Perona. Reconstructive sparse code transfer for contour detection and semantic labeling. In *Asian Conference on Computer Vision (ACCV)*, 2014. 28, 32
- [77] Xiaojiao Mao, Chunhua Shen, and Yu-Bin Yang. Image restoration using very deep convolutional encoder-decoder networks with symmetric skip connections. In *Advances in Neural Information Processing Systems (NIPS)*, pages 2802–2810, 2016. 24
- [78] Marcin Marszałek, Ivan Laptev, and Cordelia Schmid. Actions in context. In *Computer Vision and Pattern Recognition, 2009. CVPR 2009. IEEE Conference on*, pages 2929–2936. IEEE, 2009. 98
- [79] Dmytro Mishkin and Jiri Matas. All you need is a good init. *arXiv preprint arXiv:1511.06422*, 2015. 51
- [80] Ishan Misra, Abhinav Shrivastava, Abhinav Gupta, and Martial Hebert. Cross-stitch networks for multi-task learning. In *Proceedings of the IEEE Conference on Computer Vision and Pattern Recognition*, pages 3994–4003, 2016. 72
- [81] Ishan Misra, C Lawrence Zitnick, and Martial Hebert. Unsupervised learning using sequential verification for action recognition. 2016. 52
- [82] Hossein Mobahi, Ronan Collobert, and Jason Weston. Deep learning from temporal coherence in video. In *International Conference on Machine Learning (ICML)*, 2009. 52
- [83] Yuji Morimoto, Yuichi Taguchi, and Takeshi Naemura. Automatic colorization of grayscale images using multiple images on the web. In *SIGGRAPH: Posters*, 2009. 27, 28, 30, 44
- [84] Mohammadreza Mostajabi, Payman Yadollahpour, and Gregory Shakhnarovich. Feed-forward semantic segmentation with zoom-out features. In *Conference on Computer Vision and Pattern Recognition (CVPR)*, 2015. 28, 32, 54, 55
- [85] Vinod Nair and Geoffrey E Hinton. Implicit mixtures of restricted boltzmann machines. In *Advances in Neural Information Processing Systems (NIPS)*, pages 1145–1152, 2009. 7
- [86] Vinod Nair and Geoffrey E Hinton. Rectified linear units improve restricted boltzmann machines. In *International Conference on Machine Learning (ICML)*, pages 807–814, 2010. 51
- [87] Andrew Ng. Sparse autoencoder. *CS294A Lecture notes*, 72(2011):1–19, 2011. 23
- [88] Mehdi Noroozi and Paolo Favaro. Unsupervised learning of visual representations by solving jigsaw puzzles. In *European Conference on Computer Vision (ECCV)*, 2016. 52, 57, 69, 98, 100

- [89] Andrew Owens, Jiajun Wu, Josh H. McDermott, William T. Freeman, and Antonio Torralba. Ambient sound provides supervision for visual learning. In *European Conference on Computer Vision (ECCV)*, 2016. 52
- [90] Deepak Pathak, Ross B. Girshick, Piotr Dollár, Trevor Darrell, and Bharath Hariharan. Learning features by watching objects move. In *Conference on Computer Vision and Pattern Recognition (CVPR)*, 2017. 52, 69, 72, 98
- [91] Deepak Pathak, Philipp Krähenbühl, Jeff Donahue, Trevor Darrell, and Alexei Efros. Context encoders: Feature learning by inpainting. In *Conference on Computer Vision and Pattern Recognition (CVPR)*, 2016. 50, 52, 57
- [92] Deepak Pathak, Philipp Krahenbuhl, Jeff Donahue, Trevor Darrell, and Alexei A Efros. Context encoders: Feature learning by inpainting. In *Conference on Computer Vision and Pattern Recognition (CVPR)*, 2016. 50
- [93] Genevieve Patterson, Chen Xu, Hang Su, and James Hays. The sun attribute database: Beyond categories for deeper scene understanding. *International Journal of Computer Vision*, 108(1-2), 2014. 29, 44
- [94] Ning Qian. On the momentum term in gradient descent learning algorithms. *Neural networks*, 12(1):145–151, 1999. 51, 84
- [95] Yingge Qu, Tien-Tsin Wong, and Pheng-Ann Heng. Manga colorization. *ACM Transactions on Graphics (TOG)*, 25(3), 2006. 27, 30
- [96] Marc’Aurelio Ranzato, Arthur Szlam, Joan Bruna, Michaël Mathieu, Ronan Collobert, and Sumit Chopra. Video (language) modeling: a baseline for generative models of natural videos. *arXiv preprint arXiv:1412.6604*, 2014. 52
- [97] Antti Rasmus, Mathias Berglund, Mikko Honkala, Harri Valpola, and Tapani Raiko. Semi-supervised learning with ladder networks. In *Advances in Neural Information Processing Systems (NIPS)*, pages 3546–3554, 2015. 23
- [98] Alfréd Rényi et al. On measures of entropy and information. In *Proceedings of the Fourth Berkeley Symposium on Mathematical Statistics and Probability, Volume 1: Contributions to the Theory of Statistics*. The Regents of the University of California, 1961. 76
- [99] Adriana Romero, Nicolas Ballas, Samira Ebrahimi Kahou, Antoine Chassang, Carlo Gatta, and Yoshua Bengio. Fitnets: Hints for thin deep nets. In *International Conference on Learning Representations (ICLR)*, 2015. 24
- [100] Olga Russakovsky, Jia Deng, Hao Su, Jonathan Krause, Sanjeev Satheesh, Sean Ma, Zhiheng Huang, Andrej Karpathy, Aditya Khosla, Michael Bernstein, Alexander C. Berg, and Li Fei-Fei. ImageNet Large Scale Visual Recognition Challenge. *International Journal of Computer Vision (IJCV)*, 115(3), 2015. 29, 32, 54, 98

- [101] Mehdi Sajjadi, Mehran Javanmardi, and Tolga Tasdizen. Regularization with stochastic transformations and perturbations for deep semi-supervised learning. *Advances in Neural Information Processing Systems (NIPS)*, 2016. 49
- [102] Ruslan Salakhutdinov and Geoffrey Hinton. Deep boltzmann machines. In *Artificial Intelligence and Statistics*, pages 448–455, 2009. 6
- [103] Guillermo Sapiro. Inpainting the colors. In *ICIP*, 2005. 27
- [104] Wei Shen, Xinggang Wang, Yan Wang, Xiang Bai, and Zhijiang Zhang. Deepcontour: A deep convolutional feature learned by positive-sharing loss for contour detection. In *Conference on Computer Vision and Pattern Recognition (CVPR)*, 2015. 32
- [105] Jianbo Shi and Jitendra Malik. Normalized cuts and image segmentation. *Pattern Analysis and Machine Intelligence, IEEE Transactions on*, 22(8), 2000. 30
- [106] K. Simonyan and A. Zisserman. Very deep convolutional networks for large-scale image recognition. In *International Conference on Learning Representations (ICLR)*, 2015. 23, 28, 32, 37
- [107] Paul Smolensky. Information processing in dynamical systems: Foundations of harmony theory. Technical report, DTIC Document, 1986. 6
- [108] Richard Socher, Jeffrey Pennington, Eric H Huang, Andrew Y Ng, and Christopher D Manning. Semi-supervised recursive autoencoders for predicting sentiment distributions. In *Proceedings of the conference on empirical methods in natural language processing*, pages 151–161. Association for Computational Linguistics, 2011. 23
- [109] Kihyuk Sohn and Honglak Lee. Learning invariant representations with local transformations. 2012. 7, 17
- [110] Kihyuk Sohn, Guanyu Zhou, Chansoo Lee, and Honglak Lee. Learning and selecting features jointly with point-wise gated boltzmann machines. In *International Conference on Machine Learning (ICML)*, pages 217–225, 2013. 7, 17, 18
- [111] Nitish Srivastava, Geoffrey Hinton, Alex Krizhevsky, Ilya Sutskever, and Ruslan Salakhutdinov. Dropout: A simple way to prevent neural networks from overfitting. *Journal of Machine Learning Research (JMLR)*, 15(1), 2014. 8, 23
- [112] Nitish Srivastava, Elman Mansimov, and Ruslan Salakhutdinov. Unsupervised learning of video representations using lstms. In *International Conference on Machine Learning (ICML)*, 2015. 52
- [113] Daniel Šỳkora, Jan Buriánek, and Jiří Žára. Unsupervised colorization of black-and-white cartoons. In *International symposium on Non-photorealistic animation and rendering*, 2004. 27

- [114] Yu-Wing Tai, Jiaya Jia, and Chi-Keung Tang. Local color transfer via probabilistic segmentation by expectation-maximization. In *Conference on Computer Vision and Pattern Recognition (CVPR)*, 2005. 30
- [115] Tijmen Tieleman and Geoffrey Hinton. Lecture 6.5 - rmsprop, coursera: Neural networks for machine learning. 2012. 85, 86
- [116] Engin Tola, Vincent Lepetit, and Pascal Fua. A fast local descriptor for dense matching. In *Conference on Computer Vision and Pattern Recognition (CVPR)*, 2008. 30
- [117] Sotirios A Tsaftaris, Francesca Casadio, Jean-Louis Andral, and Aggelos K Katsaggelos. A novel visualization tool for art history and conservation: Automated colorization of black and white archival photographs of works of art. *Studies in Conservation*, 59(3), 2014. 27
- [118] Naonori Ueda and Ryohei Nakano. Generalization error of ensemble estimators. In *Neural Networks, 1996., IEEE International Conference on*, volume 1, pages 90–95. IEEE, 1996. 73
- [119] G. Urban, K. J. Geras, S. Ebrahimi Kahou, O. Aslan, S. Wang, R. Caruana, A. Mohamed, M. Philipose, and M. Richardson. Do deep convolutional nets really need to be deep (or even convolutional)? In *International Conference on Learning Representations (ICLR)*, 2017. 71
- [120] Harri Valpola. From neural pca to deep unsupervised learning. *Advances in Independent Component Analysis and Learning Machines*, pages 143–171, 2015. 23, 24, 26
- [121] J Hans van Hateren and Dan L Ruderman. Independent component analysis of natural image sequences yields spatio-temporal filters similar to simple cells in primary visual cortex. *Proceedings of the Royal Society of London B: Biological Sciences*, 265(1412):2315–2320, 1998. 52
- [122] Pascal Vincent, Hugo Larochelle, Yoshua Bengio, and Pierre-Antoine Manzagol. Extracting and composing robust features with denoising autoencoders. In *Proceedings of the 25th international conference on Machine learning*, pages 1096–1103. ACM, 2008. 23, 26
- [123] Pascal Vincent, Hugo Larochelle, Isabelle Lajoie, Yoshua Bengio, and Pierre-Antoine Manzagol. Stacked denoising autoencoders: Learning useful representations in a deep network with a local denoising criterion. *Journal of Machine Learning Research (JMLR)*, 11(Dec):3371–3408, 2010. 8, 17, 23
- [124] Xiaolong Wang and Abhinav Gupta. Unsupervised learning of visual representations using videos. In *International Conference on Computer Vision (ICCV)*, 2015. 50, 52, 57

- [125] Tomihisa Welsh, Michael Ashikhmin, and Klaus Mueller. Transferring color to greyscale images. *ACM Transactions on Graphics (TOG)*, 21(3), 2002. 27, 29, 30, 43, 44, 45
- [126] Daniel E Worrall, Stephan J Garbin, Daniyar Turmukhambetov, and Gabriel J Brostow. Harmonic networks: Deep translation and rotation equivariance. In *Conference on Computer Vision and Pattern Recognition (CVPR)*, 2017. 8
- [127] Zifeng Wu, Chunhua Shen, and Anton van den Hengel. High-performance semantic segmentation using very deep fully convolutional networks. *CoRR*, abs/1604.04339, 2016. 55
- [128] Jianxiong Xiao, James Hays, Krista A Ehinger, Aude Oliva, and Antonio Torralba. Sun database: Large-scale scene recognition from abbey to zoo. In *Conference on Computer Vision and Pattern Recognition (CVPR)*, 2010. 29, 44
- [129] Saining Xie and Zhuowen Tu. Holistically-nested edge detection. In *International Conference on Computer Vision (ICCV)*, 2015. 32
- [130] Jia Xu, Alexander G. Schwing, and Raquel Urtasun. Learning to segment under various forms of weak supervision. In *Conference on Computer Vision and Pattern Recognition (CVPR)*, 2015. 50
- [131] Yongxin Yang and Timothy Hospedales. Deep multi-task representation learning: A tensor factorisation approach. In *International Conference on Learning Representations (ICLR)*, 2017. 72
- [132] Liron Yatziv and Guillermo Sapiro. Fast image and video colorization using chrominance blending. *Image Processing, IEEE Transactions on*, 15(5), 2006. 30
- [133] Fisher Yu and Vladlen Koltun. Multi-scale context aggregation by dilated convolutions. In *International Conference on Learning Representations (ICLR)*, 2016. 55
- [134] Matthew D Zeiler. Adadelta: an adaptive learning rate method. *arXiv preprint arXiv:1212.5701*, 2012. 85, 86
- [135] Richard Zhang, Phillip Isola, and Alexei A Efros. Colorful image colorization. In *European Conference on Computer Vision (ECCV)*, 2016. 31, 46, 50, 52, 53, 57, 66
- [136] Richard Zhang, Phillip Isola, and Alexei A Efros. Split-brain autoencoders: Unsupervised learning by cross-channel prediction. In *Conference on Computer Vision and Pattern Recognition (CVPR)*, 2017. 52, 57, 66, 81
- [137] Junbo Zhao, Michael Mathieu, Ross Goroshin, and Yann LeCun. Stacked what-where auto-encoders. *arXiv preprint arXiv:1506.02351*, 2015. 23

- [138] Bolei Zhou, Aditya Khosla, Àgata Lapedriza, Aude Oliva, and Antonio Torralba. Object detectors emerge in deep scene cnns. In *International Conference on Learning Representations (ICLR)*, 2015. 65
- [139] Bolei Zhou, Agata Lapedriza, Jianxiong Xiao, Antonio Torralba, and Aude Oliva. Learning deep features for scene recognition using places database. In *Advances in Neural Information Processing Systems (NIPS)*, pages 487–495, 2014. 54, 98
- [140] Yanzhao Zhou, Qixiang Ye, Qiang Qiu, and Jianbin Jiao. Oriented response networks. In *Conference on Computer Vision and Pattern Recognition (CVPR)*, 2017. 8